Distribution Statement

Distribution A: Public Release.

The views presented here are those of the author and are not to be construed as official or reflecting the views of the Uniformed Services University of the Health Sciences, the Department of Defense or the U.S. Government.

Card19 is a regulator of MICOS complex proteins and protects against mitochondrial dysfunction in macrophages

by

Kariana Elizabeth Rios

Dissertation submitted to the Faculty of the
Emerging Infectious Diseases Graduate Program
Uniformed Services University of the Health Sciences

In partial fulfillment of the requirements for the degree of
Doctor of Philosophy 2020

UNIFORMED SERVICES UNIVERSITY OF THE HEALTH SCIENCES
SCHOOL OF MEDICINE GRADUATE PROGRAMS
Graduate Education Office (A 1045), 4301 Jones Bridge Road, Bethesda, MD 20814

APPROVAL OF THE DOCTORAL DISSERTATION IN THE EMERGING INFECTIOUS DISEASES GRADUATE PROGRAM

Title of Dissertation: "Card19 is a regulator of MICOS complex proteins and protects against mitochondrial dysfunction in macrophages"

Name of Candidate: Kariana E. Rios
Doctor of Philosophy Degree
March 12, 2021

DISSERTATION AND ABSTRACT APPROVED:

DATE:

SNOW.ANDREW.L.1400942230 Digitally signed by SNOW.ANDREW.L.1400942230 Date: 2021.03.15 09:01:40 -04'00' 3/12/2021
Dr. Andrew Snow
DEPARTMENT OF PHARMACOLOGY & MOLECULAR THERAPEUTICS
Committee Chairperson

SCHAEFER.BRIAN.C.1260245305 Digitally signed by SCHAEFER.BRIAN.C.1260245305 Date: 2021.03.12 17:01:48 -05'00' 3/12/2021
Dr. Brian Schaefer
DEPARTMENT OF MICROBIOLOGY & IMMUNOLOGY
Dissertation Advisor

Joseph Mattapallil Digitally signed by Joseph Mattapallil DN: cn=Joseph Mattapallil, o=USUHS, ou=Dept of Microbiology and Immunology, email=joseph.mattapallil@usuhs.edu, c=US Date: 2021.03.12 21:06:19 -05'00' 3/12/2021
Dr. Joseph Mattapallil
DEPARTMENT OF MICROBIOLOGY & IMMUNOLOGY
Committee Member

LIECHTI.GEORGE.WARREN.1461677009 Digitally signed by LIECHTI.GEORGE.WARREN.1461677009 Date: 2021.03.14 14:51:18 -04'00' 3/12/2021
Dr. George Liechti
DEPARTMENT OF MICROBIOLOGY & IMMUNOLOGY
Committee Member

LEES.JASON.R.1461954878 Digitally signed by LEES.JASON.R.1461954878 Date: 2021.03.14 11:17:24 -04'00' 3/12/2021
Dr. Jason Lees
DEPARTMENT OF MEDICINE
Committee Member

ACKNOWLEDGMENTS

I would first like to acknowledge my advisor and mentor, Dr. Brian Schaefer, for allowing me to work on the Card19 project and for his mentorship and support over the last 6.5 years. I would also like to thank my thesis committee for their support and invaluable feedback over the years. Thank you to the entire Schaefer lab for their professional and personal support, especially to Dr. Chelsi Beauregard, who developed the immortalized macrophage lines that were invaluable for our mass spectrometry and gene characterization work. Many thanks to Dr. Dennis McDaniel for his extensive assistance with the microscopy work performed in this project, particularly the TEM imaging. Thank you also to Kateryna Lund, who helped me with the flow cytometry and Seahorse extracellular flux analysis components of this project. Acknowledgement and thanks also to our collaborators: Dr. Thomas Conrads and Dr. Ming Zhou at WHIRC, who performed the mass spectrometry analysis in this project, and Dr. Igor Brodsky and Dr. Elizabet Bjanes at UPenn, who identified the cell death resistance phenotype in *Card19 -/-* BMDMs and provided invaluable insight into the function of Card19. Thanks also to the McCabe lab, Michael Nieves, and Antigone Grillakis for their assistance with our mouse behavioral studies. Many thanks to Dr. Barbara Knollmann-Ritschel and Dr. Kim Williamson for their Catholic fellowship and many Rosaries. To Dr. Margaret Weis, who introduced me to the world of academic science and fed me far too well for a summer in Amarillo in 2012. To my parents, Carol and Michael, and to the Ringquist family, for their constant loving support. And to my beloved husband, Carl, for his constant, firm support and encouragement over 6.5 years, hundreds of miles, many moves, and countless experiments.

DEDICATION

For my husband, Carl, and for my son, George. All I have written is like straw compared to the love and joy you both bring into my life. D.O.M.

COPYRIGHT STATEMENT

The author hereby certifies that the use of any copyrighted material in the dissertation manuscript entitled: Card19 is a regulator of MICOS complex proteins and protects against mitochondrial dysfunction in macrophages is appropriately acknowledged and, beyond brief excerpts, is with the permission of the copyright owner.

Kariana Rios Digitally signed by Kariana Rios Date: 2021.03.25 14:24:18 -04'00'

Kariana E Rios

March 25, 2021.

DISCLAIMER

The views presented here are those of the author and are not to be construed as official or reflecting the views of the Uniformed Services University of the Health Sciences, the Department of Defense or the U.S. Government.

ABSTRACT

Card19 is a regulator of MICOS complex proteins and protects against mitochondrial dysfunction in macrophages

Kariana E. Rios, PhD, 2021.

Thesis directed by: Brian C. Schaefer, Professor, MIC

CARD19 is a protein of unknown function that was first reported in 2003 to interact with BCL10 and inhibit NF-κB in Jurkat T cells (196). Later investigation indicated the cDNA employed in the initial study represented an incompletely spliced mRNA product (30; 138). The fully spliced mRNA encoded a protein which localized to the mitochondria and endoplasmic reticulum in HeLa cells (30). Gene expression databases report that *CARD19* is highly transcribed in both human and murine myeloid cells (46; 161; 176). Furthermore, we observed that *Card19 -/-* mice injected with LPS display elevated levels of TNF-α, IL-6, and MCP-1, which are produced by macrophages. To address how absence of Card19 mediates this phenotype, we investigated the function of Card19 in CD8+ T cells and bone marrow derived macrophages (BMDMs). We confirmed via microscopy that endogenous Card19 is a mitochondrial protein in CD8+ T cells. Furthermore, we analyzed markers of NF-κB activation in restimulated CD8+ T cells via western blot; we found that there was not a significant difference between *Card19 +/+* and *Card19 -/-* CD8+ T cells on Bcl10 degradation or NF-κB activation

kinetics. We used subcellular fractioning and microscopy to determine that endogenous Card19 does not interact with endogenous Bcl10 upon CD8+ T cell restimulation. Through microscopy and proteinase K protection assays, we confirmed that endogenous Card19 is an outer mitochondrial membrane protein in BMDMs. We generated a murine retrovirus vector expressing zeocin-selectable myc-tagged Card19 and stably transduced immortalized *Card19 -/-* macrophages followed by zeocin selection. Mass spectrometry analysis of 3xMyc-Card19 expressed in the macrophage cell line revealed that Card19 interacts with MICOS proteins Mic19, Mic60, Mic25, Sam50, and Mtx2; we confirmed this interaction via immunoprecipitation and western blot. Finally, we employed TEM, Seahorse extracellular flux analysis, and flow cytometry to determine that absence of Card19 in BMDMs promotes indicators of mitochondrial dysfunction consistent with previous reports of MICOS defects, including abnormal cristae morphology, decreased oxygen consumption rate, increased mROS, and an increased population of mitochondria with decreased membrane potential. We propose that Card19 links protection against mitochondrial dysregulation with inflammation by regulating the Mic19-Mic60-Mic25 MICOS subcomplex.

TABLE OF CONTENTS

LIST OF FIGURES

CHAPTER 1: Introduction

CARD PROTEINS

Caspase activation and recruitment domains (CARDs) are conserved binding motifs that mediate protein-protein interactions; CARD containing proteins play key roles in both innate and adaptive immunity, including the intermediate steps of cell signaling cascades that occur downstream of T and B cell activation and in important antiviral signaling pathways (22).

General CARD overview

CARD proteins are a subfamily of the death domain (DD) superfamily, which contains a range of proteins that participate in programmed cell death signaling pathways and NF-κB activation (22; 126). All members of the DD superfamily are characterized by the presence of a domain containing 6 antiparallel α-helices (22; 126). The helices of the CARD subfamily in particular are diverse in length and orientation and contain a unique H1 helix that has been described as "fragmented" or "broken"; specifically, the H1 helix is divided into an H1a and H1b helix in close association with one another (22; 126). CARDs oligomerize into multimeric complexes and typically connect via linker domains to additional regulatory domains that confer sensor, scaffolding, or proteolytic functions. For example, some CARDs, such as Apaf-1, Nod1, and Nod2 contain nucleotide-binding domains (NBDs) which permit sensing of viral RNA and DNA, and others such as CARD9 contain coiled-coiled (CC) motifs in the C-terminus which promote and stabilize complex assembly; other CARDs include kinase or protease

domains (22). CARDs can self-oligomerize or associate with the CARD of other CARD proteins (22).

CARDs do not always interact with caspases, but many do participate in cell signaling pathways that involve caspase function. These processes include apoptosis and pyroptosis signaling, pathogen recognition receptor (PRR) signaling, and NF-κB activation. Apoptosis, which is required for cellular homeostasis and maintenance not linked to a strong inflammatory response, is a programmed cell death response (22; 126). Intrinsic apoptotic stimuli culminate in the formation of the apoptosome, a multimeric structure compromised of the CARD protein APAF-1, CARD protein Caspase-9, and mitochondrial protein cytochrome c (160). APAF-1 contains an NBD and acts as the scaffold for the apoptosome; Caspase-9 contains a protease which cleaves pro-caspases 3 and 7 to their active forms (160).

Pyroptosis, in contrast, is programmed cell death response explicitly linked to inflammation, as its pathway links PRR signaling to cell death concurrent with the release of IL-1β and IL-18 (110). Whereas apoptosis can occur in all cell types, pyroptosis is mostly limited to immune cells such macrophages, dendritic cells, and microglia (16). Pyroptosis signaling initiates the formation of the inflammasome, which contains CARD-containing caspase-1, scaffolding CARD protein PYCARD, and NLRP3 (110). Caspase-1 contains a protease domain which cleaves pro-IL-1β and pro-IL18 to the active forms; caspase-1 also cleaves Gasdermin D (GSDMD) to its active form, which then inserts and assembles a pore in the plasma membrane, thus effecting cell death and release of the pro-inflammatory cytokines (110).

CARDs can additionally regulate NF-κB transcription through both PRR signaling as well as through the association of multimeric complexes that form downstream of T cell receptor (TCR) or B cell receptor (BCR) engagement (22). Downstream of TCR or BCR activation, CARMA1/CARD11 oligomerizes with CARD protein BCL10 and paracaspase MALT1 (84; 129; 164; 191). These events initiate a phosphorylation cascade that culminates in NF-κB-mediated transcription (84; 129; 164; 191). NOD1 and NOD2 (also called CARD4 and CARD15, respectively), contain NBDs just as APAF-1 does; these PRRs detect moieties present in bacterial cell membranes and following activation will elicit NF-κB activation.

CARD proteins also link PRR sensing of intracellular viral RNA moieties to antiviral signaling. Cytoplasmic PRR CARD proteins RIG-I and MDA-5 detect intracellular viral dsRNA and, upon activation, associate with Mitochondrial antiviral signaling protein (MAVS) (137). MAVS then oligomerizes and promotes antiviral signaling by driving Type I Interferons through IRF-3 and NF-κB (137). MAVS has also been reported to bind caspase-8, which does not contain a CARD, to initiate apoptosis upon viral infection (42). Whereas most CARDs are cytosolic proteins, MAVS is one of two CARDs which are reported to localize to the mitochondria. CARD19, a newly identified CARD-containing protein, is also reported to localize to the mitochondria and endoplasmic reticulum in HEK293T cells (30). Additional CARD19 data is limited.

BinCARD/c9orf89/CARD19

The identification of CARD19 and its subsequent publication history has been tumultuous, and the protein has been through multiple naming iterations. CARD19 was first identified in a screen of the human EST database in an attempt to identify new

CARD proteins (196). In this screen, the published cDNA (NCBI accession number AK057716) was identified; its 228 amino acid protein product was expressed in a mammalian two-hybrid expression system to assess interaction with 26 CARD-containing proteins (196). The protein product of AK057716 was found to interact only with BCL10 in this screen, and this novel gene product was therefore named BCL10-interacting-CARD (BinCARD) (196). Alignment of AK057716 with the human genome sequence revealed 4 exons and an N terminus with high sequence identity to ced-3, caspase-1, caspase-2, caspase-4, caspase-5, and RAIDD (196). The N terminus was conserved across species; interestingly, the C terminus was not conserved across species (196).

Upon expression in HEK293T cells, BinCARD had an apparent cytosolic and nuclear localization (196). Co-expression of BinCARD with HA-BCL10 modestly inhibited NF-κB activation and decreased BCL10 phosphorylation in HEK293T cells (196). Overexpression in the human T cell tumor line, Jurkat, in conjunction with activation by PMA and Ionomycin, also suggested modest inhibition of NF-κB activation (196). BCL10 is a key component of the BCL10-CARMA1-MALT1 (CBM) complex, which assembles as an intermediate step after T cell receptor engagement (66; 84; 88; 106; 128; 129; 147; 164; 172; 191; 202). CBM complex assembly is required for the degradation of IκBα, which releases cytoplasmic NF-κB heterodimers, resulting in nuclear translocation and the resultant transcription of pro-proliferative genes (66; 84; 88; 106; 128; 129; 147; 164; 172; 191; 202). A large number of research studies have focused on how T cell receptor activation of NF-κB is regulated and limited after T cell activation. Such regulation is critically important, as unchecked T cell activation can be

associated with tissue damage and autoimmune disorders. The identification of BinCARD appeared to offer an answer to how the CBM complex is regulated post T cell activation.

A later publication reported that the mouse gene encodes one gene product, whereas the human gene C9orf89 is reported to encode 2 gene products (30; 138) (Figure 1). These gene products were named *BinCARD1* and *BinCARD2* (30). Whereas BinCARD1, the subject of the original study, was described as a cytoplasmic protein encoded by 4 exons, *BinCARD2* encoded a protein product with 6 exons, fewer amino acids, and a tentative transmembrane domain (30; 138) (Fig. 1A). Interestingly, BinCARD2 also displayed a mitochondrial and endoplasmic reticulum (ER) localization in HeLa cells (30). The N-terminus is virtually identical between BinCARD1 and BinCARD2; the differences in the gene products exist at the C terminus, downstream of the CARD, due to the differences in the numbers of exons and resultant open reading frames (ORFs) of these gene products (30). X-ray crystallography of the CARD in the N terminus uncovered a canonical CARD with 6 α-helices (30). Helices 2 and 3 are connected via a *cis*-peptide bond between Tyr39 and Pro40; the presence of a cis-peptide bond or a cis-proline is unique to BinCARD2 among CARD proteins and may act as regulator of CARD activity (30). The authors of this structural study also identified that the CARD contains three cysteines which can be fully oxidized, and two of the cysteines, Cys7 and Cys77 form a disulfide bond (30). Together these data suggest that the CARD of BinCARD2 could act as a redox sensor (30). Furthermore, a recent report presented evidence that siRNA silencing of BinCARD2 reduced IFNβ transcription induced by overexpression of MAVS, TBK1, or RIG-I-like Receptor ligands in HEK293T cells

(166). The siRNA knock-down of BinCARD2 also diminished *IFN β* and *IL-6* transcription induced by vesicular stomatitis virus (VSV) infection in A549 cells (166). BinCARD2 was reported to interact with MAVS, a CARD-containing protein localized to the outer mitochondrial membrane (166). We later confirmed that *BinCARD2* transcription was significantly higher than *BinCARD1* transcription, and only one protein product corresponding to the predicted size of the protein product of BinCARD2 was expressed (138). We concluded that BinCARD1 represented a spurious gene product and that BinCARD2 was the bona fide product of the *BinCARD* gene (138).

Publications have referred to CARD19 as BinCARD, BinCARD-1 and BinCARD-2. Furthermore, CARD19 has appeared under the name "C9orf89" in large scale screens. The widely accepted HUGO naming system refers to the gene and gene product as CARD19. To avoid the confusion that will arise from multiple names, we will exclusively use the HUGO naming convention.

There is little published data available on CARD19. Much of what we know is gleaned from public data bases, proteomics screens, and observations of phenotypes in *Card19 -/-* mice. For example, human and mouse databases indicate that CARD19 is highly expressed in bone marrow and cells of myeloid origin (46; 91; 161; 198). Additionally, in a screen measuring transcriptomics of cells in the murine neural system, CARD19 was most highly expressed by microglia, followed closely by myelinating and newly formed oligodendrocytes (206). Card19 has also appeared in at least three large scale screens available on PubChem. One such screen indicated that CARD19 is a positive regulator of LPS-induced TNF-α in THP-1 cells, which is a human macrophage cell line, but not in the mouse macrophage cell line RAW (100; 163). Another screen

indicated that CARD19 is a negative regulator of Parkin recruitment to mitochondria in HeLa cells (61). A third screen indicated that silencing of CARD19 may result in a synthetic lethal phenotype when coupled with E-cadherin in the human MCF10A cells (170). In all three screens, silencing of *CARD19* was either not significant in secondary screens, or was excluded from further analysis due to the candidate criteria of the respective publications. As such, the authors did not further investigate the role of CARD19 in any of the respective studies.

Card19 -/- mice injected with LPS exhibit higher serum levels of TNF-α, MCP-1, and IL-6 when compared to levels produced by *Card19 +/+* mice. (Fig. 1B). Macrophages are a major source of these cytokines in response to LPS stimulation. A 129 strain was extensively (≥13 times) back-crossed onto the C57BL/6 background. Our collaborators Dr. Igor Brodsky and Dr. Elisabet Bjanes then discovered that BMDMs isolated from *Card19 -/-* mice are resistant to a range of cell death stimuli. We confirmed this phenotype by measuring cell death induced by *Shigella flexneri* M90T infection in wild-type and knock-out BMDMs. Indeed, *Card19 -/-* BMDMs were significantly resistant to infection induced cytotoxicity, whereas avirulent control strain *Shigella flexneri* BS176 did not induce death in BMDMs of either genotype (Fig. 1C).

There is further insight into the function of CARD19 through BioPlex, a mass spectrometry proteomics screen effort which employs a combination of "bait" and "prey" proteins to identify potential interacting factors of all human proteins when expressed in HEK293T cells (68; 69; 149). CARD19 was reported to interact with several targets: TRAK1, TRAK2, CD244, PCNP, APOOL, SNRNP27, TMEM169, MTX2, HDDC3, EXOC6, MGARP, FAM3B, CRACR2B, and FAXC (Fig. 2A). Additional results of

proteins expressed in the intestinal epithelial cell line HTC116 yielded hits for TRAK1, TRAK2, CHCHD3, MTX2, and FAXC (Fig. 2B). Notably, CHCHD3 (also known as MIC19), APOOL (also known as MIC27), and MTX2, are all reported to interact with or be present in mitochondrial contact site and cristae organizing system (MICOS) complexes, which will be discussed in greater detail later in this introduction (44). Notably, an independent publication which employed AP-MS for a large scale screen of binding partners of FLAG-tagged MTX2 and MIC19 in HTC116 cells also indicated that CARD19 is pulled down with MTX2 (57). However, unlike in HEK293T cells, CARD19 did not pull down with MIC19 in HTC116 cells (57). There is limited overlap in CARD19-interacting proteins between these two cell lines, which may mean that the function of CARD19 is highly cell and tissue specific. No BioPlex data is available on CARD19 expressed in cells of a myeloid lineage.

MITOCHONDRIAL BIOLOGY

Mitochondria are bean-shaped, double-membraned organelles found in all eukaryotes; these dynamic "powerhouses of the cell" originated as endosymbionts from the bacterial phylum α-Proteobacteria. For years, mitochondria were relegated as mere tools that provide for the bioenergetic needs of the cell. However, it is evident that mitochondria are involved in much more than just bioenergetics: these organelles are vital cell signaling components that function directly or indirectly in a wide variety of pathways, including immunological signaling, redox and metabolic regulation, and cell death programming. Mitochondria have been implicated in inflammation, aging, neurodegeneration, and cancer; they are capable both of sensing danger within a cell and acting as the source of the danger itself.

The mitochondrion and its structure

Mitochondria are composed of two lipid bilayers, the outer mitochondrial membrane (OMM) and the inner mitochondrial membrane (IMM), as well as the intermembrane space (IMS) between the OMM and the IMM, and the gel-like core of the mitochondria called the mitochondrial matrix (MM) . While these organelles are generally described as "spherical" or "bean-shaped", the true morphology of the mitochondria varies depending on the cell type, tissue type, organism, and the inter- and intra-cellular environment. Most mitochondrial proteins are chromosomally encoded, transcribed, and translated in the cytosol, and then translocated through the OMM. Mitochondria also contain their own unique genomes (mitochondrial DNA; mtDNA), which encodes a limited set of proteins with mitochondrial-specific functions. Unlike nuclear DNA, mitochondrial DNA is circular. In mammals, the circular 16 kilobase mtDNA contains 37 genes which encode 13 proteins as well as tRNA and rRNA(20; 39; 195). The proteins encoded by mammalian mitochondria compose most of the proteins involved in oxidative phosphorylation (39).

Proteins of the OMM and IMM can either be anchored to the membrane via a transmembrane domain or peripherally associated with the membrane via interactions with other membrane-bound proteins. Lipids compose almost half of the molecules in the OMM (86). The most abundant proteins of the OMM are voltage dependent anion channels (VDACs), which are mitochondrial-specific porins which permit the passage of small molecules (5 kDa or smaller) when in "open" conformation (112). VDACs play a role in various cell processes but primarily function to conduct calcium into the mitochondria during apoptosis (112). The OMM also contains Sorting and Assembly Machinery (SAM) and Translocase of the Outer Membrane (TOM)

proteins (60; 174). Both SAM and TOM contain a combination of β-barrel proteins which insert into the OMM as well as peripherally associated membrane proteins which aid in chaperoning translocated proteins and scaffolding of complexes (60; 174). SAM and TOM proteins are crucial, in particular, for the insertion of other β-barrel proteins into the OMM (60; 174).

Proteins are incorporated into the mitochondria first by translocation through core TOM channels; β-barrel proteins are then incorporated into the OMM by SAM core proteins (60; 174). Proteins which will be translocated to the IMM are passed from the TOM to the Translocase of Inner Membrane (TIM) complex (60; 174). Because of the dramatic control TOM and SAM have over composition and biogenesis of mitochondria, and because TOM and SAM components can form functional complexes involved in other mitochondrial processes independent of translocation, these complexes are both directly and indirectly responsible for the integrity of the mitochondria (60; 174). Since the OMM is the only portion of the mitochondria that can come in direct contact with cytosolic proteins, the OMM also contains proteins associated with a variety of cytosolic signaling pathways. For example, the OMM contains key proteins involved in antiviral and type I interferon signaling, such as mitochondrial antiviral signaling protein (MAVS). The OMM also contains domains that make contact with the ER, which permits communication between the two organelles to regulate metabolism, calcium buffering, and cell death (95). Additionally, the outer mitochondrial membrane contains the factors which regulate mitochondrial turnover in response to various intrinsic stressors. OMM proteins OPA1 and MFN2, regulate mitochondrial fission and fusion, respectively. The OMM also contains proteins which recruit regulators of mitophagy;

specifically, PINK1 is stably displayed at the OMM upon a decrease in mitochondrial membrane potential (MMP), which initiates the mitophagy cascade.

Like the OMM, the IMM also contains phospholipids, predominantly cardiolipin (CL), which is also found in bacterial membranes; however, phospholipids compose only 20 percent of the IMM, whereas proteins make up other 80 percent (86). The IMM can be delineated into three parts – the inner boundary membrane (IBM), which is in relatively close contact with the OMM, separated only by the IMS. The average distance between the IMM and OMM is approximately 20 nm at the IBM (87). The IMM also forms invaginations into the MM (87). These invaginations are called cristae; it is within the cristae that components of the electron transport chain (130), which is responsible for oxidative phosphorylation, are contained (87). The IBM meets the cristae at the cristae junction (CJ). Cristae morphology changes in response to changes in mitochondrial stress, particularly metabolic demands. While complexes I through IV are located on the length of the cristae, complex V, the ATP Synthase responsible for the generation of ATP, is located in the crypt of the cristae (87). There is some biophysical evidence that there is a direct relationship between the curvature of the crypt of the cristae and the number of ATP Synthase dimers that can fit into the crypt, although it remains unclear whether cristae curvature or ATP Synthase dimers ultimately control this process (19; 34; 78). However, the above findings minimally imply that ATP generation by OXPHOS is, in part, regulated by cristae morphology. Cristae formation is largely regulated via MICOS, which will be discussed in more detail below (34).

Bioenergetics

Bioenergetics is a deeply complex process in mammalian cells. Unsurprisingly, there is feedback between virtually all metabolic cycles, in order to ensure cells are able to continue basic functions in the event that resources are scarce. It therefore is difficult to isolate individual metabolic cycles from each other. The overall goal of metabolic cycles is to generate ATP and cofactors which can be used in the cycles used to generate ATP.

Cellular (aerobic) respiration

Aerobic respiration refers to the generation of ATP in the presence of oxygen. Aerobic respiration is the most efficient cellular bioenergetic process in that it produces a high amount of ATP per molecule of glucose and involves several major pathways: Glycolysis, the Citric Acid Cycle (TCA, also called the Krebs' Cycle), beta-oxidation (also called fatty acid oxidation), and oxidative phosphorylation (Fig. 3). While glycolysis takes place in the cytosol, the TCA occurs in the mitochondrial matrix, and beta oxidation and oxidative phosphorylation occur at the IMM. Glycolysis and TCA produce a small net amount of ATP, and beta oxidation produces no net ATP, but the primary role of these cycles in aerobic conditions are, ultimately, to generate NADH and $FADH_2$ which may be used as proton donors in oxidative phosphorylation. In the presence of oxygen, cells tend to rely on oxidative phosphorylation to generate ATP. However, the Warburg effect, or aerobic glycolysis, has been reported in cancerous cell lines and has further been reported during the metabolic reprogramming of macrophages and T cells (14; 24; 29; 81; 89; 123; 124; 180; 189). Aerobic glycolysis provides cells with rapid ATP, albeit in a significantly less efficient fashion than oxidative phosphorylation.

Glycolysis

Glycolysis refers to the metabolic process that breaks down glucose in the cytosol. Glycolysis can occur in the presence or absence of oxygen; however, it is only during aerobic respiration that this pathway contributes to the TCA and oxidative phosphorylation. Glycolysis generates 2 pyruvate molecules which are shuttled into the mitochondrial matrix via Mitochondrial Pyruvate Carrier 1 and 2 to enter the TCA. Glycolysis of one glucose molecule yields 4 ATP, 2 pyruvate, and 2 NADH (2). Under anaerobic conditions or during aerobic glycolysis, pyruvate is further converted to lactate by lactate dehydrogenase (159) (178). Alternative fuel sources, such as galactose, can enter glycolysis, but result in a net yield of 0 ATP (142).

The Citric Acid Cycle

In the mitochondrial matrix, pyruvate generated via glycolysis is oxidized to acetyl-CoA, which enters the citric acid cycle. The TCA is an eight-step process in which acetyl-CoA is used to generate oxaloacetate (3; 194). A variety of cofactors and enzymes are involved, and by the end of the cycle the net products are GTP, 3 NADH, and 1 $FADH_2$ (3; 194). It is important to note that intermediate products of the citric acid cycle play a role in other metabolic processes, and likewise other forms of metabolism can feed into the citric acid cycle (3; 194).

Oxidative Phosphorylation

Oxidative Phosphorylation is the classic bioenergetic function that is associated with mitochondria. Oxidative phosphorylation generates ATP via the electron transport chain (130). In mammals, the ETC primarily consists of 5 complexes: Complex I (NADH Dehydrogenase), Complex II (Succinate Dehydrogenase), Complex III

(Ubiquionyl-cytochrome c Oxidoreductase), Complex IV (Cytochrome C Oxidase), and Complex V (ATP Synthase) (27). Multiple co-factors and co-enzymes are also involved in the ETC, including $FADH_2$, NADH, Coenzyme Q, and Cytochrome C (27). During aerobic respiration, an electrochemical gradient is formed by the successive reduction of oxygen across the complexes and the donation of protons from $FADH_2$ and NADH across the complexes into the intermembrane space. The reduction of oxygen is what powers the pumping of the hydrogens into the IMS; however, free radicals are formed during this process, and the mitochondrial reactive oxygen species (mROS) generated during this process are reduced by Complex IV to make H_2O, although there is typically escape of some reactive species (56; 59; 115). A high concentration of protons is generated in the IMS. The chemical gradient is restored when hydrogen flows from the IMS back into the mitochondrial matrix via ATP Synthase. The energy generated by this gradient permits the ATP Synthase to generate ATP from ADP and a phosphate group. One cycle of the ETC (when driven by glycolysis and the TCA) will yield 26 ATP.

Fatty Acid Oxidation

Fatty acid oxidation, also commonly called β-oxidation, is a process which occurs primarily in the mitochondrial matrix and can be used to produce cofactors to drive the ETC. Free fatty acids in the plasma are transported primarily as acyl-CoA molecules via fatty acid transport proteins (FATPs); once long and short chain fatty acids are in the cytosol, they are converted to acylcarnitine by CPT1 (65). This permits the acylcarnitine to enter mitochondria, which are acyl-CoA impermeable. Acylcarnitine is then reverted to acyl-CoA by CPT2 at the inner mitochondrial membrane (65). Fatty acid oxidation then proceeds according to a four-step reaction which yields trans-2-enoyl-CoA, which is

two carbons from its original carbon-chain length. This cycle is successively repeated resulting in shorter and shorter acyl-CoA chains (65). Every cycle produces, in addition to its acetyl- and acyl-CoA products, one molecule of NADH and one molecule of $FADH_2$ (65). NADH and $FADH_2$ will enter the electron transport chain. Acetyl-CoA is further degraded in the citric acid cycle, which further contributes co-factors for OXPHOS.

Mitochondrial reactive oxygen species

Mitochondrial reactive oxygen species (mROS) are reactive molecules formed during the electron transport chain; in order to pump Hydrogen ions across complexes from the mitochondrial matrix to the IMS to generate a chemical gradient, electrons are donated at the ETC complexes in a successive series of redox reactions. The membrane impermeable superoxide is formed via the series of reductions in the ETC and released to the mitochondrial matrix, where it is converted to another mROS, hydrogen peroxide, by mitochondrial superoxide dismutase (MnSOD) (114). Hydrogen peroxide is membrane permeable and may pass through to the IMS and cytosol, where it can further be converted to a hydroxyl ion. Superoxide can also exit the mitochondria via VDACs (58). Interestingly, there evidence that superoxide can be produced both at the mitochondrial matrix and in the IMS, especially superoxide produced by ETC Complex III (31; 59; 115; 155). ETC Complexes I and III are the source of the majority of mROS generated, although Complex II can be responsible for a significant portion of mROS upon calcium accumulation in the mitochondria (56; 71; 115; 155). While the mitochondria is able to control mROS via methods such as the aforementioned MnSOD as well as catalases and uncoupling family proteins (UCPs), increased mROS beyond mitochondrial control is a

major source of oxidative stress and is a major symptom and cause of mitochondrial dysfunction (114; 155). Uncontrolled oxidative stress has been linked to aging, neurodegenerative disorders, and inflammatory disease as well as forms of fibrosis (11; 47; 64; 97; 114; 119; 186). Additionally, mROS can play a key role in innate antibacterial and antiviral defenses (131). Toll-like receptor (TLR) 4 stimulation promotes mROS production through ECSIT and TRAF6, which helps control *Salmonella* infection (25). Furthermore, mROS can directly activate the NLRP3 inflammasome (62). The production of mROS also promotes MAVS dimerization both dependent and independent of viral infection (23; 118). Additionally, mROS produced by Complex III of the ETC are reportedly required for murine CD4+ T cell and CD8+ T cell activation and subsequent expansion (151).

MICOS

MICOS (sometimes called MINOS) refers to a series of inner membrane proteins, either peripherally localized or integral, which ultimately control the morphology of cristae. MICOS genes were first identified in yeast; yeast MICOS genes are largely conserved across species, with the exception of Mic12, which appears to have no animal homologs (44; 45; 70). Mammalian MICOS components include additional proteins; in all species, MICOS proteins oligomerize in distinct subcomplexes along with OMM proteins to control contact between IMM and OMM. These subcomplexes additionally regulate the number and size of cristae junctions. Control of the formation and size of CJs along with OMM-IMM contact ultimately controls the shape of cristae within mitochondria (205). MICOS components in mice and humans include MIC60 (or Mitofilin), MIC19, MIC25, MIC10, MIC13, MIC27 and MIC26 (44; 70). MIC60, along

with MIC10, MIC13, MIC26, and MIC27, is a membrane-bound IMM protein; MIC25 and MIC19, MIC60, and MIC10 are peripherally associated with the IMM via direct interactions with MIC60 (Fig. 4) (44; 70). Cristae morphology is regulated by oligomers formed between distinct subcomplexes. In *Saccharomyces cerevisiae*, distinct Mic12-Mic10-Mic27 and Mic60-Mic19 subcomplexes are linked by Mic19 (45). In human cells, however, MIC19-MIC60-MIC25 and MIC60-MIC26-MIC27-MIC10 subcomplexes are formed, linked by MIC60 (44; 49; 80; 182).

Subcomplex interactions are further regulated by MICOS-associated proteins in the IMM and OMM. The MIC19-MIC60-MIC25 subcomplex associates with OMM proteins SAM50, MTX2, and MTX1 (190; 200). This complex spans the IMS to form the intermembrane bridge (IMB) (168; 200). This subcomplex has further been reported to interact with chaperonin DNAjc11 (200). The MIC60-MIC19-MIC25 subcomplex and the IMB regulate cristae in response to mitochondrial stress. The formation of the IMB is mediated by the N-myristoylation of MIC19, which maintains its interaction with SAM50 (168; 177) . Upon physiological stresses, however, the IMS protease OMA1 is activated, cleaves this myristoyl group, and thus releases MIC19 from SAM50 (168) (Fig.4C). Furthermore, OPA1, an IMM GTPase which sequesters Cytochrome c and promotes mitochondrial fusion, has also been reported to interact with MIC19 and MIC60 to maintain cristae morphology (53). CHCHD2 and CHCHD10, which are orthologs of yeast Mic17, bind to MIC60 under conditions of mitochondrial stress as well. Specifically, CHCHD2 stabilizes upon decreased MMP and forms a complex with CHCHD10 (213). The specific role of these proteins in regulating MICOS via MIC60 is

unclear, although loss of either CHCHD2 or CHCHD10 was linked to activation of Oma1 and subsequent cristae distortion (213).

The MIC60-MIC27-MIC26-MIC13-MIC10 subcomplex, in contrast, does not regulate the interaction with the IMB in response to stress. Instead, this subcomplex appears to control the IMM landscape via control of cardiolipin (49; 190). MIC10 oligomerizes to control IMM curvature; the stability of these oligomers is promoted by MIC27, MIC13, and Cardiolipin but destabilized by MIC26 (6; 57; 133) . MIC26 and MIC27 in particular have an antagonist relationship (85; 133). Transient overexpression of myc-MIC26 or FLAG-MIC27 in 143B and HeLa cells reduced expression of endogenous MIC27 or endogenous MIC26, respectively (85). Double-knockouts of MIC27 and MIC26 lead to reduction of cardiolipin levels and destabilization of ETC subunits in HeLa and HAPI cells (6; 85).

Together, current data indicates that the two MICOS subcomplexes have discrete but cooperative functions. Loss of single MICOS components typically results in the destabilization of the respective subcomplex. Both the loss of individual MICOS components as well as overexpression of individual MICOS components are detrimental to mitochondrial health. Absence of MIC19, MIC60, MIC10, MIC26, and MIC27 individually have been reported to result in abnormal cristae morphology along with altered mitochondrial membrane potential (MMP), increased mROS (5; 36; 45; 49; 57; 133; 158; 200). Additionally, knockdown of individual MICOS proteins is linked to decreased oxygen consumption rate (OCR), which is often used as a surrogate measure of oxidative phosphorylation, and decreased ATP production, although this is not consistent across cell types and the alterations are often modest (36; 49; 158). Moreover, MICOS

defects have been linked to neurodegenerative disorders, such as ALS, Parkinson's Disease (PD) and Charcot-Marie-Tooth 2a (CMT2a) disease (94; 101; 102; 139; 171; 213). Despite evidence that indicates a role of MICOS in mitochondrial function and disease, however, investigations of MICOS components have been limited in scope. It is eminently apparent that MICOS function studies have been largely limited to cancer cell lines and findings performed in primary cells or animal models are likely to be far more nuanced and tissue specific. Undoubtedly, the metabolic state of these cell lines has an impact on the "normal" function and regulation of MICOS, especially considering that cell lines tend to rely heavily on glycolysis rather than OXPHOS to meet metabolic demands. Furthermore, there has been little data reported on MICOS in the context of immune cells and immune function.

Mitochondria as sources of and sensors for danger signals

Mitochondria are the key mediators of crucial steps in various cell signaling pathways. As such, these organelles play a role in immune and programmed cell death signaling. Apoptosis can be induced by either extrinsic stimuli (TNF-α, Fas) or through intrinsic stimuli (stress, nutrient deprivation, UV damage) (160; 183). Intrinsic apoptosis, and in some cell types, extrinsic apoptosis, each require the participation of the mitochondria. In particular, pro-apoptotic signaling proteins Bax and Bak insert into the outer mitochondrial membrane to initiate mitochondrial outer membrane permeabilization (MOMP) (52; 160; 183). While the specific mechanism and composition of MOMP pores is unclear, there is clear evidence that this event precedes mitochondrial dysfunction indicated by changes in MMP and increased production of mROS (160; 183). Importantly, MOMP is required for the release of cytochrome c from

the inner mitochondrial membrane to the cytosol, where it associates with APAF-1, triggers the oligomerization of the apoptosome, and thus permits execution of the cell (183). While mitochondria are not considered part of the canonical pyroptosis signaling pathway, there is now abundant evidence that mitochondria participate in driving pyroptosis (140; 212). Indeed, the increased production of mROS and the release of mtDNA is sufficient to activate NLRs, which oligomerize with pro-caspase-1 and sometimes additional CARD-containing scaffolding proteins, to form the inflammasome, which permits pyroptosis to occur (13; 62; 209). The mitochondria can produce these danger signals in response to triggers required for the priming of the inflammasome, such as TLR-4 engagement of LPS (62).

Inasmuch as mitochondria elicit danger signals that drive a number of cell signaling pathways, mechanisms of mitochondrial quality control (mitophagy, fission, fusion) play a significant role in reducing the danger signals elicited from mitochondria. As such, mitochondria can act as a danger rheostat; rather than participating in a "on/off" (digital) switch system, the mitochondrial signals which inhibit or promote cell death exist in a gradient (analog) system. In this cell signaling tug-of-war, execution of cell death depends on whether the cell is appropriately able to contain the danger signals from the mitochondria, or whether those danger signals exist at a sufficient threshold beyond the operating capacity of mitochondrial quality control mechanisms. Extensive evidence in particular demonstrates that mitophagy, which is selective autophagy directed at mitochondria and which is initiated by a unique signaling pathway, is particularly effective at counteracting both apoptosis and pyroptosis (90; 98; 105; 132; 165; 187; 188; 193; 199; 207; 210).

Unsurprisingly, because mitochondria have a potent capacity to regulate key signaling pathways via the release of danger signals, there are a range of pathologies and conditions that have been linked to mitochondria. Indeed, any failure in critical pathways that may drive mitochondrial dysfunction – excessive cell stress, deficiencies in mitochondrial quality control, or defects in the integrity of the mitochondria itself – can link mitochondrial dysfunction to disease. This is doubly true when mitochondrial dysfunction occurs in macrophages, which are major drivers of inflammation (90; 179; 187). Pro-inflammatory disorders such as ulcerative colitis, Crohn's disease, multiple sclerosis, and others have been linked to both mitochondrial dysfunction and defects in mitochondrial quality control (12; 111; 119; 127; 136; 143). Parkinson's Disease has been explicitly linked to both mitochondrial dysfunction and defects in mitophagy in neurons and microglia (51; 94; 109; 152).

IMMUNOMETABOLISM

As new evidence reveals the far-reaching consequences of cell metabolism and mitochondrial dysfunction on immune cells, there is heightened interest into the investigation of the impact of metabolic processes on immunity.

T cells

T cells, or T lymphocytes, are major drivers of adaptive immunity and are most notably distinguished by the expression of T cell receptors (TCRs) at the plasma membrane. Mature T cells are traditionally categorized by the mutually exclusive expression of CD4 or CD8 on the cell surface; thus, the two major subsets of mature T cells are CD8+ T cells (also called cytotoxic, killer, or effector T cells) and CD4+ T cells (or helper T cells). CD8+ T cells function to destroy infected host cells or tumor cells via

a range of lytic mechanisms, including Fas ligand signaling, and secretion of vesicles containing Perforin and Granzyme B; CD8+ T cells can also release some pro-inflammatory and pro-apoptotic cytokines such as TNF-α, IFN-γ, CCL5, and IL-17 (54; 82; 156). CD4+ T cells are classically grouped into numerated subsets based on cytokine expression and cell function. Differentiation from naïve to a specific class of helper T cell is dependent on which cytokines are expressed during T cell activation, which in turn drive helper T cell specific transcription factors. These groups include Th1, Th2, Th17, Tfh, and Treg cells (54; 82). Th1 cells are traditionally considered pro-inflammatory helper T cells which defend against intracellular pathogens (54; 82). Th1 cells produce IFNγ, which activate macrophages, and LTα/β, which initiate apoptosis/necroptosis (54; 82). Th2 cells facilitate activation of cells and processes that are required for expulsion of helminthic pathogens (54; 82). This cell type is also a major driver of allergy and asthma via promotion of IgE production by B cells (54; 82). Th2 cells produce IL-4 and IL-13 (54; 82). Th17 cells are increasingly appreciated as key pro-inflammatory subset that targets extracellular bacterial infections and drives neutrophil activation (54; 82). Notably, Th17 cells have also been shown to be protective against reinfection of cells by intracellular bacteria (150). Th17 cells produce various forms of IL-17 as well as IL-21 and IL-22 (54; 82). Follicular Helper T cells, or Tfh, are localized to the spleen, tonsils, and lymph nodes, where they drive both the development and maintenance of germinal centers and play a significant role in B cell selection, affinity maturation, and negative selection against autoreactive B cells (35; 54; 82). Regulatory T cells, or T regs,, can employ multiple mechanisms to suppress immune responses, including TGF-β and IL-10, CTLA4 expression, IL-2 consumption, and endonucleotidases CD39 and CD73; they are

indispensable for promoting peripheral self-tolerance and preventing autoimmunity (4; 32; 54; 75; 82; 141). All mature T cell subsets, upon activation, will differentiate into effector or memory T cells. Whereas effector T cells are short-lived, memory T cells are long-lived and generate an enhanced response in the event that they re-encounter their cognate antigen (54; 82).

Cellular metabolism of T cells

Given the energetic demands that are increased upon T cell activation, it is unsurprising that the metabolic state of T cells regulates function and survival. Naïve T cells are generally quiescent, with low-level metabolic activity necessary for homeostasis, which is primarily sourced from OXPHOS (24; 26; 29). Activation, however, leads to rapid differentiation and proliferation that drastically increases the energetic needs to the cells. Primary murine CD4+ and CD8+ T cells both display drastically increased aerobic glycolysis, although CD4+ T cells still tend to rely on both increased OXPHOS and glycolysis under these conditions, whereas CD8+ T cells are more heavily glycolytic (24). Interestingly, CD8+ T cells have been reported to have a greater capacity to proliferate and to be resistant to inhibition of proliferation induced by rotenone or 2-DG (24). Indeed, glucose uptake is a limiting factor in T cell activity, and the engagement of CD28 upregulates the expression of glucose transporter GLUT1 at the cell surface via Akt1 (26). Sustained aerobic glycolysis is similarly important for cytokine secretion and effector function: limiting glucose availability when activating CD8+ T cells inhibited both transcription and expression of IFN-γ (26). Metabolic programming further affects the ability of the host to limit T cell expansion via restimulation induced cell death (RICD); reducing available glucose or inhibiting glycolysis via 2-DG renders activated

CD8+ T cells less sensitive to RICD, and further that glycolysis in activated T cells induces FasL, which plays a role in apoptosis (89). Whereas activated T cells rely on aerobic glycolysis to fuel differentiation, proliferation and effector function, it has been reported that memory T cells, which are relatively quiescent, rely on fatty acid-fueled oxidative phosphorylation (28; 43; 72; 103; 130). However, the paradigm in which memory T cells rely on fatty acid oxidation to fuel oxidative phosphorylation is being challenged, since many studies rely on FAO inhibitors with off-target effects (134; 135).

T cell receptor signaling

While T cells vary greatly in effector function, many intracellular signaling mechanisms are common to all T cells. More specifically, current data suggest that the signaling pathway that initiates T cell activation via TCR engagement of naïve T cells is generally conserved across T cell types. Activation of naïve T cells requires two signals, or co-stimulation, to be effective (172). The TCR heterodimer, which contains the α and β TCR chains in complex with accessory CD3 γ, δ, ε and the ζ chain, binds peptide antigens displayed by the MHC complex expressed on antigen presenting cells (APCs) (172). Simultaneously, CD28, which is expressed on the surface of the T cell, binds to either CD80 or CD86, which is extracellularly expressed by APCs and upregulated due to stimulation of PRRs such as Toll-like receptors (TLRs), RIG-I like receptors (RLRs) and NOD/NOD-like receptors (NLRs), provides the co-stimulatory signal which permits T cell activation, thus acting as a safeguard against T cell activation by self-antigens (172). TCR engagement initiates a signaling cascade that drives expression of vital transcription factors that promote T cell proliferation and differentiation. Of note, transcription factors NF-κB and NFAT are required for sustained activation and proliferation (172).

While the events immediately following TCR activation are relatively well-studied, the intermediate steps of the TCR signaling cascade are less so. It is well-documented that TCR engagement promotes the association between three proteins: BCL10, MALT1, and CARD11, thus forming the "CBM" complex (172). BCL10 is a bipartite CARD protein with a serine- and threonine-rich domain immediately downstream of its N-terminal CARD (66; 88; 129; 202). CARD11, a multidomain scaffolding protein, contains a CARD and a CC motif, in its N terminus, along with the tripartite PDZ/SH3/GUK in its C terminus that is a common scaffolding motif (172). MALT1 is a paracaspase with proteolytic activity (88; 172). CBM complex assembly is followed by polyubiquination and phosphorylation of IKKγ, as well as phosphorylation of IKKβ (164; 172; 191). These post-translational modifications, in turn, lead to the terminal activation of the NF-κB signaling cascade, required for T-cell proliferation and function (84; 129; 164; 191). Following NF-κB activation, BCL10 is targeted for degradation, which ultimately limits T cell responses (106; 128; 147). While both macroautophagy and proteasomal degradation have been implicated in this process, the complete mechanism by which BCL10 is degraded is not fully defined (147).

Macrophages

Macrophages are white blood cells classically derived from monocytes in the bone marrow. They are the primary APCs, along with dendritic cells (DC), responsible for activation of T cells. Macrophages are named for their ability to phagocytose foreign organisms. They regularly sample their environment and present processed antigens to T cells. Macrophages are also major drivers of inflammation. Macrophages are traditionally classified according to functional phenotypes: unpolarized or M0

macrophages, M1 ("classically" activated) and M2 ("alternatively" activated) (14; 40; 73; 113; 117; 122; 157). M1 macrophages are activated and polarized by LPS via TLR4, as well as TNF-alpha and IFN-γ (73; 113; 117; 122). M1 macrophages display increased expression of TLR2 and TLR4, as well as proteins required for driving T cell activation (CD86, CD80, MHC-II) (73; 113). M1 macrophages produce key pro-inflammatory cytokines, including TNF-α, IL-1β, and IL-6; they also produce chemokines such as CXCL10 and CXCL9 (73; 113). Together, these signals recruit and activate additional immune cells including T cells, NK cells, macrophages, and DCs, thus amplifying the immune response at sites of infection. As such, M1 macrophages are downstream effectors of the Th1 drive cellular immune response. Due to the potent capacity of macrophages to drive significant inflammation, macrophages have been linked to a range of immune dysregulation disorders, in which these cells are either activated when it is inappropriate or drive pro-inflammatory responses that are not limited when necessary (90; 111; 187). In contrast, M2 macrophages are associated with wound healing and tissue homeostasis function that is mediated by suppressing inflammation and promoting immune suppression. IL-4 and IL-13 are sufficient to promote differentiation of M2 macrophages; additional cytokines such as IL-10 and TGF-β potentiate, but are not sufficient for, M2 polarization (40; 73; 113; 157). Experimentally, IL-4 alone is typically used to polarize M2 macrophages during *in vitro* culture of BMDMs (73; 113). M2 macrophages produce increased amounts of IL-10, TGF-β, and chemokines linked to T cell and neutrophil recruitment and activation (73; 113). M2 macrophage differentiation can be driven by Th2 cells. Although the M1 and M2 phenotypes are

readily polarized and defined *ex vivo*, realistically, the phenotypes likely represent two ends of an immunological spectrum, rather than truly distinct subsets.

Cellular metabolism of macrophages

Macrophages, like T cells, experience metabolic reprogramming in response to activation, and this reprogramming is dependent on whether the macrophage is being polarized to an M1 or M2 state. Unpolarized (M0) macrophages are somewhat quiescent and rely on OXPHOS for ATP production (7; 81; 120). LPS-stimulated polarization of M1 macrophages reprograms the cell to rely on aerobic glycolysis coupled with repression of OXPHOS (14; 81; 120). M1 macrophages exhibit glucose uptake, increased conversion of pyruvate to lactate, and induction of the pentose phosphate pathway (50). Elegant studies from the McVicar lab have demonstrated that LPS stimulation of M0 macrophage suppresses OXPHOS via increased production of Nitric Oxide (NO) (14). Interestingly, it appears that IL-10 is the main control for preventing the glycolytic commitment that occurs as a result of LPS priming (14). Upon LPS stimulation, IL-10 production is restricted via AMP Kinase activation, which in turn suppresses mTORC activation (14). While the Hypoxia inducible factor 1α (HIF1α) promotes metabolic reprogramming that induces IL-1β signaling via TCA substrate succinate, NO is responsible for rerouting pyruvate from pyruvate dehydrogenase (PDH), inhibiting mitochondrial aconitase (ACO2), and suppressing of the ETC (104; 123; 169). Murine M2 macrophages demonstrate increased fatty acid oxidation, which in turn fuels OXPHOS, although fatty acid oxidation is not required for M2 polarization in human macrophages (81; 116; 120). M2 polarization with IL-4 appears to be mediated through signal transducer and activator 6 (STAT6) which induces increased arginase activity

along with PPARγ-coactivator-1β (PGC-1β) (181). Interestingly, BMDMs isolated from mice with transgenic expression of PGC-1β reduced expression of IL-6 and IL-12p40 after stimulation with LPS and IFNγ relative to BMDMs isolated from wild-type mice (181). Interestingly, while M2 macrophages can readily repolarize to M1 macrophages, M1 macrophages do not readily repolarize to M2 macrophages, in part because of NO-induced mitochondrial dysfunction (179)

HYPOTHESIS AND AIMS.

The current evidence surrounding the function of CARD19 is limited. Although some data indicate that CARD19 regulates NF-κB activation via BCL10 degradation and may be a positive regulator for Type I interferon signaling via MAVS, these studies are limited to overexpression studies in human cell lines. It is also unclear how these studies are consistent with evidence from gene expression and interactome databases. We benefited from the observation that *Card19 -/-* mice injected with LPS display elevated levels of TNF-α, IL-6, and MCP-1, as well as the observation that some *Card19 -/-* mice spontaneously develop ataxia. Because the function of endogenous Card19 in relevant cell types remain unclear, the mechanism by which Card19 may mediate this phenotype on a cellular level remains unclear. Given that (i) Card19 is a mitochondrial protein; (17) abundant evidence indicates that mitochondrial dysfunction plays a role in driving inflammation; (iii) metabolism is a key regulator of immune function; and (iv) Card19 is highly transcribed in macrophages, we suspected that the paradigm of mitochondrial dysfunction may be present in immune cells (particularly macrophages) in the absence of Card19. To address this gap in knowledge, we examined the function of macrophages to elucidate potential function. We also examined the putative function of endogenous

Card19 as a driver of Bcl10 degradation and inhibitor of NF-κB activation in murine CD8+ T cells *ex vivo*. We chose to study this in the context of restimulation of primary murine CD8+ T cells because since CD8+ T cells readily expand and do not require differentiation culture during activation as CD4+ T cells do. CBM signaling downstream of TCR engagement is conserved across CD4+ T cells, CD8+ T cells, and B cells (84; 172). We hypothesize that Card19 regulates pro-inflammatory responses, not by driving degradation of the CBM complex in T cells, but by protecting against mitochondrial dysfunction.

Aim 1: Examine the role of Card19 in driving Bcl10 degradation after T cell restimulation *ex vivo*

Subaim 1a: Characterize the localization of Card19 in primary CD8+ T cells

Subaim 1b: Compare markers of T cell activation in *Card19* +/+ and *Card19* -/- T cells *ex vivo*

Aim 2: Determine the cellular function of Card19 in murine macrophages

Subaim 2a: Characterize localization and interacting partners of Card19 in macrophages

Subaim 2: Define the role of Card19 in mitochondrial dysfunction in macrophages

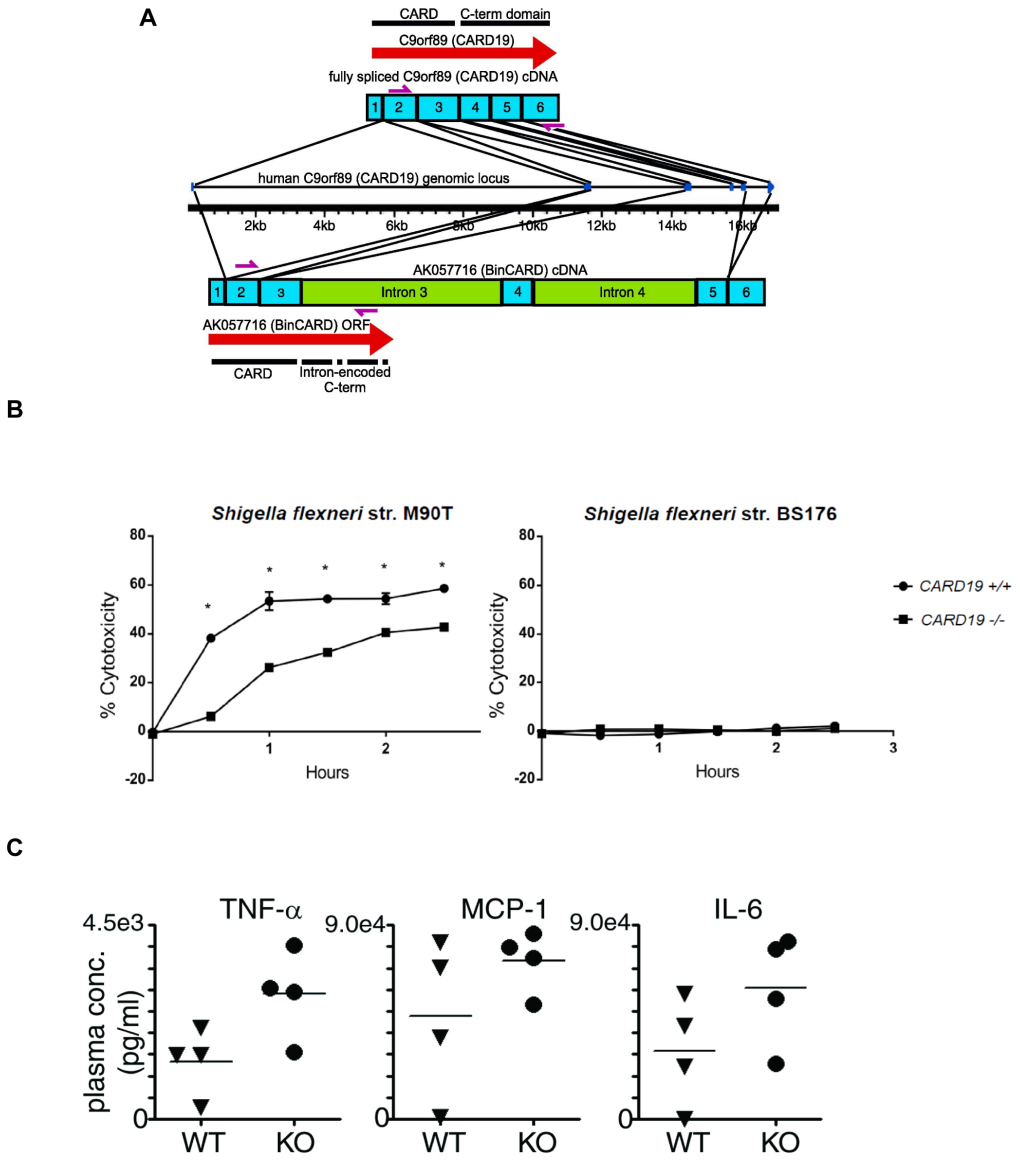

Fig. 1: Absence of Card19 promotes pro-inflammatory, macrophage-specific phenotypes. (A) The *CARD19* gene encodes an mRNA product containing 6 fully spliced exons; BinCARD1 originates from an incompletely spliced mRNA product containing intron 3 and intron 4. (B) Card19 -/- BMDMs are resistant to cell death induced by Shigella infection relative to Card19 +/+ BMDMs; avirulent strain BS176 does not induce cell death. Cell death was measured by LDH release at 0, 30, 60, 90, 120, and 150 minutes post-infection. (C) Card19 -/- mice injected with LPS display elevated serum levels of TNF-α, IL-6, and MCP-1 relative to Card19 +/+ mice; cytokine level were detected via ELISA. While differences between wild-type and knock-out cytokine levels were not statistically significant, the cytokine levels from the knock-out mice were at least one-standard deviation above historical controls performed by Lexicon. For characterization of ataxia, see Appendix 1.

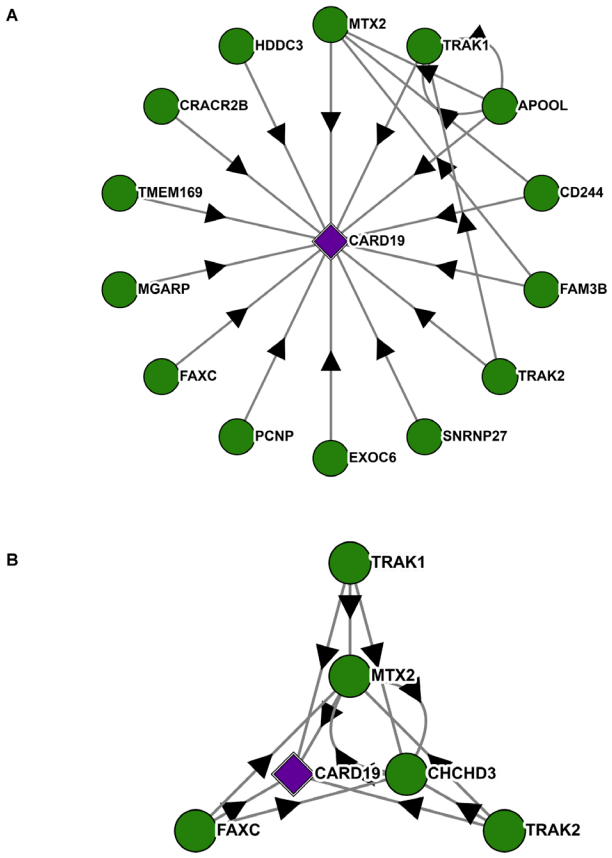

Fig. 2. BioPlex Interactome of Card19 in (A) HEK293T and (B) HTC116 cells. Circles indicate "bait" proteins, diamonds indicate "prey" proteins. Arrows indicate the bait-to-prey directed edge. Notably, there is little overlap between the proteins that are reported to interact with CARD19 in HEK293T cells versus HTC116 cells, indicating that there may tissue-specific function of CARD19. These schematics were reproduced from the BioPlex database (68; 69; 149).

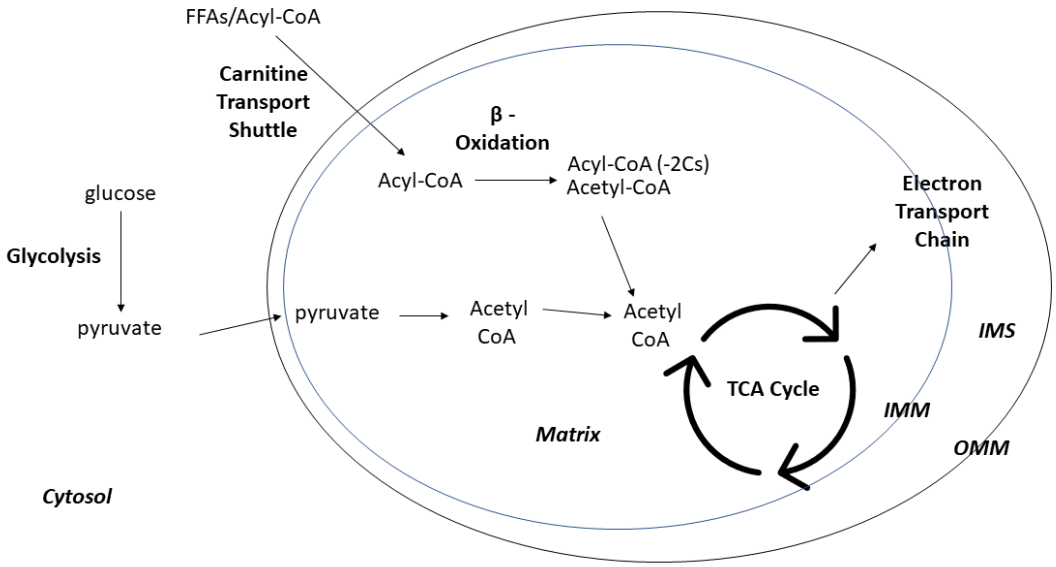

Fig. 3. Aerobic Respiration

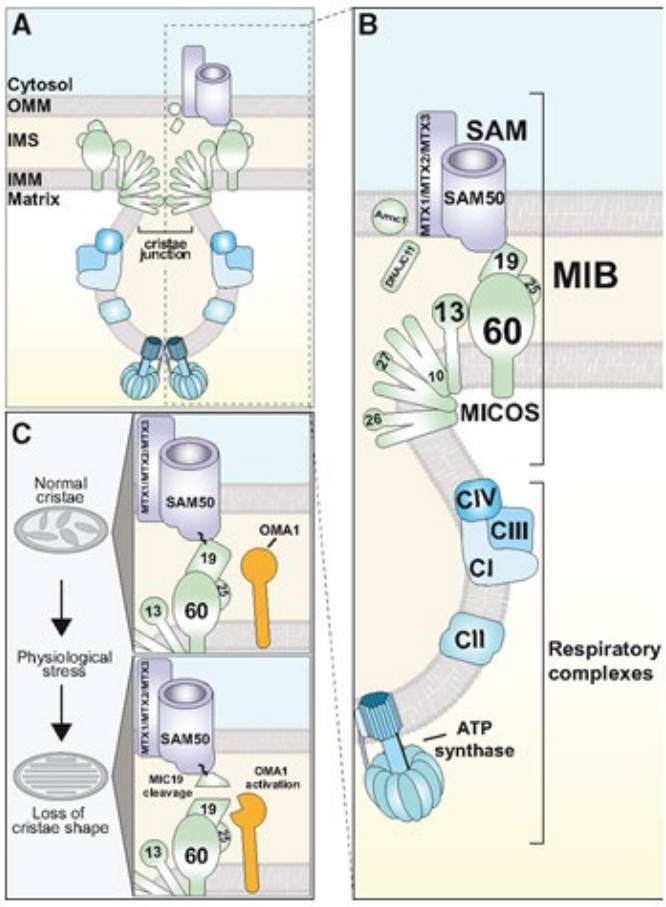

Fig. 4: Schematic Representative of Cristae and the MICOS Subcomplexes.
(A) Schematic representation of the OMM, IMM, and cristae. Purple proteins are components of the OMM; green proteins are components of the IMM; blue proteins are the complexes of the ETC. (B) SAM50 and metaxins span the IMS to interact with MIC19 to form the intermembrane bridge. (C) Mitochondrial stress induces OMA1 cleave of MIC19, disrupting the IMB and inducing the formation of distorted cristae. Reproduced and adapted with permission from (44) and Oxford University Press.

CHAPTER 2: Materials and Methods

CARD19−/− MICE

The Card19−/− strain was purchased from Lexicon Pharmaceuticals and extensively backcrossed to C57BL/6. In this strain, Card19 was inactivated by replacement of exons 3–6 (encoding amino acids 51–183, encoding the C-terminal half of the CARD and the entire Card19 C-terminus) with a Bgeo-puro cassette resulting in a truncated, non-functional Card19 protein fragment. Characterization of immune cell development and mature immune cell subsets by Lexicon Pharmaceuticals and our group has revealed no significant differences versus wild-type controls.

ISOLATION AND CULTURE OF CD8 T CELLS

To isolate CD8 T cells, lymph nodes and spleens were harvested from C*ard1*9+/+ and *Card19*−/− mice between 6 and 10 weeks of age. Organs were transferred to isolation buffer (2% FBS, 0.6% sodium citrate, 1× PBS), followed by dissociation through 70 μm mesh filters. Spleen samples were centrifuged in RBC Lysis buffer for 5 min and washed twice in isolation buffer. Lymph node and spleen samples were then consolidated and pipetted gently through a 40 μm filter to remove DNA released by lysed red blood cells. Lymphocytes were quantified and CD8+ T cells were isolated using the CD8+ T cell Dynabeads kit (Thermofisher) according to the manufacturer's instructions. Isolated CD8+ T cells were then seeded on anti-CD28 (1 ug/ml) and either anti-TCRβ or anti-CD3ε (100 μg/ml) wells in a 24 well plate, at a density of 1.3×10^6 cells per well in Eagle's Ham's Amino Acids (EHAA) medium supplemented with 10% fetal bovine

serum. After 48 h of stimulation, T cell blasts were harvested from the wells and cultured as described [16]. In indicated experiments, *Card19*−/− CD8 T cells were harvested from wells after 48 h of stimulation and subjected to retroviral transduction for 2 h at 1200×g at 32 °C. Polybrene was added to the retroviral supernatant (final concentration 10 μg/ml) to increase the efficiency of the transduction. 24 h after transduction, the transduced cells were passaged in zeocin (50 μg/ml) for 5 days to select cells stably expressing 3×FLAG-Card19. The Institutional Animal Care and Use Committee at Uniformed Services University (43) approved all animal procedures.

TCR STIMULATION OF MOUSE CD8+ T CELL BLASTS

CD8+ T cell blasts (see above) were seeded in 24 well plates coated with either anti-CD3ε or anti-CD43 (non-stimulatory control) for the times indicated. T cells were cooled on ice, collected, and centrifuged at 4 °C, and pellets were resuspended in 1× Laemmli buffer. Whole cell lysates were boiled for 5 min and subjected to sonication to shear genomic DNA. Samples were quantified via Nanodrop One/One using the Pierce 660 nm Protein Assay Reagent supplemented with IDCR. Equal amounts of total protein were loaded for each sample.

GENERATION AND CULTURE OF MACROPHAGE AND FIBROBLAST CELL LINES

To generate the immortalized macrophage cell line, peripheral blood was obtained from *Card19* +/+ mice (or splenocytes from *Card19* -/- mice). Blood or splenocytes were treated with RBC lysis buffer, washed in 1X PBS, and cultured in a non-tissue treated 24 well plate in DMEM with 10% Cosmic Calf Serum, L-Glutamine, and Penicillin/streptomycin supplemented with GM-CSF for 4 days. The cells were transferred into plates coated with Retronectin (50 μg/ml) and transduced with viral

supernatant containing a replication-deficient multi-cistronic vRaf/vMyc lentivirus vector called LIVeMac by spinning for 90 minutes at 1000xg at 32 ºC. The cells were incubated in viral supernatant for 2 more hours in a 32 ºC incubator, then viral supernatant was removed, washed once with 1X PBS, and the viral supernatant replaced. After 4 days of culture, cells were seeded in 50% conditioned media, 50% fresh DMEM with 10% Cosmic Calf Serum, L-Glutamine, and Penicillin/streptomycin supplemented with GM-CSF at $2X10^5$ cells per well in a 24 well plate. After 3 days, cells were removed from the wells via trypsinization and seeded in a new 24 well plate in 100% fresh DMEM with 10% Cosmic Calf Serum, L-Glutamine, and Penicillin/streptomycin supplemented with GM-CSF. After 7 days, dead cells were removed by washing the well with 1X PBS and replaced with DMEM that does not contain GM-CSF. After 2 weeks, 200 µg of Cytodex 1 beads were added. After 1 week, cells were split by removing the beads with adherent cells and placing them in a new well with fresh beads. The number of beads were slowly reduced during every split until the cells adhered to the flask and multiplied without the beads. See (9) for patent details.

To generate the fibroblast cell line, lungs were harvested from *Card19* +/+ and *Card19* -/- mice. The lungs were cut into pieces with a razor; the pieces were then incubated in a solution of DMEM supplemented with 10% heat inactivated FBS and glutamine containing 3 mg/ml Collagenase I for 45 minutes at 37 ºC. The digested pieces were then filtered through a 70 µm strainer, pelleted by centrifugation at 500xg for 5 minutes, and seeded in 10 ml of DMEM supplemented with 10% heat inactivated FBS and PSGG in a 100 mm petri dish. The cells were allowed to adhere for 2 weeks, after which the cells were collected and moved to 1 well in a 6 well plate, and then passaged

by trypsinization every 3 days for 3 months. Macrophage and fibroblast cell lines were passaged in DMEM supplemented with 9% heat-inactivated FBS, 4.5 g/ml D-glucose, 4 mM glutamine, 1 mM sodium pyruvate, along with penicillin, gentamicin, and streptomycin. When galactose-supplemented media was used, glucose-free DMEM supplemented with 10 mM D-galactose, 9% heat-inactivated dialyzed FBS, 4 mM glutamine, 1 mM sodium pyruvate, along with penicillin, gentamicin, and streptomycin.

GENERATION AND TRANSDUCTION OF TAGGED CARD19 AND MIC19 CONSTRUCTS

A murine EST, CB193298, which included a complete ORF was used to design nested PCR primers to clone the ORF from primary T cell cDNA. The murine Card19 ORF was also used to search the non-redundant GenBank nucleotide database, identifying the human homolog of Card19 as the fully spliced product of gene *C9orf89*. A murine EST for Mic19 was also used to design nested PCR primers to clone the Mic19 ORF. Card19 cDNA and Mic19 cDNA were subcloned from the initial destination vector (pBluescript) into pcDNA3. Mutant derivatives were made via PCR site-directed mutagenesis or Quikchange (Agilent) site-directed mutagenesis and subcloned into pcDNA3. Tagged forms of Card19 (3xFLAG, 3xMyc, RFPt) or Mic19 (3xOLLAS) were generated by excising the Card19 or Mic19 constructs with restriction enzymes, ligated with cDNA containing the respective tags excised with restriction enzymes, and finally transformed into chemically competent DH5α. Finally, tagged constructs were subcloned into zeocin selection vector pSQZ.

To generate retrovirus for transduction, HEK293-T cells were subjected to calcium-phosphate transfection. 2.4 μg of the retroviral plasmid containing the construct was mixed with 0.6 μg of helper plasmid pCL-Eco, 7.5 μl of 2.5 M $CaCl_2$, and 75 μl

ddH_2O. The mixture was then added to75 µl of 2X HEPES. Exactly one minute after mixing with the 2X HEPES, the solution was added to the HEK293-T cells in a dropwise fashion. Twenty-four hours after the transfection, 1.5 ml of DMEM is added to the transfected wells. Viral supernatant is harvested 48 hours after transfection, flash-frozen on dry ice for twenty minutes, and stored at -80ºC.

To transduce the macrophage cell line, cells were seeded at fifty-thousand cells per well in a 24 well plate and allowed to adhere overnight. On the day of the transduction, wells containing cells were aspirated. Thawed viral supernatant containing 10 ng/ml polybrene were added to the appropriate wells. The cells were subjected to spinfection for 2 hours at 1200×g at 32ºC. After the spinfection, the viral supernatant was aspirated and replaced with fresh DMEM. After 24 hours, the transduced cells were split and subjected to the appropriate selection reagent, Zeocin or Hygromycin. Transduced cells were not used for experiments until they had undergone selection for at least five days and untransduced cells were no longer viable after grown in selection media.

WESTERN BLOTTING

CD8+ T cells, immortalized macrophages, or subcellular fractions were pelleted and resuspend in Laemmli buffer containing β-mercaptanol, followed by boiling for 5 min and shearing by sonication. Equal amounts of lysate were run on 4-20% Tris-glycine gels and transferred using a TransBlot onto nitrocellulose membranes. Membranes were blocked with 5% milk in TBS with 0.1% Tween. The following antibodies were used: rabbit anti-myc (Bethyl); rabbit anti-HA (Y-11), rabbit anti-Bcl10 (H-197), mouse anti-GAPDH (6C5), mouse anti-A20 (A12), rabbit anti-TOM20; mouse anti-β-actin (C-4),

mouse anti-Mfn2 (XX-1), mouse anti-HSP60 (H-1), rabbit anti-Tom20 (FL-145), mouse anti-PCNA (F-2) (all from Santa Cruz); mouse anti-FLAG (M2) (Sigma-Aldrich); rabbit anti-phospho-IκBα (Ser32) (14D4); rabbit anti- IκBα (Cell Signaling Technologies); rabbit anti-CARD19 (HPA010990), rabbit anti-SAMM50 (HPA034537) (Atlas Antibodies); mouse anti-MCPIP1 (anti-Regnase) (MAB7875) (R&D Systems); mouse anti-mitofilin (2E4AD5), rabbit anti-Calnexin (Abcam); rabbit anti-RFP (Rockland); and mouse anti-α-tubulin (purified from DSHB hybridoma AA4.3 supernatant; AA4.3 Hybridoma deposited by Walsh, C).

(43)ISOLATION AND CULTURE OF BMDMS

Card19 +/+ and *Card19 -/-* mice were euthanized by cervical dislocation on Day 0. The tibia and pelvis were dissected, and the bone marrow was flushed from the bones with 1X PBS using a 27 gauge need and syringe. The bone marrow was then filtered through a 70 μm filter and the cells pelleted by spinning 500xg for 5 minutes at 4 ºC. The pelleted cells were resuspended in 10 ml 1X PBS; 5 ml of the cell suspension was then carefully layered on 5 ml of Lymphocyte Separation Media and spun 500xg for 20 minutes at room temperature. The fraction containing the isolated cells were removed with a serological pipette and washed three times with ice-cold 1X PBS. The cells were then seeded $5X10^6$ cells per dish in 100 mm petri dishes in 30% L929 supernatant in DMEM. After 4 days of culture, half of the media was removed and replaced with fresh DMEM with 30% L929. On day 7 post-harvest, the BMDMs can be removed from the bottom of the dishes by trypsinization, counted, and seeded as appropriate in non-tissue culture treated dishes for use between days 7 and 10 post-harvest.

MICROSCOPY

Primary CD8+ T cells from *Card19* +/+ or *Card19* -/- mice were isolated and cultured as described above. Cells were seeded for 20 min on glass coverslips coated with 100 µg/ml poly-D-lysine and 100 µg/ml anti-CD3ε or anti-CD43 for 20 min. Cells were fixed and prepared for microscopy as described in (129). For BMDMs or the macrophage cell line, cells were seeded on sterile glass coverslips and allowed to adhere overnight. Mouse anti-ATP Synthase β (4.3E8.D10) (Thermo Fisher); rabbit anti-CARD19 (HPA010990) (Atlas Antibodies); rabbit anti-Calnexin (Abcam); mouse anti-FLAG (M2) (Sigma Aldrich); mouse anti-Mfn2 (XX-1); mouse anti-Bcl10 (331.3), mouse anti-Calnexin (E-10) and mouse anti-MAVS (E3), rabbit anti-Tom20 (FL-145) (all from Santa Cruz) and anti-OLLAS. Goat anti-rabbit (H + L) Alexa Fluor 647, Goat anti-mouse (IgG1) Alexa Fluor 488 and Goat anti-mouse (IgG2a) Alexa Fluor 488 (Thermo Fisher) were used at a 1:200 dilution. To directly conjugate mouse anti-Myc and mouse anti-OLLAS antibodies to AlexaFluor 647 and AlexaFluor 488, respectively, we used AlexaFluor 488 and AlexaFluor 488 Antibody Labeling Kits (Thermo Fisher Scientific) according to the manufacturer's instructions. For confocal microscopy, coverslips were mounted in Fluoromount G and imaged using a Zeiss 710 2P Confocal Microscope or a Zeiss LSM 980 Confocal Microscope with a 63× oil objective. Images were processed using Zeiss Zen Blue software; representative insets of individual cells were selected, and single representative z-planes were exported as TIFFs. For SIM, coverslips were mounted in a glycerol-based mounting medium and imaged using a Zeiss ELYRA PS.1 with a 63× oil objective. Images were processed and aligned with Zeiss Zen Black software. Representative insets of individual cells and single representative z-planes were exported

as TIFFs. For some insets, maximum intensity projections were generated from select z-plane ranges with ImageJ. Merged images were prepared using Adobe Photoshop.

SUBCELLULAR FRACTIONATION

Cell fractions were prepared using a Qiagen mitochondria isolation kit. CD8+ T cell blasts (7.5×10^6 cells per condition) were untreated or stimulated with 100 μg/ml anti-CD3ε in one well of a 6-well plate per condition. Mitochondria were isolated according to the manufacturer's protocol, and the cytosolic fraction and microsomal fractions were saved. The subcellular fractions were then diluted 1:1 in 2× Laemmli buffer, boiled, and sonicated. Total protein in all saved fractions was quantified via Pierce 660 nm Protein Assay Reagent supplemented with IDCR. Equal quantities of total protein from each subcellular fraction were analyzed via western blotting as described above.

IMMUNOPRECIPITATION

For immunoprecipitation results to be analyzed via mass spectrometry: *Card19 -/-* macrophages expressing 3xMyc-Card19-WT were lysed for 30 minutes in 400 μL lysis/wash buffer with rotation at 4ºC. Lysis/wash Buffer composition is 50 mM Tris-HCl, pH 7.5, 150 mM NaCl, and 1% Triton-X 100. Commercially available cOmplete™ ULTRA protease inhibitor tablets (Millipore Sigma, #5892970001) and PhosSTOP™ phosphatase inhibitor tablets (Millipore Sigma, #4906845001) were used in the lysis/wash buffer according to the manufacturer's protocols. The lysed cells were then pelleted for 10 minutes at 10,000xg at 4ºC; the supernatant was transferred to fresh Eppendorf tubes and the pellet was disposed. 3xMyc-Card19 was then immunoprecipitated with Myc-Trap agarose beads or negative control agarose beads

(ChromoTek) according to the manufacturer's protocols. Immunoprecipitated samples were resuspended in 100 µl Laemmli buffer with 0.1 mM DTT and boiled for 5 minutes at 100ºC. Samples were stored at -80ºC and shipped overnight on dry ice for mass spectrometry analysis.

For immunoprecipitation to be analyzed via western blot: $5.0X10^6$ *Card19 -/-* immortalized macrophages that were untransduced or stably expressing 3xMyc-Card19-WT, 3xMyc-Card19-G73R, or 3xMyc-Card19-Δ146 were pelleted, washed with ice-cold 1X PBS, pelleted again, and resuspended in 400 ul of lysis/wash buffer. Lysis/wash buffer composition was the same as used for immunoprecipitation for mass spectrometry. Samples were lysed for 30 minutes on ice, with vortexing of the sample every 10 minutes. The lysed cells were then centrifuged for 10 minutes at 10,000xg at 4ºC. The supernatant was transferred to fresh Eppendorf tubes and the pellets discarded. During the lysis step, a Sepharose G beads were prepared. Briefly, a 1:1 solution of Sepharose G beads was washed 3x in lysis/wash buffer. The transferred lysate was then precleared by adding 10 µl of the 1:1 Sepharose G bead suspension to the lysate and rotated end-over-end for 45 minutes at 4ºC. The suspension was centrifuged for 1 minute at 15,000xg at 4ºC; the pre-cleared supernatant was carefully transferred to a fresh Eppendorf tube, leaving the pelleted Sepharose G beads. 2 µg of mouse anti-myc (9E10) was added to the supernatant and rotated end-over-end at 4ºC for 16 to 20 hours. 10 µl of the 1:1 Sepharose G bead suspension were then added to the antibody-treated supernatant and rotated end-over-end at 4ºC for 45 minutes. The supernatant was centrifuged for 1 minutes at 15,000xg for at 4ºC. The Sepharose G bead pellet was carefully washed 3x with 900 µl lysis/buffer; the beads were resuspended in wash by careful pipetting and

inverting the tubes. The Sepharose G beads were then resuspended in 50 µl lysis/wash buffer and 50 µl 2X Laemmli buffer containing 5% v/v β-mercaptanol, boiled for 5 minutes at 100ºC. The beads were pelleted, and the supernatant was transferred to fresh Eppendorf tubes, leaving the Sepharose G beads. Samples were homogenized by sonication and stored at 20 ºC.

MASS SPECTROMETRY

All mass spectrometry preparation and analyses were performed by Dr. Thomas Conrads and Dr. Ming Zhou at the Inova Schar Cancer Institute/WHIRC. Samples collected by immunoprecipitation separated via electrophoresis and stained with SimplyBlue Safe stain (Invitrogen). The lanes were then excised, dried, and subjected to in-gel trypsin digestion, followed by extraction in 70% acetonitrile, 5% formic acid. Peptides were dried, resuspended in 0.1% trifluoroacetic acid (TFA) analyzed via LC-MS/MS (Easy-nLC 1000 with Q Exactive MS) (ThermoFisher Scientific) (Orbitrap Fusion Lumos Tribid mass spectrometer) (Thermo Fisher Scientific) as described in (8), with some modest differences. The Easy-Spray ion source capillary voltage and temperature were set at 2.0 kV and 275ºC, respectively. Data was searched against the myc-Card19 protein sequence combined with a Swiss-Prot mouse protein database ((http://www.uniprot.org/uniprot/) using Proteome Discoverer (v.2.2.0.388, Thermo Fisher Scientific) with the automatic decoy search option set followed by false-discovery rate processing by Percolater. Data were searched with a precursor mass tolerance of 10 ppm and a fragment ion tolerance of 0.05 daltons (Da), a maximum of two tryptic miscleavages, and dynamic modifications for oxidiation (15.9949 Da) in methionine residues and phosphorylation (79.9663 Da) on serine, threonine, and tyrosine residues.

TRANSMISSION ELECTRON MICROSCOPY

For BMDMs, cells were isolated and differentiated as described above. On day 7 post isolation, $4X10^6$ BMDMs were seeded in a 100 mm petri dish and allowed to adhere for 3 hours. The LPS treated cells were then stimulated with 100 ng/ml LPS for 1 hour. All cells were collected by trypsinization, washed with 0.1 M cacodylate buffer, and pelleted. The pellets were fixed in 2% glutaraldehyde in 0.1 M cacodylate buffer supplemented with 2 mM calcium chloride and 2 mM magnesium chloride at pH 7.4 for 2 hours at room temperature. The cells were then stained with 1% osmium tetroxide and 1% uranyl acetate, dehydrated, and embedded in Agar resin.

Fibroblasts were prepared and imaged as described above, but 1X PBS was used as wash buffer instead of 0.1 M cacodylate buffer, and the 2% glutaraldehyde fix was also prepared in 1X PBS. Fibroblasts were not treated with LPS but were grown in DMEM without glucose and supplemented with 10 mM D-galactose, 4 mM glutamine, and 1 mM sodium pyruvate for 5 days prior to collection and fixation. Eight to fifteen 70-80 μm sections were cut and imaged for serial sectioning. All images were taken with the JEOL-JEM1011 transmission electron microscope.

FLOW CYTOMETRY

On day 7 post-harvest, BMDMs were lifted from the well via trypsinization and seeded at $5.0X10^5$ cells per well in non-tissue culture treated 6-well plates. On day 8 post-harvest, cells were treated with the indicated reagents, then lifted from the well via trypsinization for 2 minutes at 37 ºC. The cells were pelleted in 5 ml polystyrene FACS tubes, washed, and resuspended in warm DMEM with heat inactivated FBS containing MitoSox Red or MitoTracker Green and TMRE for 25 minutes 37 ºC. The cells were

then washed twice in room temperature 1X PBS and resuspended in 1X PBS containing either UV or Yellow Zombie Fixable Viability Dye (BioLegend) for 15 minutes at room temperature. The cells were washed three times in ice cold PBS with 0.1% heat inactivated FBS and kept on ice and protected from light. Samples were measured immediately following the staining protocol using a LSRII Orange Flow Cytometer (BioLegend) and analyzed with FlowJo.

SHIGELLA INFECTION OF BMDMS

Shigella flexneri strain M90T or its plasmid cured derivative BS176 were inoculated from tryptic soy broth (TSB) - agar plate colonies into TSB and grown overnight 37 ºC with shaking (225 rpm). BMDMs were seeded at $7.0X10^4$ cells per well in a 96 well plate and allowed to adhere overnight. The next day, M90T and BS176 were subcultured at 1:100 in 3 ml TSB at 37 ºC with shaking (225 rpm) for 2 hours to an OD_{600} between 0.5 and 0.6. Prior to infection, the BMDMs were washed once with DMEM and the media replaced with DMEM containing 1% heat inactivated FBS. M90T and BS176 were added to the appropriate wells in the 96 well plate with the BMDMs at an MOI of 30. The plates were spun at 4000xg for 2 minutes at 37 ºC and incubated. At the indicated timepoints, media from the wells were collected and transferred to a new 96 well plate and kept on ice. Upon completion of the assay, 96 well plate containing the transferred media was spun for 10 minutes at 1000xg at 4ºC and carefully transferred to a fresh 96 well plate, avoiding touching the bottom of the wells. Supernatant was stored at -20 ºC.

LDH ASSAY

To measure cytotoxicity induced by LPS+ATP or *Shigella* infection in BMDMs, LDH release was measured using an LDH Cytotoxicity Detection Kit (TaKaRa) according to the manufacturer's instructions. 50 µl of supernatant and 50 µl of detection mix per well were used instead of 100 µl of each per well in a clear 96 well plate. The reaction was stopped via the addition of 100 µl 1M HCl after 30 minutes of incubation at room temperature. The samples were protected from light during the incubation. Immediately after stopping the reaction, the absorbances of the wells were measured at 490 nm. BMDMs treated with 1% Triton-X 100 for the corresponding times of the time course were used as a 100% cytotoxicity control. Media without cells were used as a 0% cytotoxicity control. Percent cytotoxicity was calculated using the following formula:

$$\%\, Cytotoxicity = \frac{sample - background}{(Trixon - X\ 100\ - background)} \times 100$$

SEAHORSE EXTRACELLULAR FLUX

The night before the assay, a Seahorse XFe96 sensor cartridge (Agilent) was rehydrated in 200 µl ddH_2O per well overnight at 37ºC in a standard incubator without additional carbon dioxide. The morning of the assay, BMDMs were collected, pelleted, and resuspended in fresh complete DMEM. The cells were then filtered through a 70 µm filter to eliminate cell clusters and seeded at $5.0X10^4$ cells per well in a 96-well Agilent cell culture plate. The cells were allowed to adhere to the plate for 1 hour at room temperature, to promote formation of a monolayer. The cells were then incubated for another 6 hours in a 37ºC incubator. DMEM, pH 7.4, without phenol red (Agilent) was supplemented with 10 mM D-glucose (Agilent) and 1 mM sodium pyruvate and warmed to 37ºC. 2 hours prior to the assay, the ddH_2O used to rehydrate the sensor cartridge was replaced with 200 µl Seahorse assay calibrant (Agilent) and returned to the standard

incubator at to 37ºC. 1 hour prior to the assay, the BMDMs were washed with the specially prepared assay DMEM 1X and replaced with 180 µl assay DMEM per well. The 96 well plate containing the cells were then incubated in the standard 37ºC incubator without additional carbon dioxide. During this time, oligomycin A, FCCP, and rotenone/antimycin A from the Mito Stress Test kit (Agilent) were prepared in assay DMEM according to manufacturer's instructions. The reagents were further diluted to 100X working stocks in assay DMEM. 20 µl of oligomycin A, 22 µl of FCCP, and 25 µl rotenone/antimycin A were added to the A, B, and C drug ports, respectively, of each sensor in the sensor cartridge. The sensor cartridge was then inserted into a pre-warmed Seahorse XFe96 (Agilent), and the machine was calibrated and initialized automatically. Immediately prior to the assay, the cell media was replaced with 180 µl fresh assay DMEM, the plate was inserted into the Seahorse XFe96, and the assay was initialized. OCR and ECAR were measured 3 times immediately after mixing for 3 minutes at basal levels, and 1 minute after the addition of each drug. Final drug concentrations were 1.5 µM oligomycin A, 1.5 µM FCCP, 0.5 µM rotenone and antimycin A. Results were calculated and reported using the Mito Stress Test report generator from Agilent. Calculations for the Mito Stress Test Report parameters are as follows:

$$Basal\ Respiration = (Last\ rate\ measurement\ before\ first\ injection) - (Non - mitochondrial\ respiration\ rate)$$

$$Maximal\ Respiration = (Maximum\ rate\ measurement\ after\ FCCP\ injection) - (Non - mitochondrial\ respiration\ rate)$$

$$Percent\ Spare\ Respiratory\ Capacity = (\frac{Maximal\ respiration\ rate}{Basal\ Respiration}) \times 100$$

$$ATP\ Production =$$

$$(Last\ rate\ measurement\ after\ Oligomycin\ injection) -$$

$$(Minimum\ rate\ measurment\ after\ Oligomycin\ injection)$$

PREPARATION OF MOUSE BRAIN SECTIONS FOR IMMUNOCHEMISTRY

After mice were euthanized via cervical dislocation, the brains were harvested and fixed in 4% paraformaldehyde for 48 hours at 4ºC. The brains were then washed in 10 ml of 1X PBS for 4 hours and incubated successively in 15% and 30% sucrose for 24 hours each at 4ºC. The brains were then embedded in OCT mounting media (Fisher Healthcare) in cryomolds, flash frozen on dry ice, and stored at -80ºC until sectioned. 40 µM sagittal and coronal sections were cut via a Leica CM1850 UC Cryostat (Leica Biosystems) and mounted on coverslips.

IMMUNOCYTOCHEMISTRY AND ANALYSIS OF BRAIN SECTIONS

To stain the brain sections, sections were fixed for 5 minutes in 2% paraformaldehyde for 5 minutes at room temperature, then blocked with 10% goat serum in PBS and 0.2% Triton X-100 for 1 hour at room temperature. Sections were stained with primary rabbit anti-iba1 (Wako), rabbit anti-GFAP, or Alexa Fluor 555 mouse anti-neuronal nuclei (NeuN) (Thermo Fisher Scientific. Secondary antibodies used were Alexa Fluor goat anti-rabbit 647 or Alexa Fluor goat anti-rabbit 488 (Thermo Fisher Scientific). Covers were mounted on the sections, sealed with Fluoromount G, and allowed to dry for 30 minutes. Slides were stored at -20ºC.

TAPE REMOVAL TEST

We adapted a tape removal test developed by the McCabe lab; we were trained in the protocol by Michael Nieves. Mice were subjected to 5 days of training prior to the test to reduce variability. Briefly, red and yellow electrical tape was cut into pieces 2mm by 4mm in size. For every test, there were two sequential trials. In trial 1, yellow tape was placed on the right forepaw and red tape on the left forepaw. In trial 2, yellow tape was placed on the left forepaw and red tape is placed on the right forepaw. Yellow tape was always placed first, and red tape is always pressed to secure the tape first. After placing and securing the tape, the mouse was placed into a tall, transparent cylinder. The time to notice and the time to remove each piece of tape was measured with a stopwatch. Each individual trial was video recorded.

DIGIGAIT GAIT ANALYSIS

Mice were placed in the DigiGait compartment with a mouse-specific camera installed. Just before the treadmill was turned on, the light in the compartment was turned on, and the treadmill was slowly increased to 14 mph. Once the mouse was running consistently, the recording was begun and at least 4 seconds of uninterrupted steps were collected. After the video was collected, the automatic snout filter was applied, and the file was shortened to contain 4 seconds of video data. Individual gait corrections were made to each file by comparing the graphed gait data to the video for every paw, in order to ensure that there were no errant “steps” that needed to be removed or were actually one step detected as two steps. Finally, the DigiGait Analyzer calculated various metrics regarding the gait of each mouse.

STATISTICS

For comparison of TNF-α, IL-6, and MCP-1 serum levels between *Card19* +/+ and *Card19* -/- mice following LPS injection, two-way unpaired T-tests that assumed a non-Gaussian distribution with a confidence interval of 95% were performed. For tape removal tests, two-way unpaired T-tests that assumed a non-Gaussian distribution were performed, couple with a Mann-Whitney U test. For Seahorse Extracellular and *S. flexneri* cytotoxicity experiments, 2-way ANOVA tests followed by Bonferroni post-tests were performed using GraphPad Prism v.7.0 software. For all figures, error bars represent standard deviation (std) unless otherwise indicated.

CHAPTER THREE: Results

AIM 1: EXAMINING THE ROLE OF CARD19 IN DRIVING BCL10 DEGRADATION AFTER T CELL RESTIMULATION EX VIVO

Previous reports indicated that CARD19 specifically interacted with BCL10 after TCR engagement (196). Upon T cell activation, CARD19 appeared to drive BCL10 degradation and therefore limit NF-κB activation in Jurkat T cells and HEK293T cells (196). Additional data indicated that CARD19 is localized to the mitochondria (30). However, there were no available published data assessing the localization of endogenous Card19 in T cells, nor was there published data confirming the role of Card19 as a CBM regulator in primary T cells. Therefore, we investigated the putative role of Card19 as a driver of Bcl10 degradation after TCR engagement in primary murine CD8+ T cells isolated from *Card19* +/+ and *Card19* -/- mice.

Card19 is a mitochondrial protein in CD8+ T cells

Because there are two previous reports that indicated that Card19 is localized to the mitochondrial when overexpressed in HEK293T cells, we first sought to identify the localization of endogenous Card19 in CD8+ T cells. We chose to focus on CD8+ T cells because these are simpler to culture compared to CD4+ T cells, which require additional culturing conditions to promote helper T cell differentiation. CBM complex assembly downstream of TCR engagement is conserved in CD8+ T cells, CD4+ T cells, and B cells. Briefly, CD8+ T cells were isolated from *Card19* +/+ mice; after 48 hours of stimulation with anti-CD3ε and anti-CD28, the T cells blasts were passaged in media containing IL-2. The CD8+ T cells were seeded on coverslips coated with poly-D-lysine and co-labelled with anti-Card19 and one of three mitochondrial markers: anti-Mfn2,

anti-ATP Synthase β, or anti-Mavs (Fig. 5). Mavs and Mfn2 are both OMM proteins, whereas ATP Synthase β is located in the crypts of the IMM. The slides were then imaged via confocal microscopy using either the Zeiss 710 2P (Figures 5B-C) or the Zeiss 980 (Fig.5A) . Upon close examination of individual cells, it was apparent that endogenous Card19 displayed the same distribution as the mitochondrial markers and generally localized with all three mitochondrial markers, as well. Like the mitochondrial markers, Card19 displayed a punctate appearance. To confirm that endogenous Card19 labeling was not due to nonspecific binding, we also stained *Card19* -/- CD8+ T cells for endogenous Card19 and either Mfn2 (Fig. 6A) or Mavs (Fig. 6B). We found that there was there was a small amount of background Card19 signal in *Card19* -/- CD8+ T cells, but not an abundant signal as is apparent in the *Card19* +/+ CD8+ T cells. This background signal could be due either to clustered secondary antibody that was not sufficiently washed away during the microscopy protocol; alternatively, it could be that the polyclonal rabbit anti-Card19 antibody is interacting with residual truncated Card19 in the cytosol of the *Card19* -/- CD8+ T cells. In contrast, Mfn2 and Mavs were readily visible.

Due to the resolution limit of the confocal microscope used for this experiment, we were unable to effectively quantify colocalization. To confirm the mitochondrial distribution of Card19, we employed structured illumination microscopy (SIM) to yield better resolution of Card19 staining. Labeling of endogenous Card19 did not yield staining sufficiently strong enough to use in SIM imaging; therefore, we transduced CD8+ T cells isolated from *Card19* -/- mice with a retroviral construct that expressed 3×FLAG-tagged Card19. Prior to our SIM studies, FLAG-tagged Card19 was expressed

at similar levels as endogenous Card19, exhibiting bright, specific FLAG staining, whereas untransduced *Card19* -/- CD8+ T cells had little or no staining with either anti-FLAG or anti-Card19 (Fig. 7A). We confirmed that the FLAG-tagged Card19 construct displayed a similar distribution pattern as endogenous Card19. After confirming that 3×FLAG-Card19 appropriately co-stained with anti-Card19 and was expressed at similar levels as endogenous Card19, we performed SIM image of *Card19* -/- CD8+ T cells transduced with 3×FLAG-Card19 and labelled with anti-Card19 and anti-ATP Synthase β. The robust staining revealed 3×F-Card19 and ATP Synthase β in close association with each other (Fig. 7B). Interestingly, within individual mitochondria, ATP Synthase β appeared to constitute the "core" of the mitochondria, whereas Card19 seemed to wrap around the ATP Synthase β (Fig. 7B, inset). Apparent colocalization only occurred in distinct areas of the mitochondria. Additionally, Card19 staining had a distinct punctate appearance, rather than exhibiting a pattern of continuous staining around the entire mitochondria.

While endogenous Card19 distributed with various mitochondrial markers, a previous report indicated that Card19 also localized to the ER in HeLa cells (30). Therefore, we assessed via confocal microscopy whether endogenous Card19 also localized with Calnexin, a marker of the ER. We found that while Card19 and Calnexin were in close proximity to each other, the staining did not appear to colocalize (Fig. 8A). When examining signal-channel images of co-stains, it is apparent that Card19 staining is not present in the "gaps" left by the Calnexin staining, and vice-versa. We again confirmed that *Card19* -/- CD8+ T cells exhibited no Card19 signal but clear Calnexin staining. To further validate these results, we performed subcellular fractionation with

the Qproteome mitochondrial isolation kit (Qiagen) in *Card19 +/+* and *Card19 -/-* CD8+ T cells either treated with anti-CD43 or restimulated with anti-CD3. We examined the microsomal fraction – which contains plasma membrane, endoplasmic reticulum, and unbroken cells – with organelle markers via western blotting. We found that Calnexin, an ER marker, is enriched in the microsomal fraction (Fig. 8B). In contrast, were no bands from the cytosolic marker Gapdh or cytosolic protein Bcl10 (Fig.8B). There were low intensity bands for Pcna (nucleus), Tom20 (mitochondria) and Card19, indicating there was a small amount of contamination of other organelles in the microsomal fraction (Fig. 8B). The Card19 band intensity was so low that it likely is simply present because of mitochondrial contamination and not because it is an integral part of the ER. Therefore, Card19 may make contact the ER, as mitochondria commonly contacted and regulated by the mitochondrial associated membrane (43) of the ER; however, endogenous Card19 is clearly localized to the mitochondria in CD8+ T cells.

Absence of Card19 has no impact on markers of NF-κB activation

While CARD19 has been reported to directly interact with BCL10 and drive its degradation *in vitro*, there have been no reports confirming this function in primary cells when Card19 is expressed at an endogenous level. Therefore, we isolated CD8+ T cells from *Card19 +/+* and *Card19 -/-* mice and stimulated the cells for 48 hours with anti-CD3ε and anti-CD28. The T cell blasts where then lifted from the wells and passaged in media containing IL-2 for one week. The CD8+ T cells then were restimulated in wells coated with anti-CD3e for 0, 20, 40, 60, and 120 minutes and measured markers of NF-κB via western blot (Fig. 9A). We chose to study makers of T cell activation upon restimulation in CD8+ T cell blasts because culturing CD8+ T cell blasts provided us

with a greatly increased number of T cells available for our experiments. CARD19 has been shown to drive BCL10 degradation after CBM complex assembly and thus limit NF-κB activation in Jurkat T cells. We thus postulated that when Card19 is absent, Bcl10 levels will progressively increase and markers of NF-κB will increase as well, since there is no mechanism to limit CBM complex assembly. Surprisingly, we found that there was little difference in the markers of T cell restimulation and NF-κB activation between *Card19* +/+ and *Card19* -/- CD8+ T cells (Fig. 9A-B). Bcl10 readily degrades by 20 minutes of anti-CD3 in both genotypes; resynthesis is apparent by 120 minutes of stimulation (Fig. 9A). To detect NF-κB activation, we measured both IκBα and p-IκBα. IκBα is degraded upon TCR engagement and releases NF-κB to translocate to the nucleus. Phosphorylation of IκBα increases over time in response to TCR engagement as a feedback mechanism to limit NF-κB activation (Fig. 9A). IκBα was readily degraded by 20 minutes and resynthesized in both *Card19* +/+ and *Card19* -/- T cells. Moreover, p-IκBα reached its peak expression by 60 minutes in CD8+ T cells of both genotypes (Fig. 9A). Interestingly, it appeared that at 120 minutes, *Card19* -/- T cells had somewhat less Bcl10 and IκBα synthesis as well as less p- IκBα by 120 minutes post-restimulation, indicating that *Card19* -/- T cells had somewhat less NF-κB activation (Fig. 9A). We further confirmed this trend by measuring two additional markers: A20, which is a negative regulator of NF-κB, and Regnase B, which is cleaved by Malt1 in a manner dependent on Bcl10. CD8+ T cells of both genotypes achieved peak Regnase B cleavage by 120 minutes post-stimulation. *Card19* -/- CD8+ T cells appeared to have modestly less Regnase B cleaved relative to *Card19* +/+ CD8+ T cells (Fig. 9A). Both genotypes also exhibited increased A20, reaching maximum expression at 120 minutes

post-restimulation (Fig. 9A). Once again, *Card19* +/+ CD8+ T cells showed more A20 at 120 minutes relative to *Card19* -/- CD8+ T cells. Overall, both *Card19* +/+ and *Card19* -/- CD8+ T cells displayed similar kinetics of NF-κB; the only perceptible difference was decreased expression of NF-κB activation markers in the *Card19* -/- cells.

To better assess the activation kinetics of the CD8+ T cells, we quantified western blot results of Bcl10, IκBα, A20, and p-IκBα, normalized them to β-actin expression, and expressed the intensities as a ratio of the intensity of the untreated sample in each group (Fig. 9B). These results confirmed that *Card19* +/+ and *Card19* -/- CD8+ T cells exhibited the same kinetics of Bcl10 and IκBα degradation and resynthesis as well as A20 and p-IκBα expression (Fig. 9B). Furthermore, these quantifications indicated that *Card19* -/- CD8+ T cells had modestly less resynthesis of Bcl10 and IκBα by 120 minutes post-restimulation, as well as less A20 and p-IκBα expression at 120 minutes (Fig. 9B). We also measured Card19 expression by Western blots, quantified these results, normalized them to α-tubulin, and expressed the intensities as a ratio of Card19 expression in the untreated sample (Fig. 9C). Card19 expression did not vary significantly at 0, 20, 40, 60, and 120 minutes post-restimulation, indicating that Card19 expression does not significantly change after TCR engagement. Together, these data indicate that absence of Card19 does not affect Bcl10 degradation or NF-κB activation kinetics.

Endogenous Card19 does not colocalize or co-fractionate with Bcl10 in primary murine CD8+ T cells

Because our data indicated that absence of Card19 did not result in accumulation of Bcl10 or elevated NF-κB activation, we examined whether endogenous Card19 colocalizes or co-fractionates with endogenous Bcl10 in CD8+ T cells. We first isolated

CD8+ T cells from *Card19* +/+ mice; after 48 hours of stimulation with anti-CD3ε and anti-CD28, the cells were passaged in media with IL-2 for one week. The cells were then seeded on coverslips coated with either anti-CD43 or anti-CD3ε and restimulated for 20 minutes. The cells were co-stained with anti-Card19 and anti-Bcl10 and analyzed via confocal microscopy. As expected, Bcl10 staining was diffuse in the cytosol, but after 20 minutes of restimulation, Bcl10 punctae were visible (Fig. 10A). In both untreated and restimulated conditions, Card19 did not appear to colocalize with Bcl10 (Fig. 10A). Although some of the Bcl10 punctae appear to be in close association with Card19, this observation may reflect the limited space in the cytosol as well as the limits of the resolution of confocal microscopy.

To support and extend our confocal microscopy results, we repeated our restimulation assay with the *Card19* +/+ CD8+ T cells; we then collected the cells and isolated the mitochondria using a mitochondrial isolation kit, collecting each of the fractions. We confirmed the separation of the cytosolic fraction and mitochondrial fraction via Tom20, an OMM marker, and Gapdh, a cytosolic marker (Fig. 10B). Bcl10 was limited to the cytosolic fraction while Card19 was limited to the mitochondrial fraction, regardless of whether the cells were treated with anti-CD43 or anti-CD3ε (Fig. 10B). This data, coupled with the results from the confocal microscopy, suggest that endogenous Card19 does not interact with endogenous Bcl10, before or after T cell restimulation.

AIM 2: DEFINE THE CELLULAR FUNCTION OF CARD19 IN MURINE MACROPHAGES

According to public gene expression databases, Card19 is highly transcribed in cells of myeloid origin (46; 161; 176). Additionally, we have observed that *Card19* -/-

mice injected with LPS display increased levels of macrophage-specific cytokines relative to their *Card19* +/+ counterparts. Because mitochondrial dysfunction has been linked to inflammation, and because Card19 has been reported to have a mitochondrial localization in other cell types, we sought to examine the cellular function of Card19 in murine macrophages.

Card19 is an outer mitochondrial membrane protein in macrophages, with its N-terminus exposed to the cytosol

Card19 has been demonstrated to have mitochondrial localization in several cell types. However, because Card19 has not been studied in macrophages, we first sought to confirm that Card19 is a mitochondrial protein in macrophages. To this end, we performed SIM on BMDMs isolated from *Card19* +/+ and *Card19* -/- mice. We labelled the BMDMs with anti-Card19 and either anti-Mavs (Fig. 11A) or anti-ATP Synthase β (Fig. 11B), and we found that Card19 distributed with both mitochondrial markers. Upon closer examination of individual mitochondria, Card19 exhibited a distinct punctate appearance, whereas Mavs and ATP Synthase β exhibited a continuous staining pattern (Fig.11A/B). Card19 colocalized with both Mavs and ATP Synthase β in individual mitochondria, although it appeared that Card19 colocalized more with Mavs in the OMM, whereas the Card19 staining was wrapped around ATP Synthase β of the IMM (Fig. 11A/B). This indicates that Card19 is a mitochondrial protein; furthermore, this is consistent with our observations of endogenous Card19 in *Card19*+/+ CD8+ T cells (Fig.5A-C) and 3×FLAG-Card19 in *Card19* -/- CD8+ T cells (Fig. 7B).

We could not clearly identify whether Card19 was an OMM or IMM protein based on our SIM analysis alone, as the limits of resolution of SIM would not permit an appropriate differentiation. To elucidate whether Card19 was localized to the outer or

inner mitochondrial membrane, we expressed 3×FLAG-Card19-TagRFP-T in a fibroblast cell line derived from primary lung fibroblasts isolated from *Card19 -/-* mice. We then isolated the mitochondria, performed Proteinase K protection assays, and analyzed the results via western blot. Mfn2, an OMM protein, was readily degraded in the presence of proteinase K, whether the treatment occurred in isotonic buffer, swelling buffer, or 0.1% Triton X-100 (Fig. 11C). Mic60, an integral IMM protein, was resistant to degradation in isotonic buffer, but in the presence of swelling buffer, which produces mitoplasts by permeabilizing the OMM, Mic60 was more readily degraded; in the presence of Triton X-100, Mic60 was fully degraded (Fig. 11C). Hsp60, an MM marker, was resistant to digestion in both isotonic and swelling buffer but was completely degraded in Triton X-100 (Fig. 11C). We then probed for FLAG and TagRFP-T; the FLAG tag was expressed on the N terminus, whereas the RFP tag was expressed on the C terminus. We found that both the FLAG tag and RFP tag readily degraded in isotonic buffer, swelling buffer, and Triton X-100, indicating that Card19 is an OMM protein (Fig. 11C). Furthermore, the RFP tag appeared to be somewhat resistant to the proteinase K digestion relative to the FLAG tag, which suggests that the N-terminus is exposed to the cytosol, whereas the C terminus is exposed to the IMS (Fig. 11C). Together, these data indicate that endogenous Card19 is an OMM protein in macrophages.

The *Card19* protein contains a transmembrane domain and a mitochondrial targeting sequence in its C terminus

To characterize the functional domains of Card19, we expressed several 3×FLAG-tagged mutant Card19 mutants in a cell line derived from macrophages isolated from the spleen of *Card19 -/-* mice. We expressed full-length Card19, along with G73R, a point mutation at a conserved glycine residue that has been shown to be required for

function in other CARDs; ΔTM, a deletion of the putative transmembrane domain; Δ130, which contains a partial deletion of the transmembrane domain and all of the C terminus; and Δ146, which left the transmembrane intact but deleted the majority of the C terminus (Fig. 12A). To analyze the localization of these proteins, we co-stained the cells with anti-FLAG and anti-Tom20, a marker of the OMM, and imaged the cells using SIM. Both full-length Card19 and G73R colocalized with Tom20; these constructs also displayed a punctate appearance, similar to the appearance of endogenous Card19 in BMDMs (Fig. 12B). In contrast, ΔTM and Δ130, were diffuse in the cytosol and nucleus, thus confirming the function of the putative transmembrane domain (Fig. 12B). Interestingly, the Δ146 mutant did not colocalize with Tom20; however, it clearly did not exhibit a diffuse cytosolic/nuclear distribution (Fig. 12B). We postulated that the Δ146 mutant localized to the endoplasmic reticulum. To determine if this was correct, we imaged co-stained the cells with anti-FLAG and anti-Calnexin and imaged with SIM (Fig. 13). We found that the full-length and G73R constructs exhibited a punctate distribution that was in close association with, but did not colocalize with, Calnexin (Fig. 13). As before, ΔTM and Δ130 displayed a cytosolic distribution and did not distribute with Calnexin (Fig. 13). However, Δ146 did strongly distribute with Calnexin (Fig. 13), perhaps indicating that the distal C-terminus contains a previously unidentified mitochondrial targeting sequence (MTS).

3xMyc-Card19 associates with MICOS and MICOS-interacting proteins in macrophages

After confirming that full length Card19 is indeed a mitochondrial protein, we sought to identify potential interacting partners of Card19 in macrophages. To date, there is no published proteomics data on Card19 interacting partners; there are only

public results available from mass proteomics screens, which did not specifically examine Card19 in macrophages. To define the interaction partners of Card19 in macrophages, we transduced the *Card19 -/-* macrophage cell line with a retroviral construct expressing 3×Myc-Card19. We then performed immunoprecipitation using the Myc-Trap Agarose kit from ChromoTek; the results were analyzed via mass spectrometry by our collaborators Dr. Thomas Conrads and Dr. Ming Zhou at the Women's Health Integrated Research Center (WHIRC) at Inova (Fig. 14A). We found that Card19 specifically interacted with several MICOS interacting proteins, including Sam50, Mic19, Mic25, Mtx2, and Mic60 (Fig. 14A). The strongest peptide results were Sam50 and Mic19. The association between Card19 and Sam50, Mic19, Mic25, Mtx2, and Mic60 were consistent across multiple mass spectrometry experiments performed with various specificity controls. Importantly, Sam50 and Mtx2 have previously been reported to interact with Mic19, and thus indirectly with Mic60 and Mic25, to form the IMB and Mic19-Mic60-Mic25 MICOS subcomplex (168; 200). The combination of mass spectrometry and previous findings in the literature strongly suggest that Card19 interacts with specific components of the MICOS complex. Notably, neither Mavs nor Bcl10 were detected as Card19-interacting partners by mass spectrometry, although they have been reported to interact with Card19 in previous publications (30; 196).

To confirm the results of the mass spectrometry, we performed immunoprecipitation of 3×Myc-Card19, employing a combination of a mouse anti-myc antibody and Protein G-Sepharose beads. We then analyzed the results via western blots (Fig. 14B). We were easily able to validate the specific immunoprecipitation of both Sam50 and Mic19, which were readily apparent in anti-Myc immunoprecipitations from

the cell line expressing 3×Myc-Card19 compared to the control cell line which did not express 3×Myc-Card19. However, we had difficulty confirming association with Mic60, Mtx2, and Mic25 by immunoprecipitation. Because Sam50 and Mic19 were reliable interaction markers of Card19 with MICOS in this context, we employed immunoprecipitation and western blots to examine the ability of the G73R and Δ146 mutants to interact with these proteins. We confirmed, first, that Card19-G73R and -Δ146 were expressed and immunoprecipitated with efficiency equivalent to wild type (WT) 3×Myc-Card19 (Fig. 14B). G73R immunoprecipitate included less Sam50 and Mic19 as compared to wild-type Card19, demonstrating impaired association with these proteins (Fig. 14B). The Δ146 mutant did not detectably co-immunoprecipitate with either Mic19 or Sam50 (Fig. 14B).

Finally, to determine if we could image the interaction between Card19 and MICOS components, we co-expressed 3×Myc-Card19 and Mic19-3×OLLAS in *Card19* -/- immortalized macrophages. We then stained the cells for anti-OLLAS, anti-myc, and anti-Tom20. To reduce the possibility of cross-reactivity between the anti-OLLAS and anti-Myc antibodies, we directly labelled anti-OLLAS with AlexaFluor 488 and anti-Myc with AlexaFluor 647. We then imaged the macrophages via SIM (Fig. 14C). We found that while endogenous Tom20 had a continuous, non-punctate distribution around the entire mitochondria, both 3×Myc-Card19 and Mic19-3×OLLAS exhibited the clustering distribution that we saw in our previous SIM data (Fig.8B, Fig.11A/B, Fig. 12B). The punctate distribution of 3×Myc-Card19 and Mic19-3×OLLAS appeared to overlap, as indicated by the magenta arrow in Fig. 14C. These data together indicate that Card19

interacts with MICOS and MICOS-interacting proteins in a manner dependent on CARD conformation and expression of the distal C-terminus.

Card19 -/- bone marrow derived macrophages and fibroblasts exhibit distorted cristae morphology

Phenotypes of MICOS defects have been widely reported in various human cell lines, although none have been examined in mouse BMDMs or human primary macrophages. Both Mic19, Mic25, and Mic60 deficiencies have been reported to result in aberrant cristae and decreased number and width of cristae junctions (5; 36; 80). Therefore, we examined the morphology of the mitochondria and mitochondrial cristae in both *Card19* +/+ and *Card19* -/- BMDMs using TEM. In general, mitochondria in BMDMs of either genotype were relatively heterogenous, thus making clear assessment of the mitochondrial and cristae morphology challenging. However, close examination revealed that *Card19* -/- BMDMs contained mitochondria with an increased presence of vesicular cristae (Fig. 15A). This phenotype has been reported in HeLa cells that contain knockdowns of Mic60 or Mic19 (158). Furthermore, we found that the number of mitochondria in both *Card19* +/+ and *Card19* -/- BMDMs increased in response to 3 hours of stimulation with 100 ng/ml LPS, which is known to induce oxidative stress (Fig. 15B). While both genotypes displayed an increase in the mitochondria with vesicular cristae phenotype in response to LPS, *Card19* -/- BMDMs exhibited proportionally more mitochondria with vesicular cristae then their wild-type counterparts (Fig. 15B). Because the mitochondria and cristae within primary cells, especially BMDMs, tend to be relatively heterogenous relative to that of cell lines, we suspected that we may find a cristae phenotype more apparent when examining the cristae within a cell line. Therefore, we performed TEM on 70 - 80 μm serial sections of immortalized fibroblasts

derived from lungs harvested from *Card19* +/+ and *Card19* -/- mice. Since cell lines tend to rely on aerobic glycolysis rather than oxidative phosphorylation for ATP generation, we cultured the fibroblasts in galactose-supplemented glucose-free DMEM for 5 days prior to fixation. Galactose is ultimately broken down via glycolysis but results in zero net ATP produced. The cells are therefore forced to rely on OXPHOS for ATP generation. The cristae within the *Card19* +/+ fibroblast mitochondria were more homogenous than we previously observed in the BMDMs. Specifically, there were clearly apparent lamellar cristae in the mitochondria of *Card19* +/+ fibroblasts (Fig.16A). However, there was little organization of the cristae within the mitochondria of *Card19* -/- fibroblasts. Indeed, most of the cristae appear vesicular, and there are no apparent lamellar cristae (Fig. 16A). The gross mitochondrial morphology was inconsistent in both size and shape in *Card19* -/- fibroblasts, whereas the mitochondria in *Card19* +/+ fibroblasts were consistent in size and shape (Fig. 16A). Upon closer examination of individual mitochondria, we confirmed the lamellar cristae from the wild-type mitochondria (Fig. 16B). However, in the knock-out mitochondria, we identified arc-like cristae (Fig. 16C), vesicular cristae (Fig. 16D), and generally disorganized, unclassified cristae (Fig. 16E). We did not identify any mitochondria with lamellar cristae in the *Card19* -/- fibroblasts. These data strongly suggest that cristae are morphologically dysregulated in the absence of Card19. Together, these results indicate that Card19, like other MICOS proteins, promotes normal cristae morphology, and in the absence of Card19, the mitochondria are distorted in comparison to the wild-type counterparts.

Card19 -/- bone marrow derived macrophages display hallmarks of mitochondrial dysfunction

Mitochondria with MICOS defects have been reported to display signs of dysfunction, including decreased OCR, increased mROS expression, and alteration in MMP (5; 36; 49; 133; 158; 168). We therefore examined whether BMDMs showed similar signs of mitochondrial dysfunction. To measure the metabolic state of the BMDMs, we employed Seahorse Extracellular Flux technology. In brief, *Card19* +/+ and *Card19* -/- BMDMs were cultured in glucose-supplemented DMEM, seeded in special 96 well plates designed to be used with the Seahorse Extracellular Flux Analyzer XFe96, and allowed the cells to adhere overnight. The following morning, the oxygen consumption rate (OCR), which is a measure of OXPHOS, and the extracellular acidification rate (ECAR), which is a measure of glycolysis, were measured. The basal OCR and ECAR were measured, along with the OCR and ECAR after the addition of Oligomycin A, FCCP, and Rotenone/Antimycin A (Fig. 17A and B, respectively). Oligomycin A is an ATP Synthase inhibitor and thus decreases OCR upon addition since oxidative phosphorylation is inhibited. Addition of Oligomycin A permits the measurement of proton leak independent of ATP Synthase. FCCP is an uncoupler, meaning that it decouples the proton gradient from oxygen consumption -driven ATP generation. Addition of FCCP forces the cell to its maximal oxygen consumption since the proton gradient cannot drive ATP production. Finally, Rotenone and Antimycin A are inhibitors of Complex I and Complex III of the ETC, respectively. The addition of these reagents inhibits OXPHOS completely, thus abolishing oxygen consumption driven by the ETC. This permits the measurement of non-OXPHOS driven oxygen consumption. We found that *Card19* -/- BMDMs displayed a modest decrease in OCR (Fig. 17A/C). Additionally, *Card19* -/- BMDMs exhibited decreased maximal

respiratory rate (Fig. 17A/D), which is the maximum respiration rate a cell can achieve, spare oxygen capacity (Fig. 17A/E), which measures the cell's ability to respond to changes in energy demand, and ATP production (Fig. 17A/F), which measures the amount of oxygen being consumed to generate ATP. Overall, the ECAR was also lower in *Card19 -/-* BMDMs, suggesting that the cells were less glycolytic. Together, these data indicate that *Card19 -/-* BMDMs have a decreased OXPHOS rate compared to the wild-type BMDMs, although it is unclear if this is due to mitochondrial dysfunction or simply because the *Card19-/-* BMDMs were relatively less metabolically active.

To measure the MMP and the levels of mROS in *Card19 +/+* and *Card19 -/-* BMDMs, we utilized flow cytometry. BMDMs were seeded in 6-well plates and allowed to adhere overnight. The next morning, BMDMs were untreated, or stimulated with LPS, or Antimycin A (a positive control for mROS generation). To measure MMP, cells were co-stained with MitoTracker Green and TMRE. MitoTracker Green is a membrane-permeable, mitochondrial-specific fluorescent dye; its fluorescence is reported to be resistant to changes in MMP, and therefore it can be used as a measure of mitochondrial mass. To measure mROS, cells were stained with MitoSox Red. All cells were also stained with a Zombie fixable viability dye (BioLegend) to allow discrimination of viable and dead cells (data not shown). We did not find a significant difference in cell death or mitochondrial mass between the two genotypes via flow cytometry (data not shown). *Card19 -/-* BMDMs showed an increased population of mitochondria with a decreased MMP at basal levels (Fig. 18A), although this difference was ablated after 6 hours of treatment with 500 ng/ml LPS (Fig. 18A). *Card19 -/-* BMDMs exhibited increased basal levels of mROS relative to *Card19 +/+* BMDMs (Fig. 18B). *Card19 +/+* and *Card19 -/-*

BMDMs produce equivalent amounts of mROS in response to both Antimycin A and LPS treatment (Fig. 18B).

Because Card19 deficient BMDMs had increased levels of basal mROS, we suspected these BMDMs may produce more mROS at lower concentrations of LPS stimulation, whereas wild-type BMDMs would be resistant to producing mROS at lower concentrations of LPS stimulation. Therefore, we treated wild-type and knock-out BMDMs with 100 ng/ml LPS for 3 hours and 6 hours, respectively (Fig. 18C). In our previous mROS studies, we stimulated the BMDMs with 500 ng/ml of LPS for 6 hours because this has been reported previously to stimulate levels of mROS detectable by MitoSox Red in wild-type BMDMs (192). Interestingly, we discovered that *Card19 -/-* BMDMs produced a robust shift in MitoSox Red signal at both time points with 100 ng/ml LPS, whereas the *Card19 +/+* BMDMs did not produce a shift in MitoSox Red signal with either timepoint (Fig. 18C). This demonstrates that in the absence of Card19, mitochondria are more sensitive to generating mROS in response to LPS at levels that do not generate measurable mROS in the presence of Card19. Together, these data strongly indicate that mitochondria in *Card19 -/-* BMDMs show signs of mitochondrial dysfunction or dysregulation.

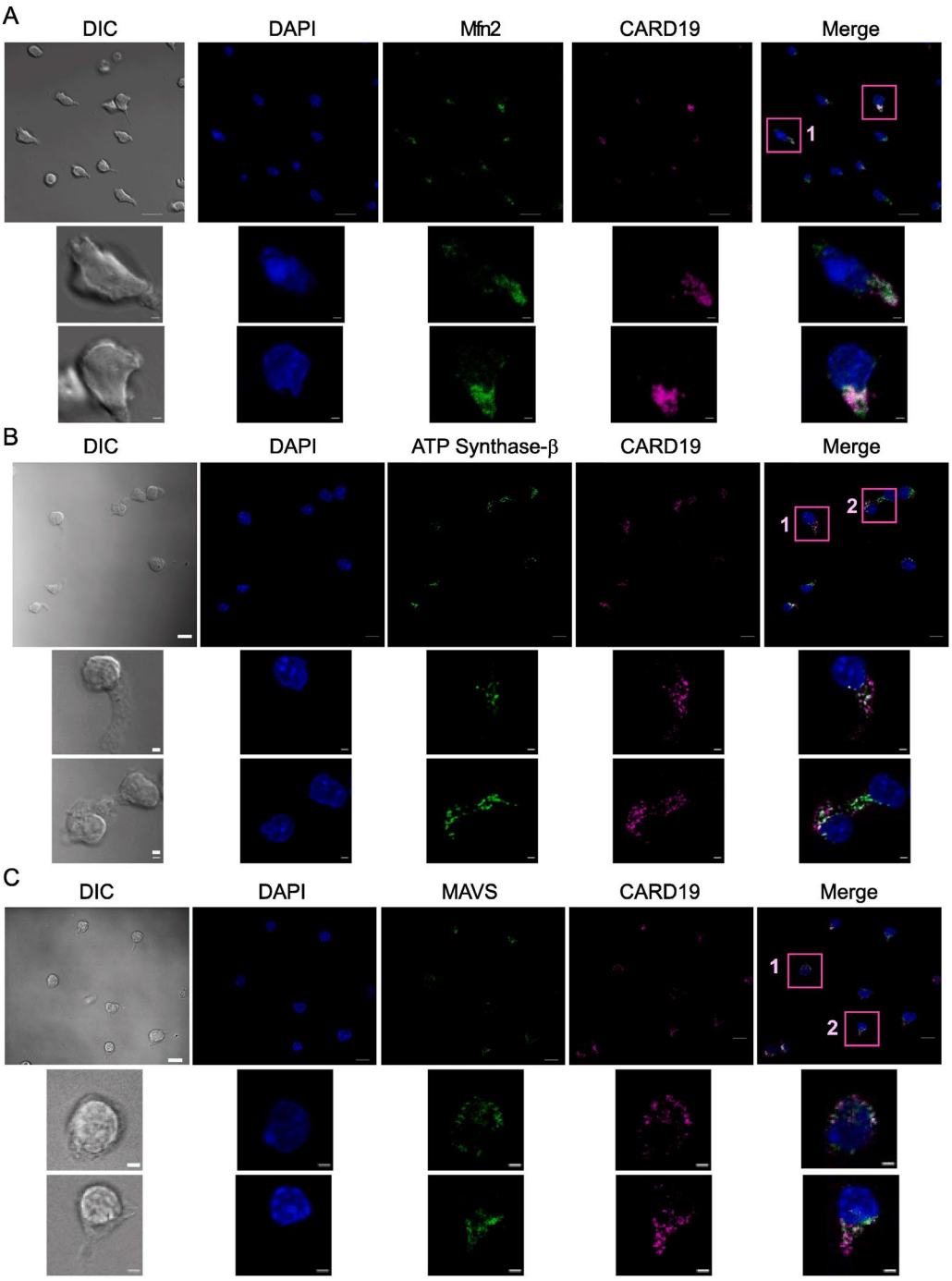

Fig. 5. Endogenous Card19 colocalizes with mitochondrial markers in murine CD8+ T cells.

(A) *Card19* +/+ CD8+ T cells were stained for endogenous Mfn2 and Card19 and imaged via confocal microscopy with a 63x oil objective. (B and C) are the same as in (A) but were stained with ATP Synthase β (B) or Mavs (C). Scale bars in full sized images correspond to 10 μm and 2 μm in insets. Reproduced with permission from (138).

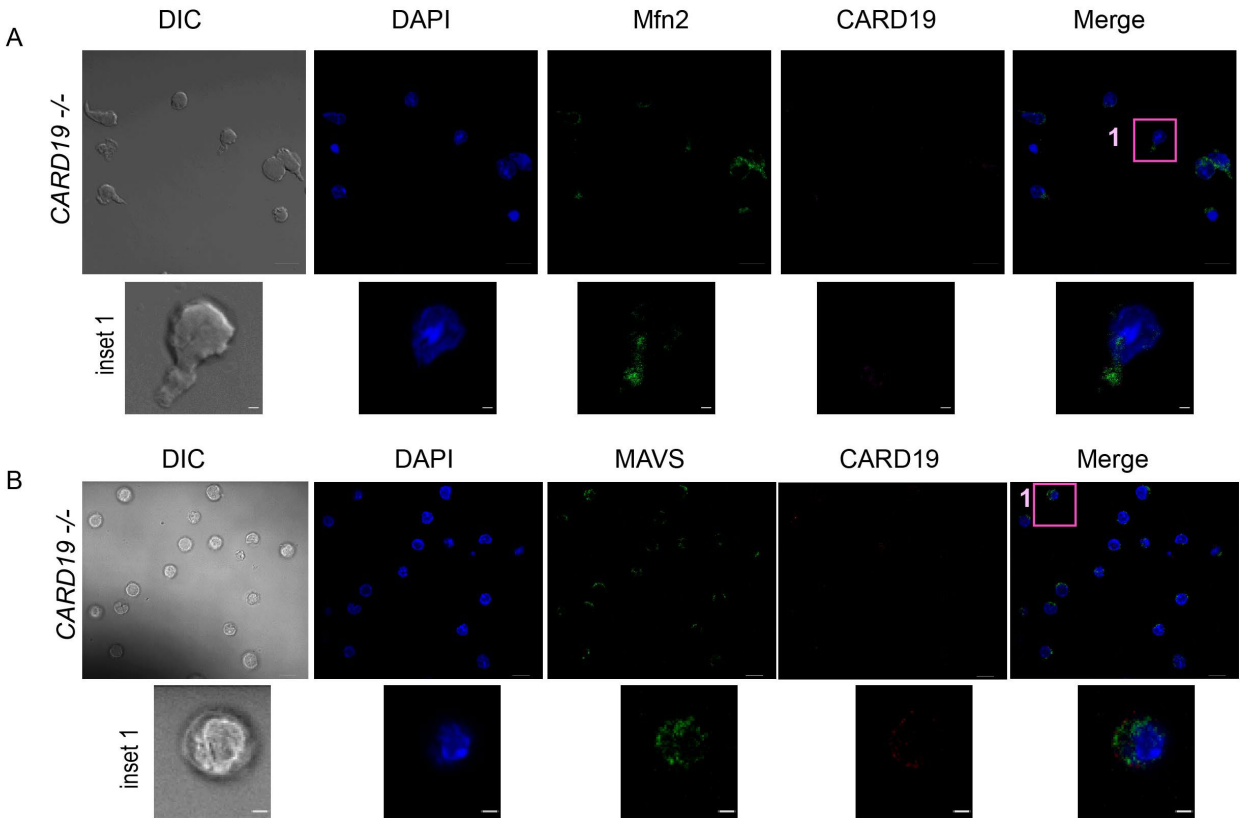

Fig. 6. There is little apparent detectable signal of Card19 in *Card19 -/-* CD8+ T cells when measured by confocal microscopy.
(A) *Card19 -/-* CD8+ T cells were stained with Mfn2 and Card19 and imaged by confocal microscopy with a 63x oil objective. (B) Same as in (A), but cells were stained with Mavs and Card19. Scale bars in full images correspond to 10 µm and 2 µm in insets. Reproduced with permission from (138).

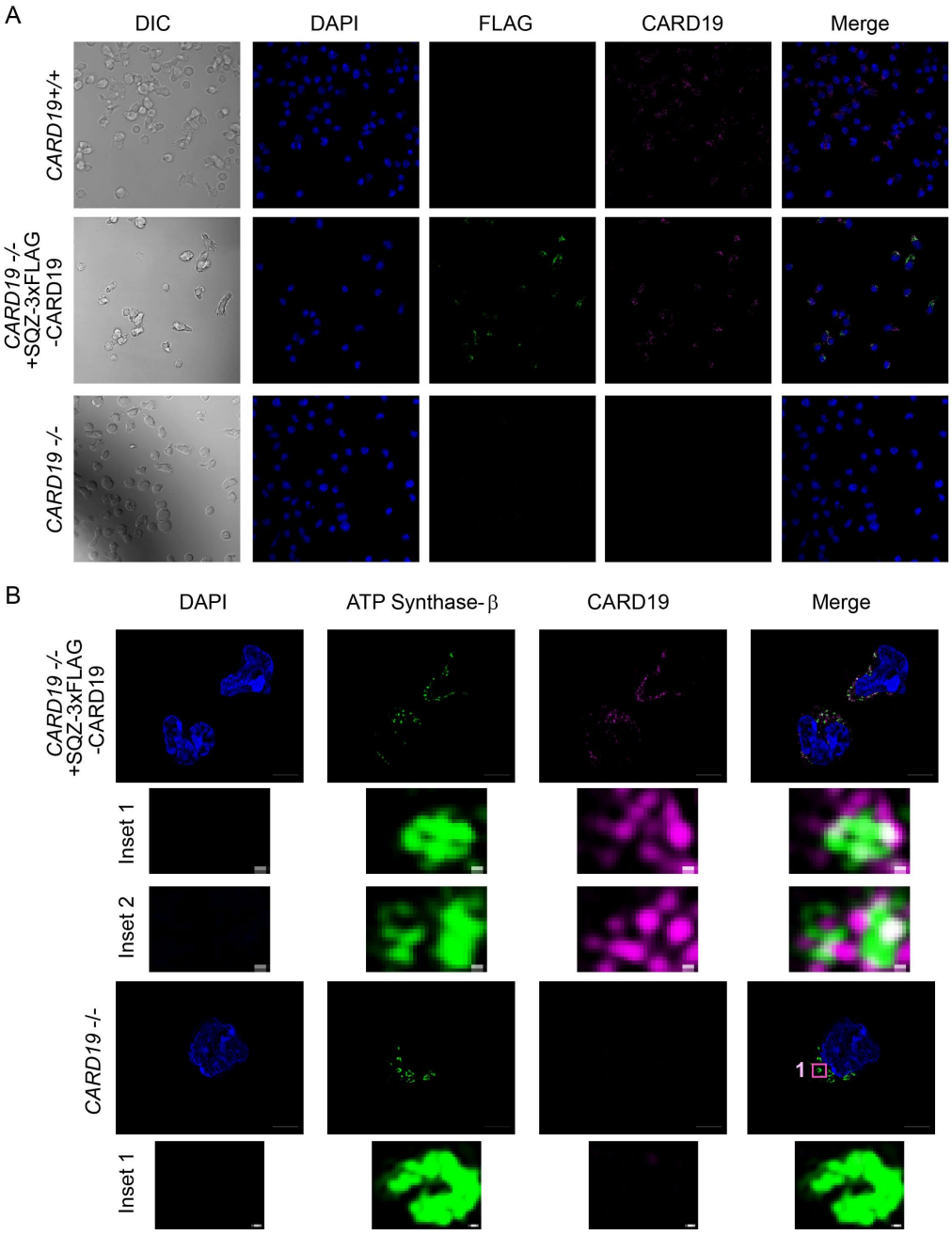

Fig. 7. *Card19* -/- CD8 + T cells expressing 3×FLAG-Card19 exhibit clusters of Card19 that distribute with ATP Synthase β in individual mitochondria when imaged via SIM.
(A) *Card19* +/+ and *Card19* -/- CD8+ T cells as well as *Card19* -/- CD8+ T cells reconstituted with 3×FLAG-Card19 were stained for FLAG and Card19 and imaged via confocal microscopy with a 63x oil objective. (B) SIM imaging of *Card19* -/- CD8+ T cells unreconsituted or reconstituted with 3×FLAG-Card19. Scale bars in full size images correspond to 5 μM and 0.2 μM in insets. Reproduced with permission from (138).

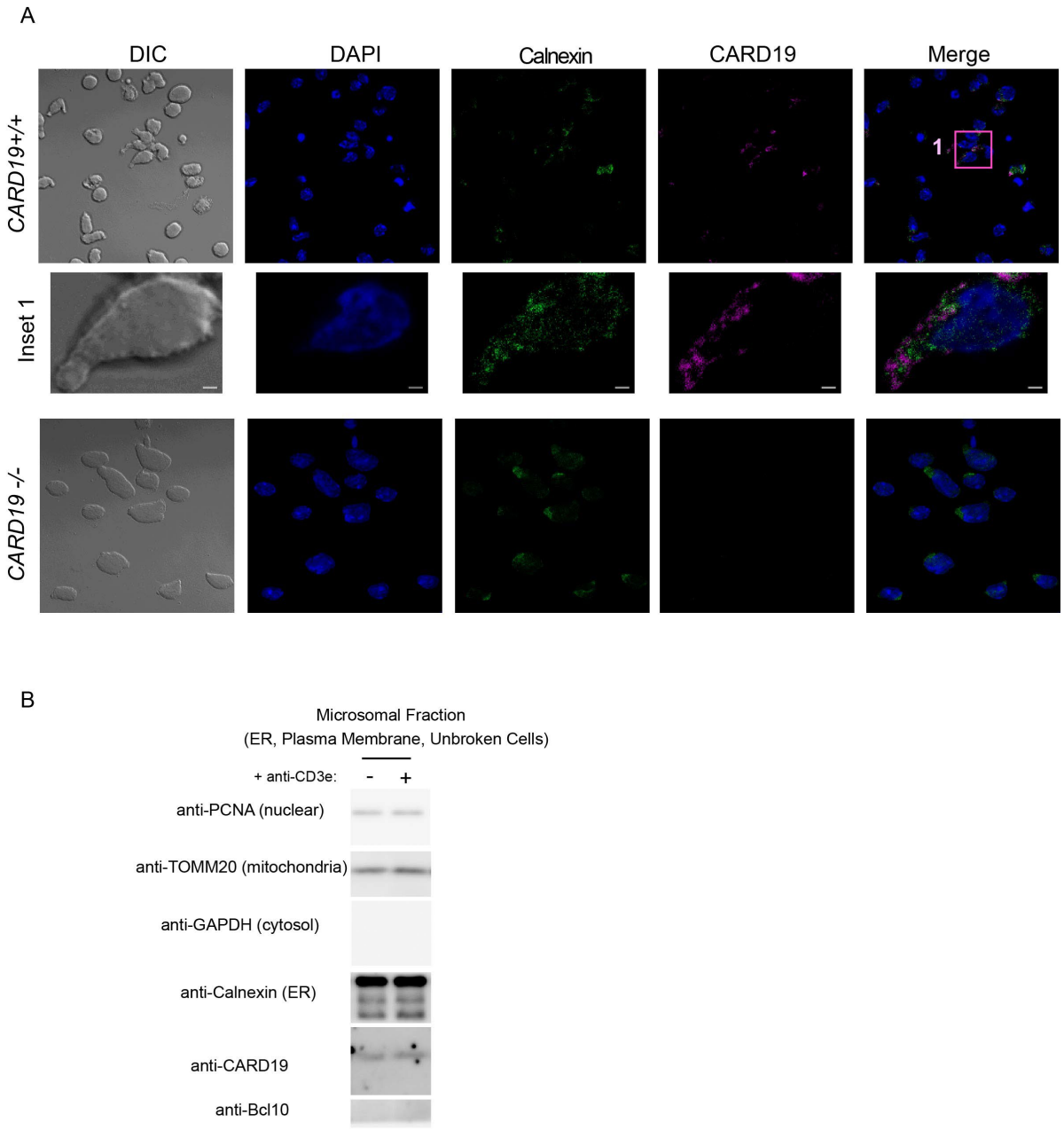

Fig. 8. Endogenous Card19 does not distribute with Calnexin, a marker of the endoplasmic reticulum.
(A) Confocal microscopy of *Card19* +/+ and *Card19* -/- CD8+ T cell blasts stained for Calnexin and Card19. Scale bar in insets corresponds to 2 μm. (B) Microsomal subcellular fraction isolated from *Card19* +/+ CD8+ T cell blasts treated with anti-CD43 (-) or anti-CD3 (+) for 20 minutes. Reproduced with permission from (138).

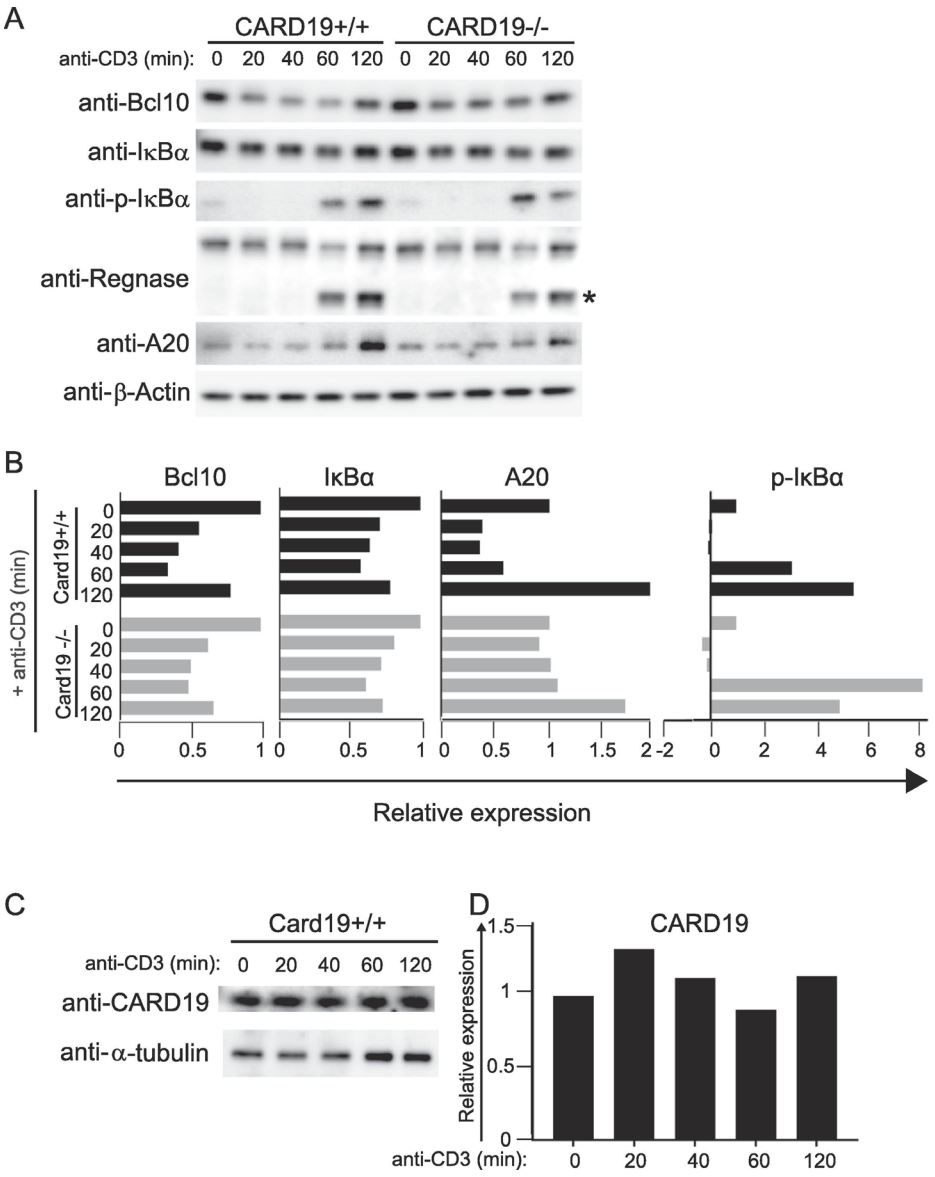

Fig. 9. Absence of Card19 does not result in a change or increased intensity in Bcl10 or NF-κB activation dynamics in primary murine CD8+ T cells.
(A) Markers of NF-κB activation were measured by western blot in whole cell lysates of *Card19* +/+ and *Card19* -/- CD8+ T cells after anti-CD3 restimulation for the indicated amounts of time. * indicates the Malt1-cleaved form of Regnase. (B) Band intensities of Bcl10, IκBα, A20, and p- IκBα were quantified, normalized to β-actin, and expressed as intensities relative to the untreated sample in each group. (C) whole cell lysates of *Card19* +/+ CD8+ T cells restimulated with anti-CD3 for the indicated times. (D) Band intensities of Card19 in (C) were normalized to α-tubulin and expressed intensities relative to the untreated timepoint. Results are representative of 3 experiments, performed with CD8+ T cells isolated from 1 mouse per genotype per experiment. Reproduced with permission from (138).

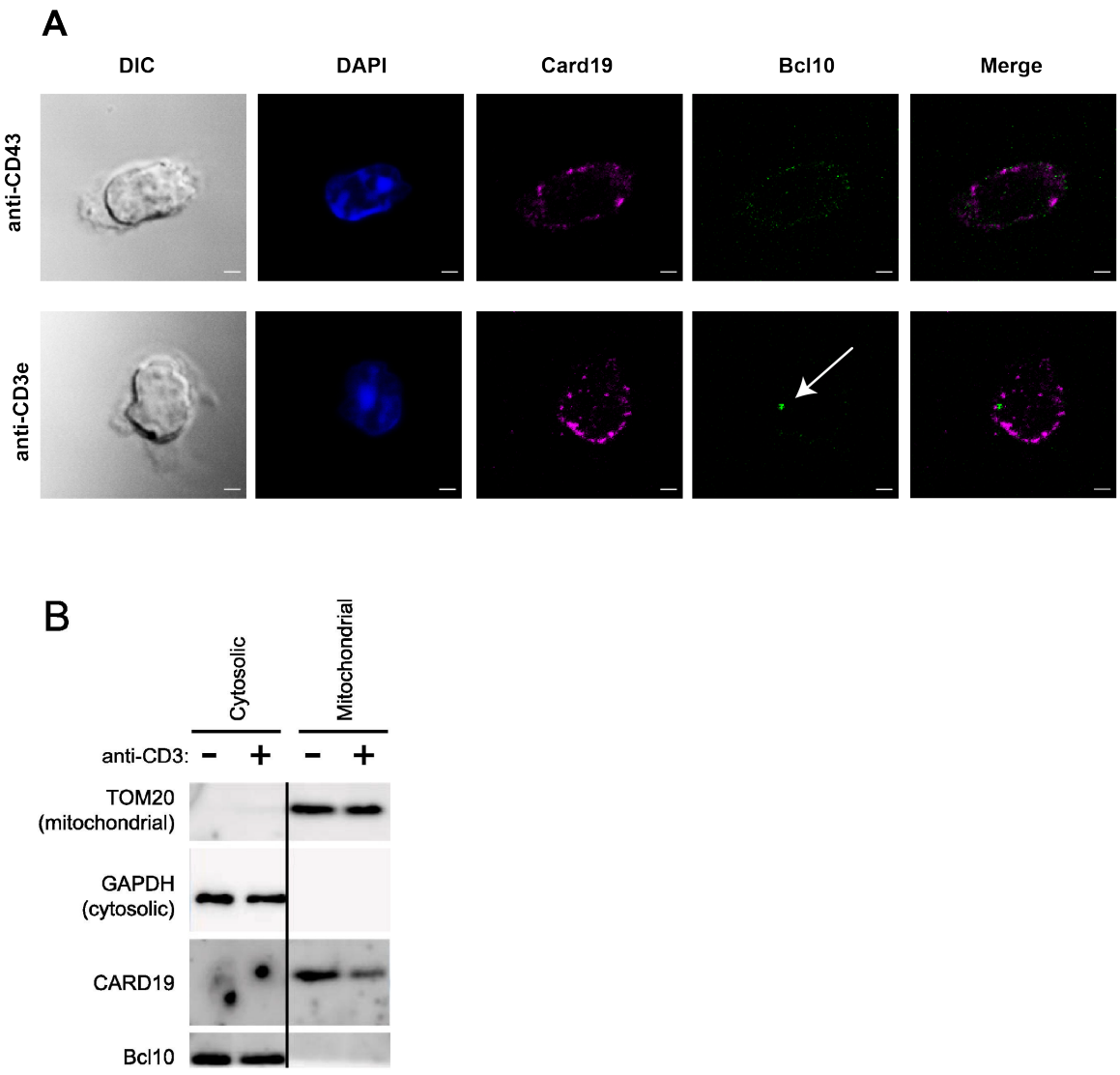

Fig. 10. Endogenous Card19 does not interact with endogenous Bcl10 e*x vivo*.

(A) *Card19* -/- CD8+ T cell blasts were seeded on coverslips coated with anti-CD43 or anti-CD3 for 20 minutes and imaged via confocal microscopy with a 63X oil objective. Bcl10 punctae are indicated by white arrows. Scale bars correspond to 2 μM. (B) Cytosolic and Mitochondrial subcellular fractionation were collected from *Card19* +/+ CD8+ T cell blasts treated with anti-CD43 (-) or anti-CD3 (+). Reproduced with permission from (138).

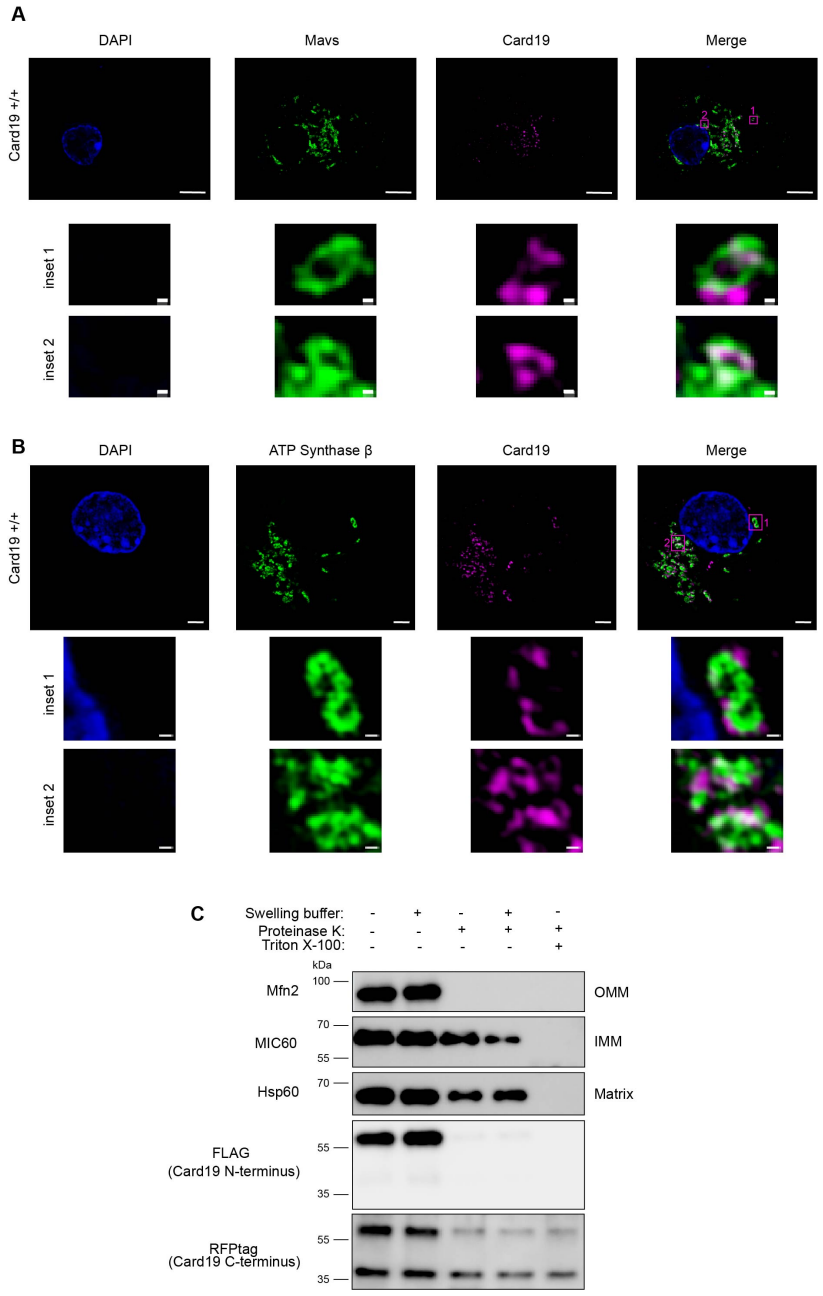

Fig. 11. Endogenous Card19 clusters along the mitochondria in *Card19* +/+ BMDMs when measured by SIM and localizes to the OMM.
(A) SIM imaging of *Card19* +/+ BMDMs stained for endogenous Card19 and OMM marker Mavs. Insets show co-stains in individual mitochondria. (B) shows the same as in (A), but BMDMs were stained for IMM marker ATP Synthase β rather than Mavs. Insets for (A) were generated by maximum intensity projection of z-slices 18 -22 (inset 1) and 17 -19 (inset 2). Scale bars in full sized images corresponded to 5 μm and 0.2 μm in insets. (C) Proteinase K protection assay of mitochondria isolated from *Card19* -/- immortalized fibroblasts reconstituted with 3×FLAG-Card19-RFPt.

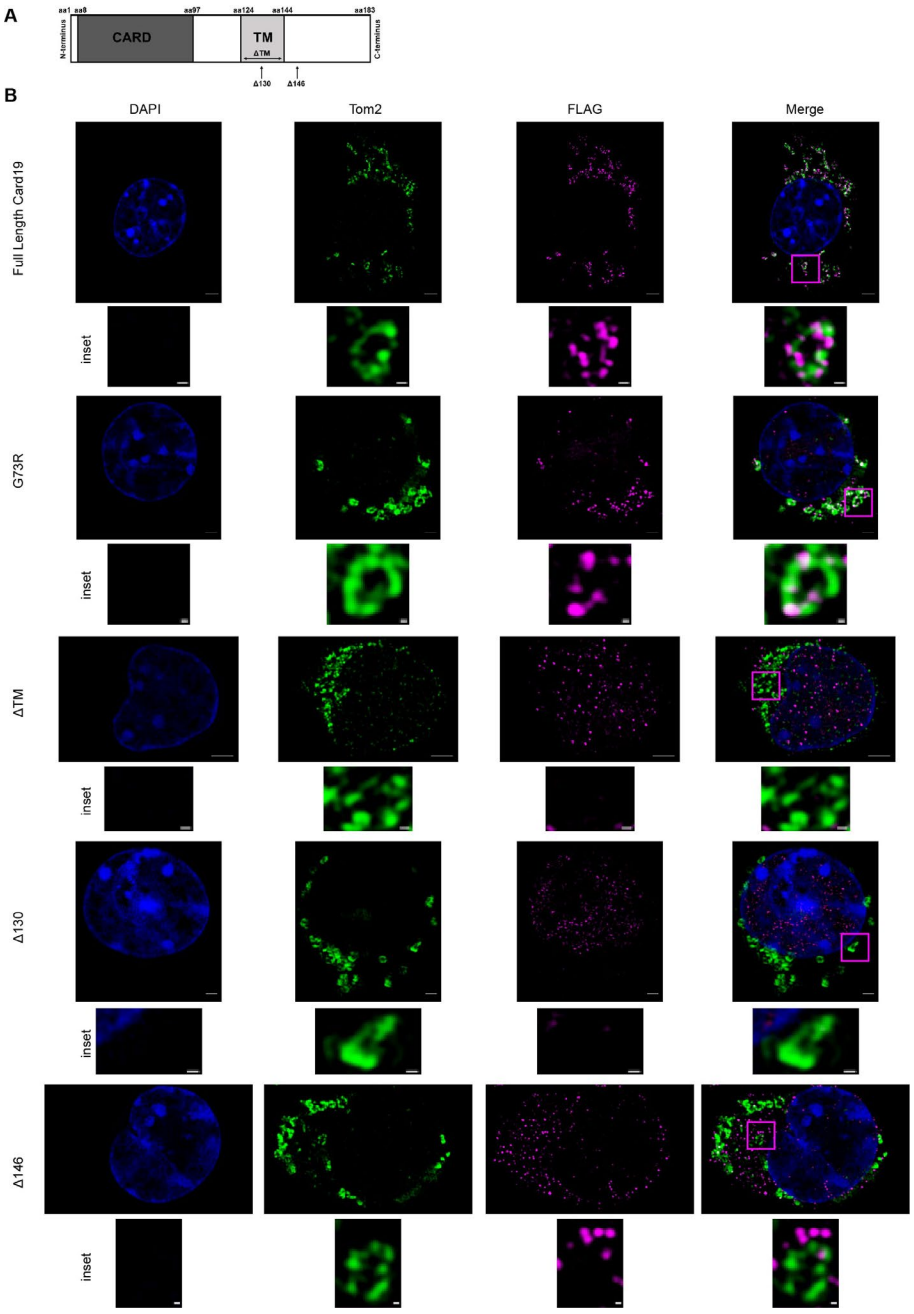

Fig. 12. 3×FLAG-Card19-full length and G73R cluster in individual mitochondria when expressed in a *Card19 -/-* cell line, but other mutant derivatives mislocalize. (A) Graphical representation of the G73R point mutation and progressive Card19 deletions ΔTM, Δ130, and Δ146. The CARD and predicted transmembrane domain (TM) are indicated. (B) SIM imaging of Card19 -/- immortalized macrophages reconstituted with 3xMyc-Card19-full length and its mutant derivatives. Insets show individual mitochondria. Scale bars correspond to 5 μm in full images and 0.2 μm in insets.

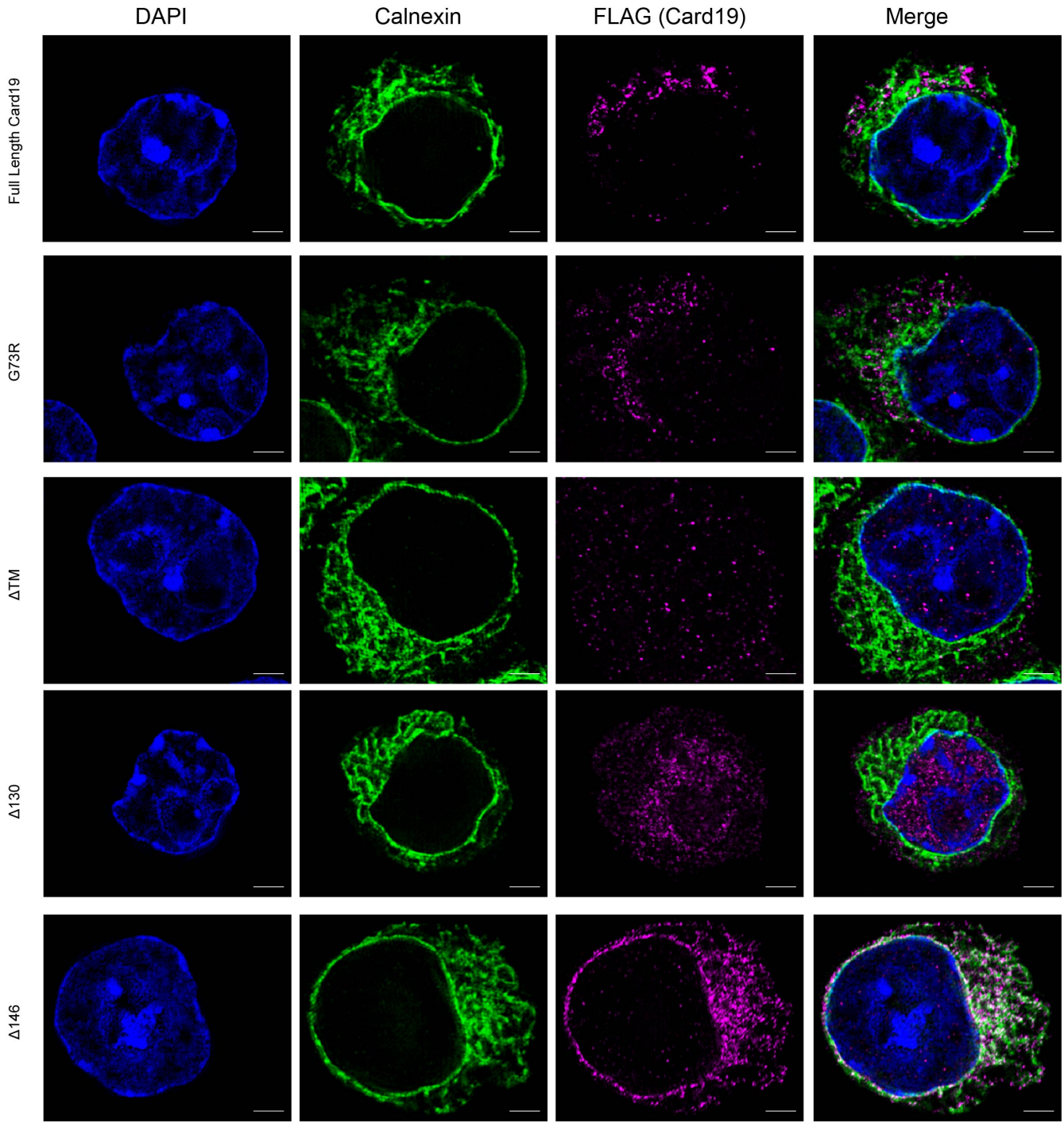

Fig. 13. 3xMyc-Card19-Δ146 localizes to the endoplasmic reticulum.
Card19 -/- immortalized macrophages reconstituted with 3xMyc-Card19-Full length and its mutant derivatives were imaged via SIM at 63X oil objective. Scale bars correspond to 5 μm.

A

	Protein	Normalized Peptides (myc)	Normalized Peptides (control)	Ratio (myc/control)	Z Score	p-value
MICOS	Sam50	25.89421731	1	25.89421731	3.562162768	0.000367812
	Mic19	22.916423	1	22.916423	3.424657628	0.000615575
	Mic25	22.916423	1	22.916423	3.424657628	0.000615575
	Mtx2	15.93490295	1	15.93491295	3.015694756	0.002563912
	Mic60	170.3042753	11	15.57402503	2.989910378	0.002790593

B

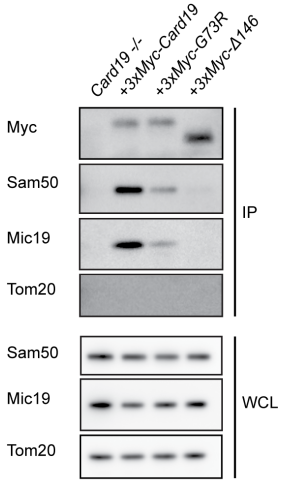

C

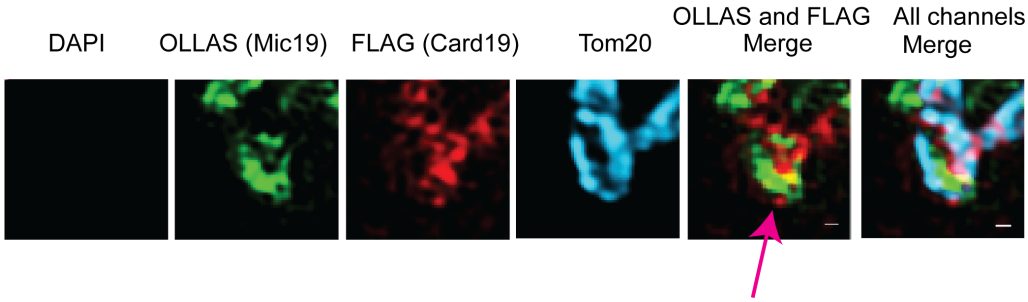

Fig. 14. 3xMyc-Card19 interacts with components of MICOS.
(A) Mass Spectrometry analysis of immunoprecipitation against 3xMyc-Card19 show that Card19 pulls down with components of MICOS. (B) Western blot analysis confirmed the interaction between 3xMyc-Card19 with Sam50 and Mic19. IP indicates immunoprecipitation samples; WCL indicates whole cell lysates of the samples used for the immunoprecipitation studies. (C) SIM imaging of *Card19 -/-* immortalized macrophages co-expressing Mic19-3xOLLAS and 3xMyc-Card19. Samples were stained with mouse anti-OLLAS, mouse anti-FLAG, and rabbit anti-Tom20. Scale bars correspond to 0.2 μm.

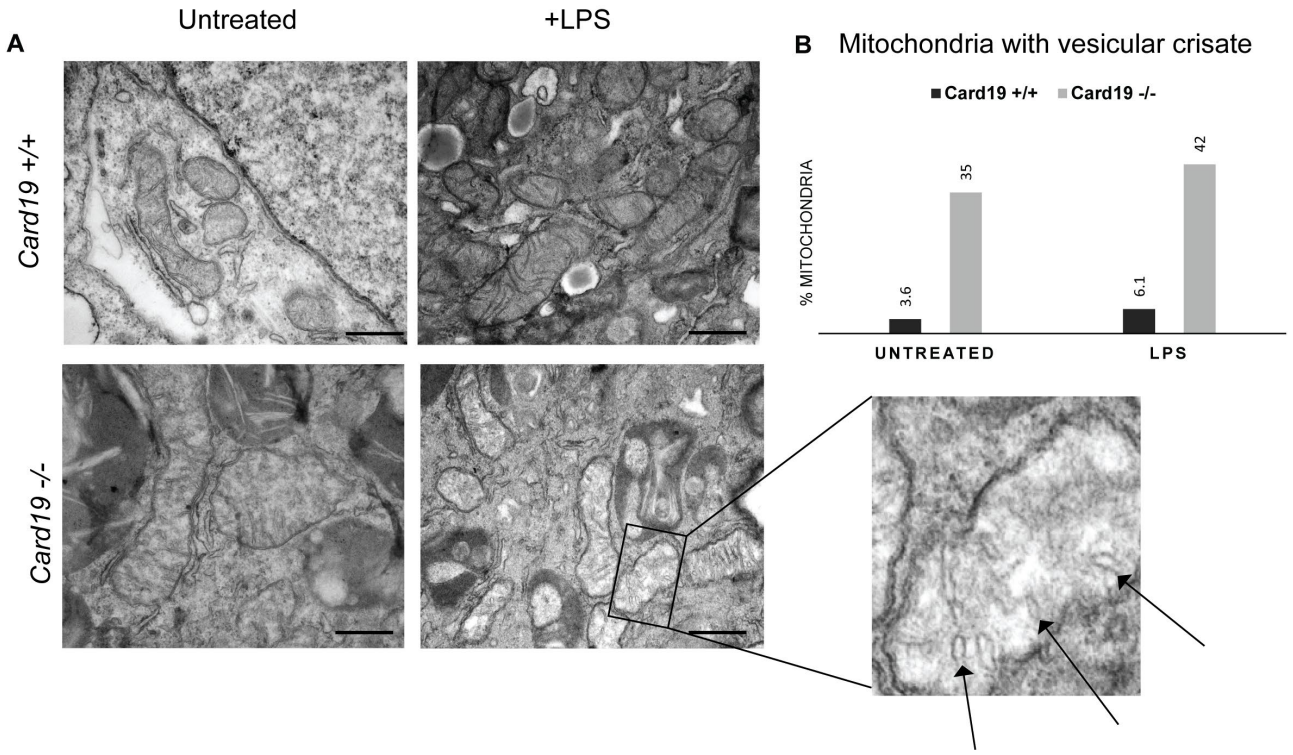

Fig. 15. Vesicular cristae are apparent in the mitochondria of *Card19 -/-* BMDMs
(A) BMDMs were untreated or treated with LPS (100 ng/ml, 3 hours) and imaged with TEM. Vesicular cristae are indicated by arrows in the inset. (B) The number of mitochondria containing vesicular cristae shown in (A) were quantified.

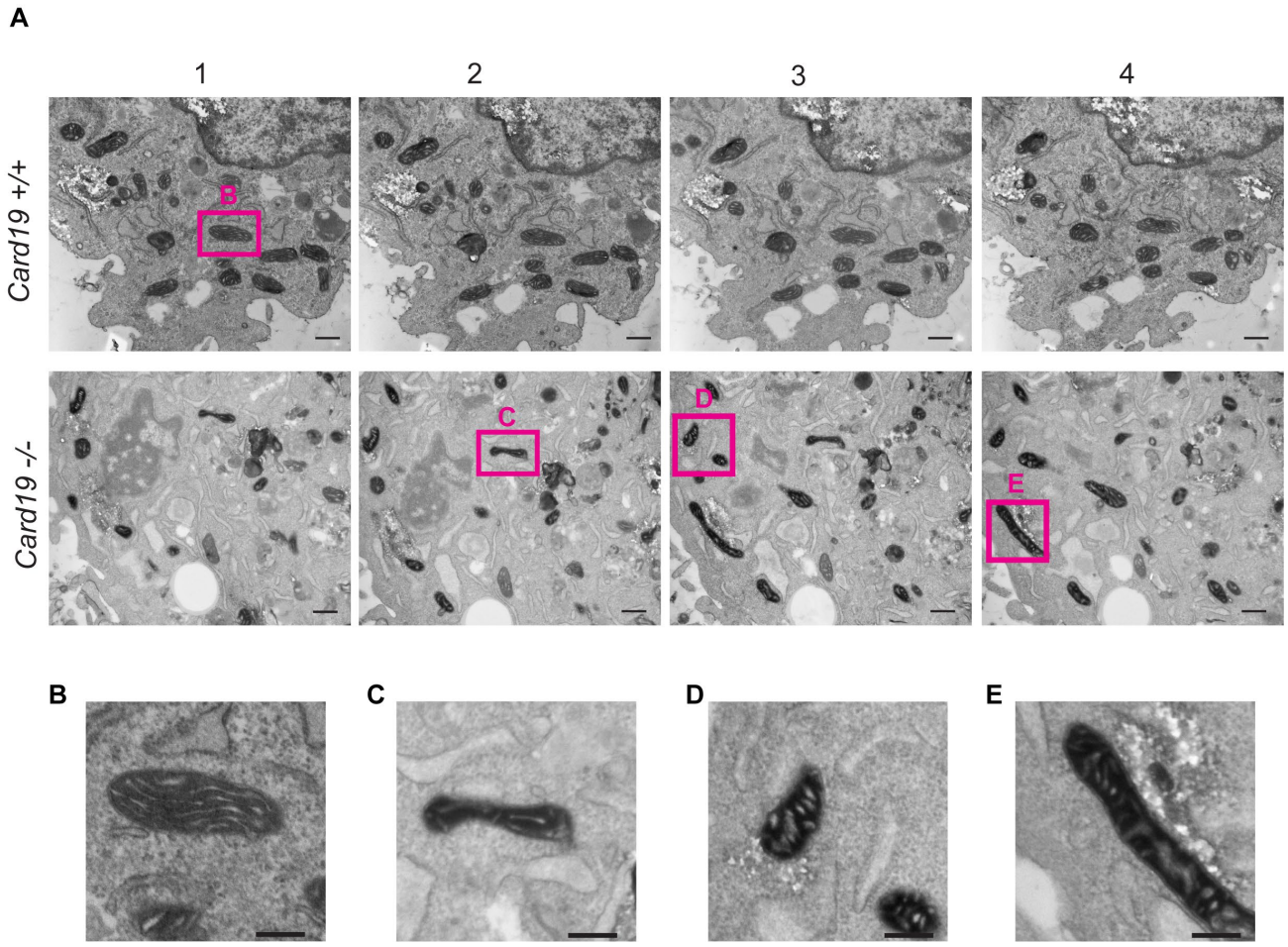

Fig. 16. Aberrant cristae are apparent in the mitochondria of *Card19 -/-* fibroblasts derived from murine lungs and cultured in glucose-free, galactose-supplemented media.
(A) Immortalized murine lung fibroblasts were grown in glucose-free, galactose-supplemented media for 5 days before cells were fixed and prepared for TEM. Serial sections 70 to 80 µm are shown in sections 1 – 4. Insets of mitochondria are indicated by the magenta boxes and correspond to healthy lamellar cristae from wild-type mitochondria (B) or aberrant cristae from knock-out mitochondria including arc cristae (C), vesicular cristae (D), and generally disorganized cristae (E). Scale bars in (A) correspond to 500 nm. Scale bars in (B – E) correspond to 250 nm.

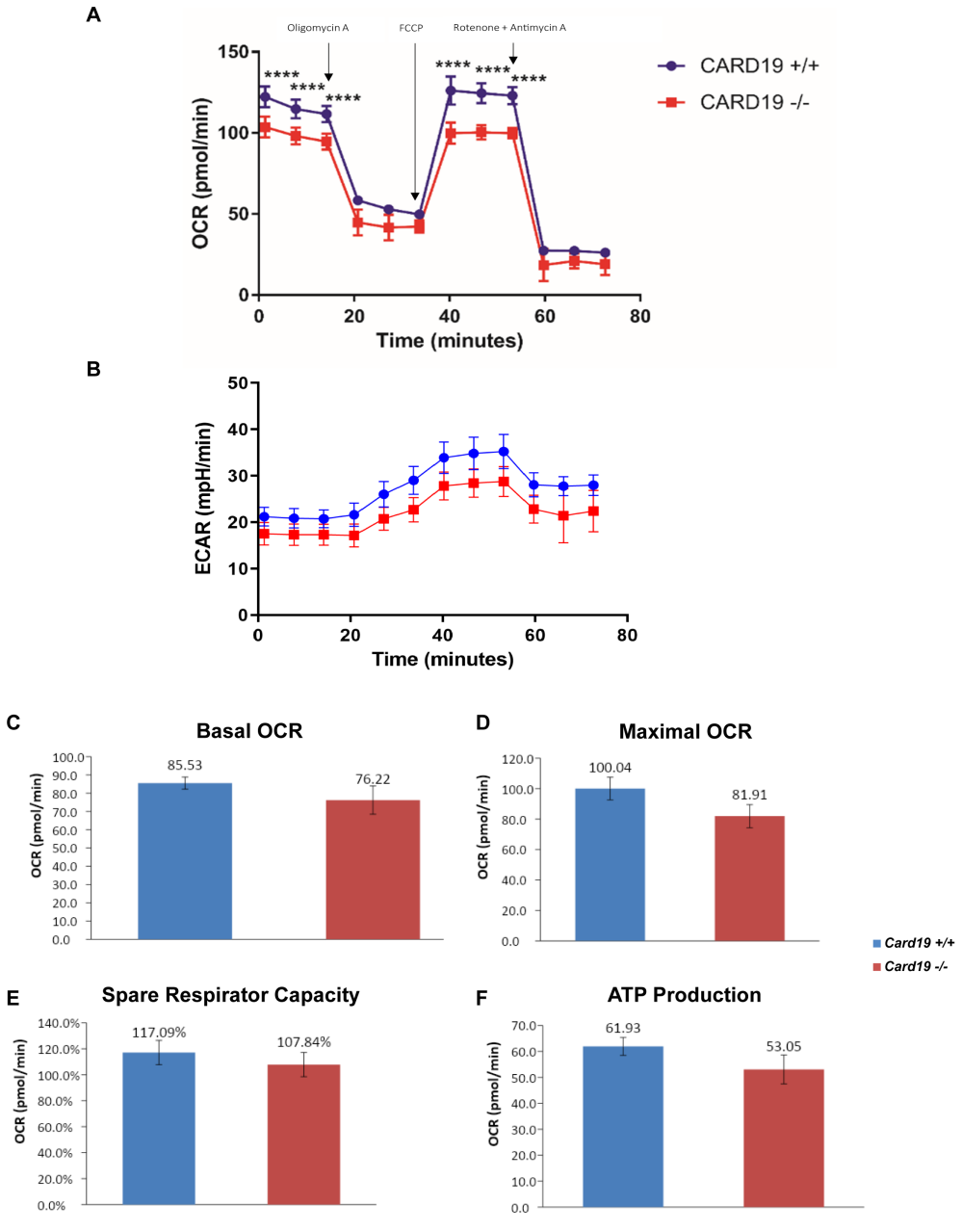

Fig. 17 *Card19 -/-* BMDMs exhibit a modestly lower basal OCR and ECAR relative to *Card19* +/+ BMDMs.
Seahorse extracellular flux analysis was performed on BMDMs with the addition of Oligomycin A, FCCP, and Rotenone/Antimycin A. The OCR (A) and ECAR (B) measured before and after the addition of the respective drugs are shown. Calculations of mitochondria health, including basal OCR (C), maximal OCR (D), spare respiratory capacity (E), and ATP production (F) are also shown.

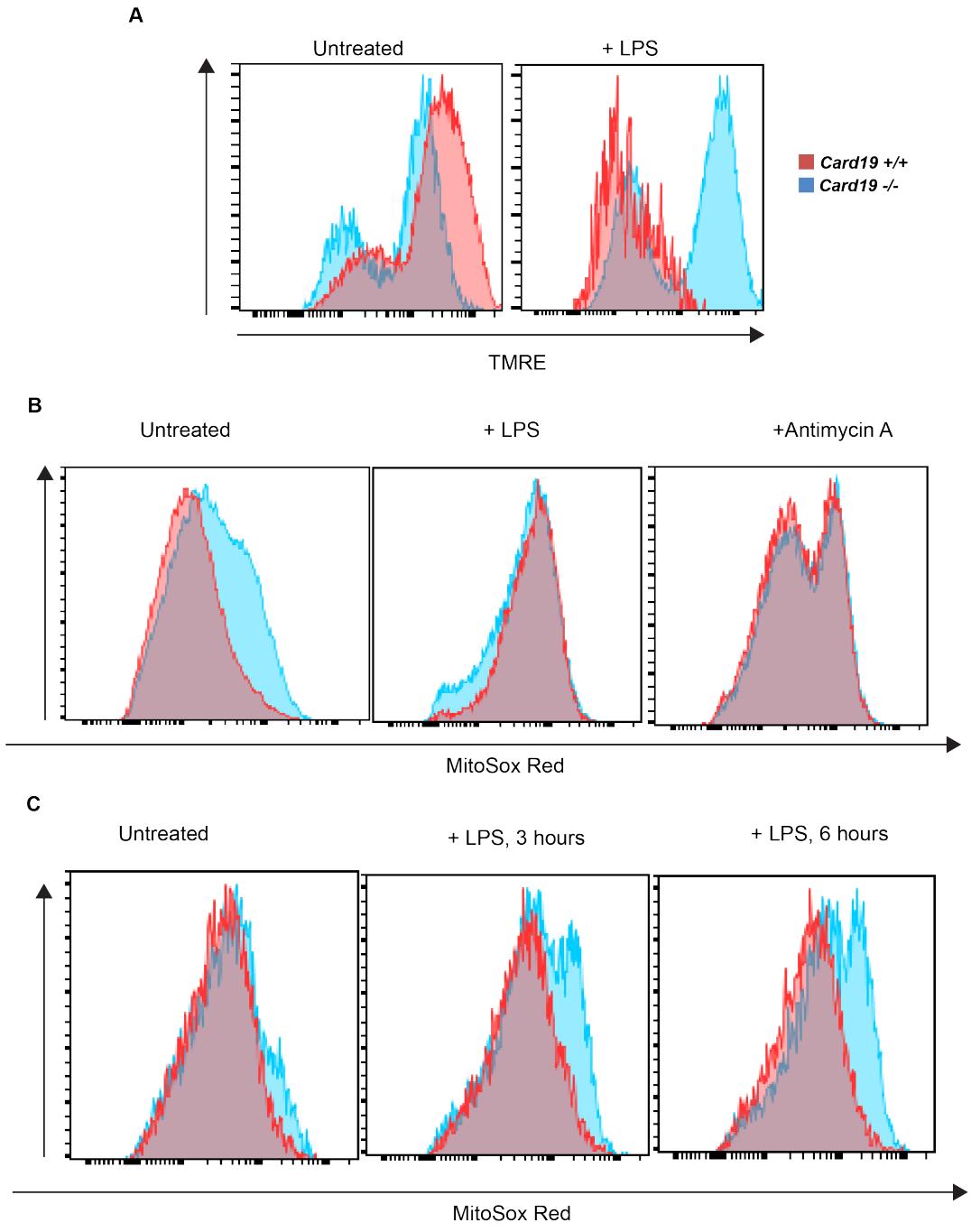

Fig. 18 *Card19 -/-* BMDMs display an increased population with decreased MMP as well as increased mROS.
(A) TMRE staining, measuring MMP, was decreased in *Card19 -/-* BMDMs. (B) BMDMS were untreated, treated with LPS (500 ng/ml, 6 hours), or Antimycin A (5 µM, 6 hours). (C) To assess if *Card19 -/-*BMDMs were sensitive to mROS production at lower LPS levels, BMDMs were untreated or treated with 100 ng/ml LPS for 3 or 6 hours. In both (B) and (C), mROS was measured with MitoSox Red. All samples were gated for live cells using Zombie UV fixable viability dye.

Chapter 4: Discussion

As mitochondria have emerged as clear regulators of multiple cellular functions, and as it is becoming increasingly clear that mitochondrial dysfunction is linked to a range of neurodegenerative and immune dysregulation diseases, particularly with uncontrolled inflammation, it is vital to investigate how these processes are regulated. CARD19 has previously been shown to be a mitochondrial protein in HEK293T and HeLa cell lines, and it is highly transcribed in cells of myeloid origin.

In these studies, we have reported important findings regarding the basic biology of Card19: first, that the originally published narrative, in which CARD19 drives BCL10 degradation to limit NF-κB activation in Jurkat T cells, is not recapitulated in primary CD8+ T cells; secondly, that Card19 is clearly a mitochondrial protein in macrophages, interacts with MICOS and is required for normal mitochondrial function. To date, these are the first data that employ primary cells and study endogenous Card19 expression to identify its function.

ABSENCE OF CARD19 DOES NOT YIELD RESULTS CONSISTENT WITH A PUTATIVE FUNCTION DRIVING BCL10 DEGRADATION

We employed a combination of confocal microscopy and SIM imaging to demonstrate that endogenous Card19 is a mitochondrial protein in CD8+ T cells isolated from *Card19*+/+ mice. Endogenous Card19 clearly distributed with three mitochondrial markers: Mfn2 and MAVS (both OMM proteins) and ATP Synthase β (Fig. 5A-C). Attempts to quantify colocalization to confirm mitochondrial localization were limited by the background signal present in endogenous Card19 staining, as there is a single polyclonal antibody that reliably detects endogenous Card19, and the expression level of

Card19 is low. To further validate the organelle-specific localization of Card19, we employed confocal microscopy to examine distribution of Card19 and Calnexin, an ER marker (Fig. 8A). Again, colocalization quantification was not possible, due to a high background to signal ratio. However, upon comparison of single-channel images of Card19 and Calnexin signal, "gaps" of Calnexin signal in the Card19 single channel do not overlay with the Card19 signal. In contrast, comparison between single-channel images of Card19 and the mitochondrial markers regularly filled the same signal "gaps". Our biochemical fractionation data indicates that, in the microsomal fraction, which contains the ER along with plasma membrane (PM) and unbroken cells, there was a small amount of Card19 present; however, this was comparable to the amount of Tom20 also present in the microsomal fraction, indicating that this is likely just mitochondrial contamination of unbroken cells within the microsomal fraction (Fig. 8B). Coupled with the results of our biochemical fractionation data (Fig. 8B), which indicate that Card19 is stringently in the mitochondrial fraction, it is evident that endogenous Card19 is specifically a mitochondrial protein in CD8+ T cells. Interestingly, examination of 3×FLAG-Card19 expressed in CD8+ T cells from *Card19 -/-* mice via SIM provided a more nuanced view of the localization of Card19. While 3×FLAG-Card19 clearly distributed with ATP Synthase β in individual mitochondria, there was not clear colocalization between the two proteins. SIM imaging provides significantly more resolution than confocal microscopy; this distribution provides evidence that Card19 and ATP Synthase β do not co-complex within the mitochondria. It is also possible that the discrete distribution of these proteins within the mitochondria is because our data strongly suggest that Card19 is an OMM protein, and ATP Synthase β is known to be an

IMM protein. Specifically, ATP Synthase β is present in the crypts of the cristae. Although the resolution of SIM is insufficient to resolve between proteins at the OMM and the IBM, which are only approximately 20 nm apart, the crypts of the cristae and the OMM may be far enough apart such that proteins at these respective sub-mitochondrial localizations can be resolved, depending on the length of the cristae. It is notable that SIM imaging revealed that while ATP Synthase β exhibited a contiguous staining pattern within the mitochondria, 3×FLAG-Card19 exhibited a more punctate appearance. This may be a bona fide staining pattern; however, it is also possible that this pattern is somehow a consequence of the presence of the 3×-FLAG tag on full-length Card19 or the binding affinity of the anti-Card19 antibody. However, this clustering pattern is consistent with previous reports of super-resolution microscopy performed against MICOS components. Stimulated emission depletion (STED) microscopy performed against endogenous Mic60, Mic19, Mic10 and Sam50 in adult human primary fibroblasts exhibited distinct protein clusters which were not evenly distributed across the mitochondria (76). In contrast, labeling of endogenous Tom20 exhibited less discrete clustering and was evenly distributed across the mitochondria (76). Labeling of endogenous Mic60 and ATP Synthase β in the adult human primary fibroblasts also yielded consistent results that we have seen when analyzing Card19 via SIM: ATP Synthase β does not exhibit distinct clustering, whereas Mic60 exhibits clear clustering unevenly distributed along the ATP Synthase β staining (76). Therefore, the punctate distribution of endogenous Card19 imaged by SIM is likely a real phenomenon and may indicate that Card19 participates in discrete mitochondrial signaling processes consistent with a MICOS regulating protein. Together, these data are consistent with previous

reports that full-length Card19 is a mitochondrial protein; however, we did not find that endogenous Card19 was an ER protein, which was reported in subcellular fractionation in HEK293T cells overexpressing CARD19 (30).

Prior to our work, there was no published data examining the role of Card19 in primary cells. Furthermore, there was no published data confirming that the previously reported function of Card19, based on overexpression analysis, was valid in primary T cells. To address this gap in knowledge, we compared expression of Bcl10 and markers of NF-κB activation in CD8+ T cells isolated from *Card19* +/+ and *Card19* -/- mice (Fig. 9). We expected that if Card19 bound and drove degradation of Bcl10 as well as limited NF-κB activation after TCR engagement, that in the absence of Card19, we would see both the accumulation of Bcl10 as well as accumulation of NF-κB activation markers. To our surprise, however, there was little difference in the activation kinetics between *Card19* +/+ and *Card19* -/- CD8+ T cells. Bcl10 was readily degraded and resynthesized in cells of both genotypes. Furthermore, IκBα degradation and p- IκBα exhibited similar kinetics, as did additional markers of NF-κB activation and CBM complex formation. Most interestingly, it appeared that *Card19* -/- CD8+ T cells displayed slightly less resynthesis of Bcl10 and IκBα, as well as slightly less expression of NF-κB-dependent activation markers by 120 minutes. These data would indicate that, in direct contrast to the previous model of CARD19 as a negative regulator of BCL10 signaling, *Card19* -/- CD8+ T cells exhibited modestly less T cell activation instead of greater activation, perhaps because Card19 plays a role in regulating metabolic processes that are required for sustained T cell activation, such as nucleotide generation (41). The intensity of Card19 expression does not change after TCR engagement, which further

indicates that Card19 does not regulate T cell activation. These results are not consistent with the originally reported function of Card19 (or our own data in cell lines with high levels of Card19 overexpression), which supported that Card19 can drive Bcl10 degradation and limit NF-κB activation (138).

To our knowledge, there is only one report of Bcl10 recruitment to the mitochondria, which occurs in murine embryonic fibroblasts upon viral infection (77). However, we are aware of no reports of Bcl10 either alone or as part of the CBM complex being recruited to the mitochondria in T cells upon TCR engagement. Given that endogenous Card19 is clearly a mitochondrial protein and given that our T cell experiments did not support the originally published function of Card19, we investigated whether endogenous Card19 and Bcl10 interact in primary CD8+ T cells (Fig. 9). We first measured endogenous Card19 and endogenous Bcl10 interactions via confocal microscopy. We chose to examine unstimulated CD8+ effector T cells as well CD8+ T cells stimulated for 20 minutes, because at 20 minutes post-stimulation we are able to observe discrete Bcl10 punctae (129). In untreated CD8+ T cells, there was no apparent colocalization between Card19 and Bcl10; this is unsurprising given that Bcl10 is normally diffuse in the cytosol when T cells are not activated, and our observations were consistent with this distribution. Upon T cell stimulation, it was not clear whether Card19 and Bcl10 puncta were colocalized. They did appear to be in close distribution with each other, but close proximity could be due to the fact that CD8+ T cells have a very limited amount of cytosol because the nucleus fills up most of the cell. Therefore, Bcl10 and Card19 could appear close together because of the physically limited space, without actually interacting or occupying overlapping areas of the cell. To further clarify

potential interactions between endogenous Card19 and endogenous Bcl10, we isolated mitochondria from unstimulated CD8+ T cells and CD8+ T cells stimulated with anti-CD3ε for 20 minutes. We expected that, if Card19 and Bcl10 interacted, we would see either Card19 in the cytosolic fraction, Bcl10 in the mitochondrial fraction, or both. However, Bcl10 was strictly limited to the cytosolic fraction. There was some contamination of Card19 in the microsomal fraction, but it was primarily enriched in the mitochondrial fraction. Crucially, Card19 and Bcl10 were not present in any fractions together, indicating that in primary cells, endogenous Card19 and endogenous Bcl10 do not, in fact, interact. Again, this is in direct contrast to previous reports that CARD19 directly binds to BCL10.

It is unclear why CARD19 appears to inhibit NF-κB activation in HEK293T cells and Jurkat T cells upon stable overexpression. The only report of NF-κB inhibition in Jurkat T cells was in the original publication that identified Card19; however, we have since demonstrated and published that the CARD19 (then called BinCARD) construct used in the original study represents the spurious protein product of an incompletely spliced gene product (138; 196). The fully spliced mRNA of *CARD19* is expressed at much higher levels than the (partially) spliced RNA counterpart of the originally identified cDNA. We also did not observe a protein product of a size consistent with BinCARD-1 when probing western blots with an anti-CARD19 antibody (which can detect both proteins with equivalent efficiency (138), consistent with the fully spliced Card19 gene product being the only biologically relevant protein product of the Card19 gene. Therefore, it seems likely that overexpression of the artifactual BinCARD, which was reported to have cytosolic and nuclear expression, that led to the interaction with

BCL10 and subsequent effect on NF-κB activation. Indeed, our own work examined the activity of both the originally reported BinCARD protein and the biologically relevant CARD19, and we found both proteins inhibited NF-κB activation upon transient transection of CARD19 in HEK293T cells, with CARD19 having a stronger inhibitory activity (138). This phenotype was only apparent upon the overexpression of full-length CARD19; overexpression of various CARD19 truncation mutants and the G73R CARD mutant mostly or entirely abrogated this inhibitory activity (138). We noted during these experiments that full-length CARD19 was rapidly proteolyzed and therefore was difficult to detect via western blots, whereas the various mutants were much more stable (138). We therefore propose that, by an unknown mechanism, full-length CARD19 is rapidly turned over when overexpressed in HEK293T cells; overexpressed full-length CARD19 interacts with BCL10 in the HEK293T cells, and these proteins are degraded together, thus having the effect of limiting NF-κB activation. The mutant derivatives, however, are relatively stable, and fail to drive BCL10 degradation; thus, the effect of NF-κB inhibition is lost. We further propose that these interactions occur only under conditions of high overexpression, when CARD19 spills over into the subcellular compartment in which BCL10 resides. It is clearly apparent from our work examining endogenous Card19 in primary murine T cells that Card19 does not interact with Bcl10 or inhibit NF-κB activation, in large part because these two proteins have a non-overlapping subcellular distribution. Although we only performed these studies in CD8+ T cells, these results are translatable to CD4+ T cells, since CBM complex signaling is conserved between CD8+ and CD4+ T cells. We have seen no evidence that Card19 would redistribute to non-mitochondrial locations after activation in, for example, CD4+ T cells, given that this did

not occur upon TCR engagement in CD8+ T cells, and we have shown that Card19 has a transmembrane and is therefore an integral mitochondrial protein, rather than a peripheral mitochondrial protein (Fig. 12B). Holistically, we argue that the originally proposed role of CARD19 as a driver of BCL10 degradation in T cells upon TCR engagement is spurious one.

CARD19 IS A MICOS INTERACTING PROTEIN IN MACROPHAGES

High expression of CARD19 in myeloid cells has been reported in gene expression databases (46; 161; 176). For example, there is nearly four times as much *CARD19* RNA detected in classical human monocytes when compared to human naïve or memory CD8+ and CD4+ T cells (176). Since our data linked the absence of Card19 with macrophage-linked phenotypes, we investigated the function of Card19 in macrophages. We used both primary BMDMs and spleen or blood-derived macrophage cell lines for these experiments.

Endogenous Card19 is a mitochondrial protein in BMDMs

We first employed SIM imaging of BMDMs co-stained with anti-Card19 and mitochondrial markers (Fig. 12). As in our confocal microscopy and SIM imaging of endogenous Card19 in CD8+ T cells, endogenous Card19 is clearly distributed to the mitochondria of macrophages. Within individual mitochondria, both Mavs and ATP Synthase β have a more contiguous staining pattern than Card19, which is very punctate in its distribution. This is consistent with our SIM imaging in CD8+ T cells, as well as with the SIM imaging results of 3×FLAG-Card19 expressed in the *Card19 -/-* macrophage cell line, which also appears to very punctate in appearance, particularly in comparison to the Tom20 labeling. Coupled with the results of our proteinase K

protection assays, which indicate that 3×FLAG-Card19-TagRFP-T is an OMM protein, these data strongly suggest that Card19 organizes into discrete complexes along the outer mitochondrial membrane in macrophages. This may indicate that Card19 transmits signals from the cytosol to the IMM, and furthermore that Card19 operates at discrete mitochondrial complexes. It is also possible that the punctate appearance is due to Card19 self-associating and forming homodimers.

Given that 3×FLAG-Card19-ΔTM has a cytosolic distribution, we can rule out the possibility that Card19 is a peripheral OMM protein, as these data show it is anchored to the OMM via its transmembrane domain. It is notable that the Card19 transmembrane domain is not in the N or C terminus; most integral OMM proteins are anchored to the OMM via a distal C-terminus or N-terminus transmembrane domain. Instead, the transmembrane domain in Card19 is between both termini, leaving the N terminus and the C terminus to overhang on either side of the membrane. This may indicate that Card19 interacts with proteins both via its N terminus – most likely via the CARD – and as well as its C terminus. This could also indicate that Card19 also acts as a sensor to transmit signals from the cytosol to the IMS or IMM, which is supported by our proteinase K protection assay, which suggests that the N terminus of Card19 is oriented to the cytosol and the C terminus is oriented to the IMS. It is further notable that 3×FLAG-Card19-Δ146 distributes to the ER rather than the mitochondria, since this indicates that Card19 may contain a mitochondrial targeting sequence (MTS) in its C terminus that is required for final translocation to the mitochondria. All OMM proteins are translated in the cytosol and then transported directly to the mitochondria, where they are imported into the OMM and IMM via TOM and SAM complexes (148). These

proteins normally contain a cleavable MTS in the N terminus, although there are certainly precedents for a C Terminus MTS (99; 148). Analysis of the amino acid sequence of murine Card19 and human CARD19 with publicly available MTS tools do not predict the presence of an MTS, which is unsurprising given that is unlikely to be a conventional MTS. Additionally, we know very little about the confirmation of the C-terminus, since there has been no x-ray crystallography work performed on the C-terminus thus far (30). Nonetheless, it is clear that Card19 is a mitochondrial protein. It is possible that Card19 is translated at the rough ER and then translocated to the mitochondria via an MTS in the C terminus but given that all OMM proteins to date are not translated in the ER, this is a less probable explanation. It is more likely that the deletion of amino acid residues 146 to 183 do not fully delete the MTS but disrupt the MTS enough that Card19 mislocalizes to the endoplasmic reticulum. Interestingly, Mic19 is reported to exist in two redox forms, and fully oxidized Mic19 is assembled with MICOS via an intramolecular disulfide bond in yeast (144). This redox state is important for the translocation of Mic19 to the IMM via the mitochondrial IMS assembly pathway (144). Since x-ray crystallography was only performed on the CARD-containing N terminus of CARD19, we do not know if Card19 has similar, fully oxidized cysteines and redox sensitive disulfide bonds in the C terminus, as well (30). It is possible that, like Mic19, Card19 contains a redox sensitive domain in the C terminus that is required for the final translocation of Card19 to the mitochondria, and the distal deletion of the C terminus eliminates these residues. Systematic mutagenesis of individual cysteines in the C-terminus may help to further clarify this potential function

3xMyc-Card19 interacts with components of the MIB and Mic19-Mic60-Mic25 subcomplex

Based on our initial mass spectrometry data, there were clearly multiple candidates for interacting-partners for Card19 (Fig. 14). We focused primarily on candidates which were part of the same complex, since this increased the likelihood that the interaction was authentic. MIC19, MIC60, and MIC25 are well-established to organize into a MICOS subcomplex at the cristae junction; furthermore, it has also been reported that SAM50 and MTX2 interact specifically with the MIC19-MIC60 subcomplex to form the IMB (168; 200). Furthermore, there were very few mitochondrial contaminants – for example, there was no detectable Tom20 present in the mass spectrometry results. This gave us confidence that this was a true, specific interaction. We then attempted to confirm these results via western blots. However, we were only able to reproducibly validate that 3×Myc-Card19 immunoprecipitated with Sam50 and Mic19. The fact that we were only able to confirm Sam50 and Mic19 may be the result of a few factors. Firstly, there are limited antibodies available for Mic25 and Mtx2, which are not heavily studied. Thus, insufficient signal-to-noise may be a factor preventing confirmation of these interactions. However, Mic60 is regularly studied and there are many reliable commercial antibodies available. Thus, a second possibility is that the immunoprecipitation protocol we employed to detect binding partners via mass spectrometry was distinct from the protocol for confirmation via western blot. Specifically, for mass spectrometry, we utilized a commercially sourced kit from ChromoTek, which is highly specific, does not required the use of Sepharose G beads or antibody, and requires only limited steps that could introduce disruptive mechanical forces (such as spins). By contrast, for confirmation via western blots, we used a standard IP protocol in which permeabilized cells were pre-cleared with Sepharose G

beads, incubated overnight with a mouse monoclonal anti-myc antibody, incubated again with Sepharose G beads, and heat inactivated. This protocol requires significantly more steps which introduces more opportunity for proteins to dissociate from 3×Myc-Card19. It appears likely that Card19 interacts very strongly (possibly directly) with both Sam50 and Mic19, whereas the interactions with Mtx2, Mic25, and Mic60 may be indirect, due to these proteins being in a complex with Sam50 and Mic19. Alternatively, Mtx2, Mic25, and Mic60 are simply lower affinity directly interacting partners. In this case, the entire IMB and Mic19-Mic60-Mic25 subcomplex may be detected by this method more readily by using a cross-linking technique. Thirdly, difficulty in detection may be due to decreased relative abundance of Mic25 and Mtx2 in the mitochondria compared to Sam50 and Mic 19. Again, however, this is unlikely to be true for Mic60, which is an abundantly expressed IMM protein. It is most likely that the true explanation is a combination of these three possibilities.

That Card19 would interact directly and specifically with Sam50 and Mic19 is consistent with the previously reported model of the MICOS subcomplexes. The results of the SIM imaging of 3×Myc-Card19 and Mic19-3×OLLAS co-expressed in the *Card19* -/- macrophage cell line support this interaction; whereas endogenous Tom20 was contiguously stained across the entire mitochondrial membrane, both 3×Myc-Card19 and Mic19-3×OLLAS displayed a distinct punctate appearance; often the respective punctae were co-distributed within the mitochondria (Fig. 14) . While the SIM data alone is insufficient to prove a direct interaction between Card19 and Mic19, the punctate formation of both proteins is consistent with other reports of super-resolution microscopy analyses of MICOS components in individual mitochondria, and it certainly supports that

Card19 has a specific interaction with the Mic19-Mic60 subcomplex when considered with the IP data (76). 3×Myc-Card19-Δ146 does not appear to interact with Mic19 or Sam50; it is unsurprising that mislocalized Card19 no longer interacts with a protein in the inner mitochondrial membrane when its interacting partner is relegated to the ER. However, we were surprised to see that 3xMyc-Card19-G73R also did not interact with either Mic19 or Sam50, despite the fact that it localizes to the mitochondria and maintains a punctate distribution in the OMM. As our data suggests that the N terminus of Card19 is exposed to the cytosol, it seems unlikely that the IMM protein Mic19 binds directly to Card19 via the CARD. Hypothetically, Sam50 could interact with Card19 via the CARD in the N terminus, since both are OMM proteins, but there certainly is not a precedent for Sam50 to bind to CARDs. The G73R mutant was generated in a glycine in the helix 4-5 turn, which is conserved in CARDs across species (30; 33; 138). Mutations of this glycine to arginine in CRADD and CASP2 prevents CARD-CARD interaction by disrupting the helix 4-5 conformation (30; 33; 138). Therefore, it is likely that the interaction between Card19 and Sam50 or Mic19 is ultimately dependent on the conformation of the CARD. In the case of Mic19, the interaction between Card19 and Mic19 is likely to regulated by the conformational change in the CARD conferring a subsequent conformational change of the C-terminus of Card19, since it is unlikely that a cytosolic CARD (Card19) interacts directly with a peripheral IMM protein (Mic19). This indicates that Card19 may act as a sensor that transmits signals to MICOS to regulate it; alternatively, it could indicate that the CARD may be required an early sorting process and interaction with a mitochondrial chaperone protein that is required for its final colocalization with MICOS, given that redox-sensitive disulfide bonds in other proteins

have already been shown to be required for mitochondrial import (144). However, since we have been unable to probe for Mic60 or Mic25 thus far using traditional IP methods followed by western blotting, we are unable to conclude whether the conformational change in G73R mutant CARD subsequently affects interaction of the C-terminus of Card19 with Mic60 or Mic25.

Card19 interacting partners are not wholly consistent between cell types

Interestingly, in the publicly available proteomics screen, MTX2 and MIC19 have been reported to interact with CARD19 in HTC116 cells (68; 69; 149). CARD19 was also reported to interact with MIC27 and MTX2 in HEK293T cells (68; 69; 149). Mic27 did not appear as high-likelihood targets in any of our proteomics experiments. Additionally, we did not observe any of the other interacting partners that were reported to interact with CARD19 in the BioPlex screens (68; 69; 149). We were most surprised to find that neither Trak1 nor Trak2, which consistently pulled down CARD19 in both the HEK293T cells and the HTC116 cells in the Bioplex proteomics screen, did not feature in our own proteomics results. The discrepancies between some of the previously reported interacting partners of Card19 may simply be because HEK293T and HTC116 are human cell lines, whereas we used a mouse macrophage cell line for our proteomics studies.

It is also likely that Card19 has tissue and cell-specific functions. Indeed, considering the particular importance of metabolic, and especially OXPHOS regulation, has on immune cells such as macrophages, it would be unsurprising that Card19 has more specific functions in macrophages than in epithelial or fibroblast cell lines. It is also possible that the type and location of the tags used in the Bioplex study interfere with the

localization and interactions proteins which interact with Card19. The Bioplex study has not reported to use Card19 as a "bait" protein; Card19 has only ever featured in the screen as a "prey"; that is, it was reported to interact with various proteins expressing a FLAG and HA tag on its C terminus. Anecdotally, we have observed that expression of the FLAG or myc tag, but not an RFP tag, on the C-terminus interferes directly with the localization of Card19 to the mitochondria, leading instead to expression of Card19 in the ER (data not shown). Therefore, there may be similar discrepancies with other tagged proteins. Additionally, the authors of the Bioplex study did not quantify to what degree each of the tagged bait constructs were overexpressed. It is possible that overexpression led to spurious interactions and/or loss of authentic interactions. As we have reported previously, overexpression is clear issue for Card19 in particular.

In one paper published in 2019, Card19 was reported to be a positive regulator of interferon responses (166). Specifically, the authors indicated that silencing of CARD19 in HEK293T cells decreased the release of type I Interferons in response to various virus stimuli (166). Furthermore, the authors reported that HA-CARD19 interacted with FLAG-MAVS in a manner dependent on the transmembrane domain but not the CARD of CARD19 under untreated conditions (166). Their conclusions were dependent on confocal microscopy and immunoprecipitation followed by western blotting of immunoprecipitates (166). However, Mavs was not identified as an interacting partner in any of our proteomics screens. Additionally, MAVS was not reported to interact with CARD19 in the Bioplex proteomics screen; indeed, there was no overlap reported between the interacting partners of CARD19 and MAVS in the Bioplex study. This discrepancy may be due to the fact that we did not stimulate the cells with an activator of

Mavs signaling in our experiments; indeed, it seems unlikely that we would identify a Mavs-Card19 interaction without the use of an appropriate stimuli such as poly (I:C), poly (dA:dT), or viral infection. However, it is notable that the authors of this publication did not use any stimuli to induce the interaction they observed between CARD19 and MAVS (166). It is possible that HA-CARD19 and FLAG-MAVS were overexpressed to such a degree that the proteins have an artifactual interaction that does not occur at physiological expression of either protein. Additionally, both CARD19 and MAVS contain CARDs in the N terminus, and it is well-established the interactions between CARD-containing proteins typically occur via the CARDs. Despite this, the authors expressed the HA tag and the FLAG tag on the N termini of CARD19 and MAVS, respectively. The impact this may have on the interaction of these two proteins is uncertain. It is possible, too, that Card19 does interact with Mavs in non-macrophage cell types, given that the evidence that CARD19 interacts with MAVS was identified in HEK293T, HeLa, and A549 cells. While it is certainly interesting that CARD19 may play a role in antiviral defense, the data we have reported here is not consistent with a constitutive Card19-Mavs interaction in unstimulated macrophages.

However, our lack of evidence supporting a Card19-Mavs interaction in untreated macrophages does not indicate conclusively that such an interaction does not occur in macrophages upon viral infection or under conditions of mitochondrial stress. Since both Card19 and Mavs are mitochondrial proteins that contain N-terminal CARDs oriented to the cytosol, it is feasible that Card19 and Mavs would oligomerize upon stimulation with poly (I:C) or viral infection. Even in the absence of a direct interaction of Card19 and Mavs, Card19 loss-of-function mutations could still impact Mavs oligomerization and

signaling. The production of mROS has been shown to augment Mavs oligomerization; Mavs mediates viral-infection induced apoptosis, and the mitochondria is a key regulator of apoptosis (23; 42; 96; 118). The increased mROS in the absence of Card19 could potentiate Mavs-driven interferon signaling. Additionally, mitochondrial dysfunction in the absence of Card19 could also potentiate Mavs-mediated apoptosis. Of course, this would suggest that Card19 acts as a negative regulator of interferon signaling rather than the positive regulator it has already been reported to be (166).

CARD19 PROTECTS AGAINST MITOCHONDRIAL DYSFUNCTION

MICOS deficiencies have been studied extensively in various human cell lines. Downregulation of various MICOS components causes mitochondrial dysfunction phenotypes. Most commonly, defects in MICOS cause the formation of aberrant cristae, swollen mitochondria, and other indications of dysfunction such as altered MMP, altered OXPHOS, and increased mROS. Distorted cristae morphology is the most commonly reported defect, usually accompanied by altered or total loss of the presence of cristae junctions. Abnormal cristae can appear as stacks, onion-like layers, vesicular, or even the complete absence of apparent cristae. Upon examination of the cristae within *Card19 +/+* and *Card19 -/-* BMDMs via TEM, there was some evidence of distorted cristae (Fig.15/16). Primarily, this manifested as the increased presence of vesicular cristae within *Card19 -/-* BMDM mitochondria. The assessment of this phenotype is complicated by the fact that, unlike in cell lines, the morphology of cristae, and indeed of mitochondria overall, is heterogenous in primary cells. Additionally, due to limitations in the quality of the cristae resolution and contrast within the images, we were unable to consistently quantify other markers of distorted cristae, such as the number and width of

cristae junctions. Notably, the treatment of LPS increased the presence of vesicular mitochondria in both wild-type and knock-out BMDMs (Fig. 15B). However, this change between untreated and LPS-treated mitochondria was not drastic, as the number of mitochondria with vesicular cristae increased by 3 percent in wild-type cells and increased by 6 percent in knock-out cells (Fig. 15B). It is possible that the modest change is due to our inability to identify further types of distorted cristae.

Interestingly, the presence of some vesicular cristae has been reported in HeLa cells treated with siRNA against *MIC19* and *MIC60* (80; 158). Indeed, knock down of *MIC19* and *MIC60* in HeLa cells resulted varied aberrant cristae, including arc-shaped cristae, single membrane cristae and cristae stacks (158). Another study that employed shRNA to ablate MIC19 expression in HeLa cells also displayed fewer lamellar increased and increased vesicular or "tubular" cristae, along with reduced overall cristae amount and decreased CJ diameter (36). Our investigation of the cristae in *Card19* +/+ and *Card19* -/- fibroblasts murine lung fibroblasts yielded similar morphological results as knock down of *MIC19* and *MIC60* in HeLa cells, with clear, consistent lamellar mitochondria in the wild-type fibroblasts and obviously aberrant cristae of varied morphology in the knock-out fibroblasts (Fig. 16). These cristae morphology in *Card19* -/- lung fibroblasts included arc-shaped cristae, cristae stacks, and vesicular cristae (Fig. 16). However, we did not quantify CJ diameter or the total amount of cristae present as has been performed in other MICOS studies. Notably, there were no apparent concentric circles of cristae in either the *Card19* -/- BMDMs or fibroblasts; this is also consistent with published data on distorted cristae morphology that indicate that concentric circles of cristae are more common in defects of MIC26 and MIC27 (6; 80; 85).

Examination of other markers of mitochondrial dysfunction provide a more complete picture of the effect rendered by the absence of Card19. The decrease in OCR measured by Seahorse Extracellular Flux in *Card19 -/-* BMDMs was very modest (Fig. 17). This is not entirely unexpected; ablation of MICOS components in cell lines have conflicting reports on the impact on OCR. SiRNA knockdown of *MIC60* and *MIC19* in HeLa cells has been reported to have little to no impact on the OCR; however, in another study, shRNA knockdown of *MIC19* dramatically reduced OCR (36; 158). Furthermore, lentivirus-mediated shRNA knockdown of *MIC25* and *MIC60* in RKO and MCF7 cells resulted in a modest decrease of only approximately 3 nmol/mol*minute in OCR relative to wild-type counterparts (5). This was coupled with a dramatic decrease in directly measured ATP production (5). Overall, this is consistent with what we have reported, in which *Card19 -/-* BMDMs exhibit a basal OCR approximately 10 pmol/minute less than *Card19 +/+* BMDMs. It is worth nothing that oxygen consumption as a measure of oxidative phosphorylation should be interpreted with caution. While OCR measurements at basal level and after the addition of drugs can be useful, especially in healthy cells, it cannot always give a clear picture of the status of unhealthy cells. The OCR reduction in *Card19 -/-* BMDMs may be due to an overall reduction in metabolism in the cells; it also could be a direct indication of inefficient oxidative phosphorylation, especially when considering that the maximum OCR that can be achieved by *Card19 -/-* BMDMs is also approximately 20 pmol/minute less than that of *Card19 +/+* BMDMs. Given that the ECAR was also reduced in *Card19 -/-* BMDMs, it is possible that in the absence of Card19 and when cultured in glucose-rich media, the cells are less metabolically active, further complicating interpretation of these results (Fig. 17B). The results from the

Seahorse Extracellular Flux analysis alone are not a sufficient measure of mitochondrial dysfunction but coupled with our TEM cristae data, there is strong evidence of mitochondrial dysregulation.

It was also striking to find that absence of Card19 led to larger population of mitochondria with a decreased membrane potential (Fig. 18A). Decreased MMP is a hallmark of mitochondrial danger and is the initial step that triggers mitophagy (79). There are reports of both increased and decreased MMP as a result of MICOS deficiency: siRNA knockdown of *MIC60* in HeLa cells caused increased MMP; however, siRNA against *MIC60* delivered by transfection to rat H9c2 cells and HEK293 cells caused decreased MMP (80; 108). The decreased MMP we have observed in *Card19 -/-* BMDMs may be due to "leakiness" of the cristae junction, in which protons are able to escape from the cristae more readily, thus reducing membrane potential. However, the decreased MMP could simply be downstream of other mitochondrial dysfunction, such as the increased mROS we observed in the absence of Card19. Indeed, MIC60 ablation in HeLa cells, H9c2 cells, and HEK293 cells caused increased basal mROS (80; 108). It is therefore notable that basal levels of mROS were increased in the absence of Card19, and *Card19 -/-* BMDMs were more sensitive to producing mROS in response to lower levels of LPS stimulation relative to wild-type cells (Fig. 18B/C). The sensitivity of *Card19 -/-* BMDMs to produce mROS at low levels of LPS stimulation that do not yield increased mROS in *Card19 +/+* BMDMs suggests that this mROS production is mediated by ETC complex I, where LPS-induced mROS is primarily produced (25; 62). Antimycin A, which we used as a control, is an inhibitor of ETC complex III, and therefore presumably also drives mROS production at complex I. It is likely that we did not see a difference in

mROS production after AA treatment in wild-type and knock-out BMDMs because we used AA at a higher concentration, similar to how we did not see differences in mROS production after 6 hours of 500 ng/ml of LPS treatment. It is possible that we may see differences in mROS production after stimulation of BMDMs with a lower AA concentration and a decreased stimulation time. The transient overexpression of myc-MIC26 and FLAG-MIC27 in HeLa cells also drives a reduction in basal OCR and an increase in ROS (85). Thus, it is possible that these phenotypes are a result of compensatory increased expression of the Mic26-Mic27-Mic10-Mic13 subcomplex. Together, these data strongly indicate that absence of Card19 in BMDMs corresponds to hallmarks of mitochondrial dysfunction and bioenergetic dysregulation that is consistent with previous reports of MICOS dysregulation.

Card19, MICOS, and Disease

Based on the data we have presented in this paper, in which Card19 interacts with MICOS proteins and protects against mitochondrial dysregulation in macrophages, we argue that Card19 may be a regulator of processes which, when dysregulated, are major drivers of inflammatory and neurodegenerative diseases. Disease etiology linked to Card19 defects could be driven by MICOS dysregulation alone, by the inflammation initiated by mitochondrial danger signals in macrophages and microglia, or some combination of the two.

MICOS defects and associated diseases

A range of diseases have been linked to deficiencies in MICOS dysfunction; these diseases are primarily neurodegenerative. One mutation in MIC13 has been reported to cause pathology in humans: an infant patient presenting with bilateral kidney stones,

hepatopathy, lactate acidosis, and mitochondrial encephalopathy was found to have a homozygous mutation in a splice site in the gene encoding MIC13, resulting in two truncated splice variants, one with a frameshift mutation (204). The patient also displayed psychomotor retardation and global muscular hypotonia (204). The patient was found to have distorted cristae and mitochondria in muscle and fibroblasts. Fibroblasts isolated from the patient did not produce MIC13 and had highly diminished MIC10 levels (204). This resulted in the absence of MIC27-MIC10 subcomplexes but the sustained presence of MIC60-MIC19 subcomplexes (204). A pathogenic hemizygous mutation in MIC26 was identified in a Brazilian family; specifically, the eight-year-old child of non-consanguineous parents presented with symptoms such as inflammatory symptoms such as vomiting, fever and diarrhea (15). Later, the patient presented with neurological symptoms such as developmental delays, hypotonia, fatigue, irritability, autistic behavior cognitive impairment (15). The patient also exhibited repeated infections, along with acidosis and an altered carnitine profile (15). Interestingly, the child's mother, who was heterozygous for the mutation, and multiple female family members presented with symptoms such as cognitive disorders, fatigue and increased blood lactate (15). The eight-year-old male patient and his mother were treated with carnitine and Coenzyme Q10, which effected apparent improvement (15).

We are aware of no case reports in which a loss-of-function mutation in a MIC19, MIC60, or MIC25 has explicitly been identified as the causative agent of a disease. Similarly, we are currently aware of no reports of homozygous loss-of-function mutations in CARD19 which have been identified as the definitive cause of human disease in any case studies. Indeed, examination of predicted pathogenic/likely pathogenic loss of

function mutations in CARD19 reported in the genome Aggregation Database (gnomAD) (http://gnomad.broadinstitute.org) indicates that no individuals are homozygous for predicted pathogenic loss-of-function mutants of CARD19. This may indicate that homozygous loss-of-function mutations in most MICOS components as well as CARD19 are in fact embryonic lethal in humans. While it is not surprising that loss-of-function mutations in MICOS would be embryonic lethal, it is surprising that this is the case for CARD19, considering that *Card19 -/-* mice do not appear to have difficulty reproducing or carrying pups to term. Indeed, *Card19 -/-* mice are generally healthy in spite of the neurological phenotypes we have observed. We have been able to maintain ataxic and hyperactive mice until they are at least two years of age. It is possible that there is simply not enough research surrounding CARD19 to permit identification of homozygous mutations causing pathology or being linked to increased likelihood of disorders. A closer and systematic assessment of available data on reported CARD19 SNPs may yield further information on the role of CARD19 in human disease.

Although there is only one report of a case study of a pathogenic loss-of-function mutation in MIC13 or MIC26, there is certainly abundant evidence that MICOS components are linked to neurodegenerative diseases. One group observed that in a model of ALS-C9 in Drosophila muscle, G4C2 poly(GR) C9orf72 strongly interacted with Mic27 (101). This interaction led to decreased subcomplexing of Mic10 with Mic27 and an increased subcomplexing of Mic10 with Mic60, Mic19, and Opa1 (101). These altered interactions resulted in increased MMP, Ca2+ and K+, and the authors proposed that this may be due to tightening of CJ junctions leading to decreased osmolyte exchange in the mitochondria (101). In another study, when CHCHD2 mutants R145Q

and Q126X, which have been linked to Parkinson's disease, were expressed in isogenic human embryonic stem cell (hESC) lines, these cells displayed reduced overall OXPHOS function measured by OCR and western blot analysis of OXPHOS component expression (213). Furthermore, upon the expression of these mutants in NPCs derived from these isogenic hESC, there were few cristae in the mitochondria when analyzed by TEM; there was a also a reduction in the expression of MIC60, MIC10, MIC19, and MIC25 (213). The mitochondrial dysfunction observed in these cells were rescued by treatment with Elamipreptide, a mitochondrially targeted peptide thought to rescue mitochondrial dysfunction, by increasing expression of MICOS components (213).

The development of apparent ataxia and possible hyperactivity in *Card19 -/-* mice seems to be consistent with data indicating that proteins of the MIC19-MIC60-MIC25 subcomplex are linked to neurodegenerative disorders. These neurological phenotypes exhibit incomplete penetrance, as only 30% of the female *Card19 -/-* mice developed ataxia, and only four female mice have developed apparent hyperactivity; this indicates that any disease that may be caused by Card19 mutations has a complicated etiology and may require concurrent mutations in other genes to cause pathology. There has been one report of several rare *MIC60* variants identified in a cohort of patients with Parkinson's disease (175) . Interestingly, several of these rare variants were missense mutations in the MTS of MIC60 – indicating that perhaps, mutations in the putative MTS of Card19 may also be pathogenic (175). This would not be surprising, given that we have shown that distal deletion of the C terminus of Card19 leads to mislocalization. Indeed, upon expression of the MTS missense *MIC60* variant transgenes in drosophila, these variants did not localize to the mitochondria and reflected a diffuse, presumably cytosolic,

distribution (175). Furthermore, drosophila expressing these variants displayed significant motor issues, reduced adult viability, and "onion-like" mitochondria in muscle tissue (1; 175). The authors of this investigation do not report if the patients with rare *MIC60* missense variants also exhibited *PINK1* mutations. Given that *PINK1* mutations are commonly associated with PD, and given that PINK1 can regulate cristae architecture and mitophagy by phosphorylating MIC60, it seems likely that there are multiple avenues in which disruption of this process may mediate pathogenesis (1; 45; 175).

Mitochondrial dysfunction and associated diseases

To our knowledge, MICOS defects have not been linked to any inflammatory disorders. Indeed, there is very little available investigation into the role of MICOS in immune cells. To date, there has been no reported work investigating the role of MICOS in primary macrophages. However, there is abundant evidence that mitochondrial dysfunction and dysregulation of CARD-mediated signaling processes in macrophages are linked to immune dysregulation disorders. Furthermore, dysregulation of mitochondrial turnover and chronically dysfunctional mitochondria are clearly implicated in a range of pathologies. Indeed, mitochondrial dysfunction is linked to various neurodegenerative disorders, including amyotrophic lateral sclerosis (ALS), Parkinson's disease (PD), CMT2a, Alzheimer's disease, and multiple sclerosis (MS) (12; 48; 64; 94; 111; 119; 127; 136; 143; 185; 186). Mitochondrial dysfunction has also been linked to immune dysregulation disorders such as irritable bowel disease (IBD) as well as various forms of fibrosis (67; 90; 111; 119; 136; 185; 188; 211). Mitochondrial dysfunction in microglia, in particular, is a major driver of neurodegenerative disorders. Friedrich's ataxia, for example, is mediated by mitochondrial dysfunction in microglia due to

deficiency of the protein Frataxin (152). ALS is reported to be driven by a combination of dominant SOD1 mutations in both motor neurons and microglia (21). While microglia dysfunction does not appear to be required for the development of ALS, it does appear to promote late disease progression (21). Microglia morphology can be an indicator microglia activation and disease state (63). For example, in murine model of Autism spectrum disorder (ASD), Autophagy related gene 7 (Atg7) was selectively deleted from myeloid cells in mice, thus rendering the cells unable to undergo autophagy (83). The morphology of these defective microglia looks strikingly similar to the microglia we observed in the brain sections of *Card19 -/-* mice, with shortened, fragmented extensions (Fig. 21) (83). Given that there is precedence for neurodegenerative disorder driven by mitochondrial dysfunction and microglia defects, and CARD19 is highly transcribed in microglia, the phenotypes we have observed in *Card19 -/-* mice likely arose from mitochondrial-dysfunction driven microglia dysregulation. This is strengthened by the fact that we see no evidence of astrogliosis, eliminating at least one alternative explanation for the mechanism of these neurological phenotypes (Fig. 20). However, since these observations were made in germline knock-outs, and since we have not yet performed any further analyses examining other cell types such as oligodendrocytes, we currently lack the evidence to make strong statements about the etiology of these phenotypes. Since *Card19 -/-* mice also display elevated levels of macrophage-specific cytokines, *Card19 -/-* BMDMs display resistance to cell death induced by bacterial infection, and mitochondrial dysfunction is linked to immune dysregulation and inflammation, it is also possible that CARD19 mutants may be linked to increased risk of diseases such as IBD as well as increased risk of bacterial and viral infections. There is a

distinct balance inherent in inflammation: inflammation is required for the control of bacterial and viral infections, yet much of the damage rendered to the host is often caused by the host inflammatory response itself. *Card19 -/-* mice may be more sensitive to producing inflammatory cytokines, just as we observed that *Card19 -/-* BMDMs are more sensitive to producing increased mROS at low levels of LPS stimulation, because they are already in a "primed" state due to mitochondrial dysfunction. In the context of an infection, this may manifest as increased inflammation, but coupled with increased overall bacterial or viral burden and ultimately failure to resolve the infection. Indeed, mitochondrial dysfunction coupled with increased survival of BMDMs in the absence of Card19 may explain why *Card19 -/-* mice injected with LPS produce higher levels of TNF-α, IL-6, and MCP-1. Overall, the connection between mitochondria dysfunction, especially in microglia and macrophages, indicates that CARD19 mutations may be potently capable of initiating and/or potentiating neurodegenerative diseases and inflammation.

FUTURE DIRECTIONS

Our work constitutes the only analysis of the function of endogenous Card19 in primary cells to date. Many additional questions have organically emerged from the body of these experiments, providing both immediate and long-term avenues of investigation.

Card19 regulation of MICOS

Immediate experiments should further investigate the mechanism by which Card19 interacts with MICOS. Presumably, Card19 is a regulator or a previously undefined required subunit of MICOS, given that its absence promotes mitochondrial

phenotypes commonly seen upon MICOS deficiency. Previous reports indicate that MICOS and MICOS-interacting proteins participate in MICOS regulation via distinct functions. SAM50 and MTX2, for example, do not actively manipulate formation of subcomplexes, per se (36; 168; 200). Rather, these proteins are key scaffolding proteins, which upon interaction with MIC19, form the IMB, which stabilizes the localization of MIC19-MIC60 subcomplexes (36). This, in turn, has a significant impact on the number and width of cristae junctions in the mitochondria. In contrast, MIC19 is the principal protein required to connect SAM50 and MTX2 to the MIC60-MIC19-MIC25 subcomplex. Cleavage of MIC19 by OMA1 ablates CJ formation and causes the loss of cristae shape (36). Several experiments can address the role of Card19 in this paradigm. Firstly, immunoprecipitation of Mic19-3×OLLAS expressed in the *Card19* +/+ and *Card19* -/- macrophage cell lines followed by analysis by western blot can inform whether Card19 is required for the formation of the IMB. Specifically, if Card19 is required for this bridge formation, then presumably when Card19 is absent, Mic19 will not immunoprecipitate with Sam50, or the amount of Sam50 present in the pulldown will be decreased. It is also possible that Card19 plays a role in either promoting or inhibiting the IMB by exposing or shielding the N-myristoyl modification in Mic19 for cleavage. This could be assessed by comparing expression of Mic19 in *Card19* +/+ and *Card19* -/- macrophages – first in the cell line, then in BMDMS – via western blot. If Card19 promotes Mic19 cleavage, then in its absence, there should be increased expression of full-length Mic19 in *Card19* -/- cells; if Card19 inhibits Mic19 cleavage, then we can expect observe decreased full-length Mic19 and increased expression of cleaved, lower molecular weight Mic19 (also called short-Mic19 or S-Mic19). Full length Mic19 and S-

Mic19 have an approximately 10 kDa size difference, so the respective bands are easily resolvable via western blot (168). Mic19 also contains a conserved phosphorylation site immediately following the myristoylation site at Thr11, which is a substrate for Protein kinase 1 (Pka1) and in the phosphorylated state inhibits recruitment of Parkin following mitochondrial membrane depolarization (1). In conjunction with this mechanism, MIC60 also contains a phosphorylation site that is reportedly a target of PKA1, and phosphorylated MIC60 inhibits the recruitment of both PINK1 and Parkin to depolarized mitochondria (1). While these functions appear independent of MICOS function, it is worthwhile to measure the phosphorylation status of Mic19 and Mic60 compared in *Card19 +/+* and *Card19 -/-* macrophages using an anti-phospho-Mic19 antibody and anti-phospho-Mic60. As far as we are aware, there are none commercially available; however, one group reported producing this antibody in rabbits, which were used to demonstrate that MIC19 and MIC60 are phosphorylated by PKA (1). It is possible we could request some of this antibody for our own use; alternatively we could generate our own antibodies using the published peptide sequences reported by this group (1).

To further investigate the role of Card19 in MICOS regulation, comparison of whole cell lysates isolated from *Card19 +/+* and *Card19-/-* macrophages will be vital. Previous publications examining the effects of downregulation of specific, individual MICOS components reported decreased expression of both other MICOS proteins as well as key components of the electron transport chain. Decrease of Mic19, Mic60, and Mic25 in the absence of Card19 would indicate that Card19 is required to stabilize the Mic19-Mic60 subcomplex. Likewise, decreased expression of ETC Complex I – IV in the absence of Card19 would support this function. It would also be worthwhile to assess

the impact of the absence of Card19 on the expression of Mic27-Mic26-Mic13-Mic10 the alternative MICOS subcomplex, since instability and degradation of the Mic19-Mic60-Mic25 subcomplex could lead to either a corresponding destabilizing and decrease or compensatory stabilization and subsequent increase in Mic27-Mic26-Mic13-Mic10 expression.

Directly related to the specific role of Card19 is the question of what regulates Card19. X-ray crystallography of the CARD of Card19 revealed three cysteines that could be fully oxidized. Card19 was suggested to act as a redox sensor by this authors of the X-ray crystallography study (30). This hypothesis is strengthened by the fact that, in the absence of Card19, BMDMs exhibit both increased basal mROS as well as increased sensitivity of production of mROS upon LPS stimulation. The superoxide species of mROS are produced in the matrix and to some degree, the intermembrane space; superoxide is not membrane permeable, and thus Card19 is unlikely to act as a direct sensor for mROS as the N-terminus is presumably exposed to the cytosol (59; 115; 155). However, superoxide is readily reduced in the mitochondria to hydrogen peroxide, which is membrane permeable and maintains a strong reducing capacity. Card19 may undergo a conformational change that permits its association with Mic19, Sam50, and Mtx2 under cellular conditions induced by mROS. Upon a change in the redox state of the cell, Card19 dissociates from MICOS, thus permitting cristae alteration that generates more mROS. In this case, Card19 would act as the sensor in a feedback mechanism that acutely measures and mediates MICOS-regulated responses to the redox state of the cell. Interestingly, this would provide a link between innate immunity and Card19 functionality. Reactive oxygen species, including those generated by the mitochondria,

are well-established mechanisms employed against intracellular bacterial and viral infections. In such a case, Card19 could provide a link between infection in the cell and mitochondrial involvement in innate defenses. The capacity of Card19 as a sensor for reactive oxygen species can be investigated via a series of experiments. The most straightforward technique to experimentally assess this function would be to treat *Card19 -/-* macrophages expressing 3×Myc-Card19 and its derivative mutants with exogenous hydrogen peroxide. Proteins that bind to 3×Myc-Card19 upon this treatment can be measured via immunoprecipitation followed by mass spectrometry and western blots, as we have performed previously. We can then detect if Card19 has altered interactions with Sam50, Mtx2, Mic19, Mic60, and Mic25. Additionally, via mass spectrometry, we can detect if there are additional proteins which engage Card19 upon changes in the redox potential of the cell. To determine if these interactions are dependent on the three cysteines previously reported to be capable of being fully oxidized, these experiments can be repeated using mutants which contain point mutations in one or all of the cysteines (30). We can further probe the role of Card19 as a reactive oxygen species sensor by measuring its interactions with MICOS upon treatment of *Card19 -/-* macrophages expressing 3×Myc-Card19 with known inducers of mROS, such as LPS, Antimycin A, and Rotenone, followed by measurement of its interactions with MICOS proteins via immunoprecipitation and western blot or mass spectrometry. While the exact mechanism of the generation of mROS upon MICOS dysfunction are unclear, Rotenone and Antimycin A are well-documented to induce mROS by inhibiting ETC Complexes I and III, respectively. LPS elicits mROS through a more specific pathway in macrophages; TLR-4 engagement by LPS induces mitochondrial association of the protein ESCIT,

which promotes mROS at ETC Complex I. If LPS elicits alterations in Card19 interactions measured by mass spectrometry, whereas Antimycin A and Rotenone do not, this would indicate a TLR4, ESCIT-specific mROS mechanism is involved in Card19 functionality. Additionally, it is vital to test these outcomes not only at levels of stimulations at which there is detectable mROS present, but also in the context of suboptimal stimulation that does not induce detectable mROS. Differences in Card19 interactions with the IMB and Mic19-Mic60-Mic25 subcomplex upon mROS inducing versus non-mROS inducing stimulation would indicate that Card19 participates in signaling that is not directly responsible for sensing mROS, but that absence of Card19 and thus lack of participation in such a pathway permits increased mROS formation indirectly.

The formation of aberrant cristae in the absence of Card19 also warrants further investigation. Blind scoring of mitochondria in *Card19* +/+ and *Card19* -/- BMDMs of mitochondrial features is required. Use of an imaging software such as Zen or ImageJ to outline the cristae within the mitochondria may improve reliable categorization of cristae morphology. Since the morphology of the cristae may is more homogenous in the fibroblast cell line, this may be true in the macrophage cell line, as well. Furthermore, measurement of the number and width of cristae junctions is a vital measure of MICOS regulation. Altered width of cristae junctions has been described to promote ion leak from the cristae to the inner boundary membrane. If *Card19* -/- BMDMs have wider CJs than *Card19* +/+ BMDMs, this may partially contribute to the increased population of mitochondria with decreased MMP we have observed in *Card19* -/- BMDMs.

Finally, it should be noted that it is well documented that cancers and cell lines tend to preferentially utilize glycolysis over OXPHOS for ATP production (124; 180; 189). In contrast, inactivated BMDMs are relatively quiescent and primarily utilize OXPHOS to generate ATP. In light of this, metabolite switching experiments may reveal more dramatic phenotypes than we have already observed. The media used for the macrophage cell line and BMDMs is DMEM containing 4.5 g/L glucose, which is approximately 25 mM. This is level of glucose is not comparable to, for example, the concentration of fasting blood glucose levels in a healthy mouse, which is reported to be between 80 to 100 mg/dL, or approximately 4.4 mM to 5.5 mM (55; 173). Even the average diabetic mouse has a fasting blood glucose of only 200 mg/dL, or approximately 11.1 mM (55; 173). While blood glucose levels certainly will increase after consumption of food, persistent high glucose availability is not necessarily a biologically accurate experimental condition. While high glucose availability permits cells of both the wild-type and knock-out genotype to survive for experimental use, it is probable that repeating measures of mitochondrial dysfunction with decreased glucose availability would yield more dramatic and physiologically accurate phenotypes. Comparisons of mROS and MMP, for example, between *Card19* +/+ and *Card19* -/- BMDMs in high (25 mM) versus low (2.5 mM) glucose levels in media may yield stronger MitoSox Red and TMRE staining measured by flow cytometry. Additionally, experiments can similarly be performed with media containing glucose versus media containing galactose. Galactose is more difficult for cells to metabolize; it is ultimately metabolized via glycolysis but produces no net ATP. Therefore, cells must rely on OXPHOS for ATP production.

Presumably, *Card19 -/-* BMDMs will show exacerbated markers of mitochondrial dysregulation in the presence of low glucose or galactose.

Mitochondrial Dysfunction and Dysregulated Inflammation

One of the phenotypes early *Card19 -/-* phenotypes we observed was that *Card19 -/-* mice injected with LPS produced higher levels of TNF-α, IL-6, and MCP-1 relative to *Card19 +/+* mice. Mitochondrial dysfunction has been linked to immune dysregulation disorders such as IBD (107; 111; 119; 136). Not only can the danger signals elicited from damaged mitochondria activate apoptosis and, in macrophages, pyroptosis, but these danger signals also initate mitochondrial turnover, particularly mitophagy. Indeed, decreased MMP, as we observed in the *Card19 -/-* BMDMs via flow cytometry, is the initiating step of mitophagy signaling cascade. It has been demonstrated in BMDMs that LPS-mediated activation of mROS will not only activate the inflammasome, but the resultant NF-κB activation from TLR4 engagement has a twofold response: first, to drive the transcription of pro-inflammatory cytokine and inflammasome precursors and second, to initiate p62 mediated mitophagy (210). This indicates that pro-inflammatory pathways within macrophages contain self-regulatory mechanisms to limit activation. As we have shown that, in the absence of Card19, mitochondria in BMDMs clearly show signs of dysfunction, some of which are exacerbated upon LPS stimulation, it is crucial to examine the inflammation-LPS-mitochondrial dysfunction connection more closely.

We have performed preliminary experiments measuring the release of IL-6 and TNFα via ELISA from *Card19 +/+* and *Card19 -/-* BMDMs untreated or treated with LPS (data not shown). Initial results indicated that *Card19 -/-* BMDMs may produce higher amounts of TNFα and IL-6 after 18 hours of stimulation with LPS. However,

these results have proved to be inconsistent and difficult to normalize to total cell number and viable cell number. To accurately measure the cytokine response of BMDMs as a result of LPS stimulation, RT-PCR quantification of TNF-α and IL-6 transcription, along with other markers such as NF-κB, IL-1β, and IL-18 transcription can be performed. Transcription of these target genes can be normalized to genes that have previously been reported to remain stable under LPS stimulation, such as Heterogenous nuclear ribonucleoprotein A/B (*Hnrnpab)* or Syntaxin 5a (*Stx5a)* (167). Since mROS has been explicitly linked to the activation of the inflammasome in macrophages, as well, and since the mROS production is acute in *Card19 -/-* BMDMs, it is likely that these are explicitly linked. To assess this, the RT-PCR experiments can be repeated with the addition of a commercially available mROS scavenger such as MitoTempo. If the elevated mROS produced in the absence of Card19 participates in driving elevated pro-inflammatory cytokine production, then treatment with MitoTempo will reduce the transcription of these cytokines in *Card19 -/-* BMDMs.

The capacity of mROS and mitochondrial dysfunction to promote dysregulation is not limited to the context of TLR engagement or intracellular infection. Abundant evidence supports that mitochondrial dysfunction due to the loss of mitochondrial integrity can lead to the development of various pathologies via activation of pyroptosis or apoptosis at inappropriate times or levels (12; 107; 119; 136; 143; 146; 186). Furthermore, these pathologies can be caused, or exacerbated by, defects in mitochondrial turnover (109; 127). Alternatively, mitophagy in macrophages can prevent critical apoptosis by eliminating damaged mitochondria; in this case, the disruption of apoptosis, which is necessary for homeostasis and is thus a necessary process, leads to

disease, as is the case for models of pulmonary fibrosis in mice (90). Mitophagy has also been implicated to play a protective role in response to a broad range of pro-apoptotic and pro-pyroptotic stimuli in a wide variety of cell types (10; 17; 38; 67; 90; 98; 105; 125; 127; 132; 162; 165; 185; 187; 188; 193; 199; 201; 207; 208; 211; 214). Since both Parkin and PINK1 have been shown to regulate mitophagy and cristae morphology via interactions with MIC19 and MIC60, dysregulated mitophagy is another avenue by which absence of Card19 can promote accumulation of mitochondrial damage (1; 175). Indeed, we have preliminary data which indicates that there is increased p62 punctae formation measured by confocal microscopy but decreased expression of autophagy marker p62 and LC3 measured by western blot in *Card19 -/-* BMDMs after treatment with LPS or the uncoupler CCCP (data not shown). These data do indicate that there may be dysregulation of autophagy – and more specifically, mitophagy – in the absence of Card19. This paradigm can be further analyzed through a series of experiments. Firstly, p62 recruitment to mitochondria can quantified by quantifying colocalization of p62 punctae with a strong mitochondrial marker such as Tom20 via confocal microscopy. If Card19 regulates Mic60-mediated mitophagy, then we can an alteration in the number of p62 punctae which form at the OMM in the absence of Card19. Furthermore, we suspect that the decrease in autophagy markers that we observed in our preliminary western blot data from *Card19 -/-* BMDM lysates is likely due increased autophagy or mitophagy, since p62 and LC3 are degraded as part of the autophagy process. We can confirm this by pretreating *Card19 +/+* and *Card19 -/-* BMDMs with autophagy inhibitors such as bafilomycin and 3-methyladenine (3-MA), treat the BMDMs with LPS or CCCP, and collect the lysates. Lysates can then be probed for autophagy-specific and mitophagy-

specific markers p62, LC3, Pink1 and Parkin. If absence of Card19 does indeed lead to an increase in mitophagy, we can expect to see accumulation of both autophagy and mitophagy markers measured via western blot.

In 2015, the Brodsky lab at the University of Pennsylvania identified a striking phenotype: *Card19 -/-* BMDMs displayed resistance to a variety of cell death stimuli, including classic activators of the inflammasome, as well as classic activators of caspase-3 mediated apoptosis. These data were measured by an LDH release assay and confirmed via a propidium iodide assay. At first, our collaborators pursued the possibility that Card19 interacted with the caspases or CARDs involved in these pathways, as this appeared to be most likely. However, absence of Card19 did not appear to decrease caspase recruitment or activation. Our collaborators were able to confirm the mitochondrial localization of Card19 in BMDMs. Ultimately, their data suggested that *Card19 -/-* BMDMs displayed a subtle defect in the amount of cleaved Gasdermin present in the cytosol (18) . However, they were unable to directly connect this defect to the identifiable function of Card19. Considering that Card19-deficient mitochondria display signs of dysfunction, the relationship between the observed mitochondrial danger signs and the resistance to cell death is worthy of further investigation. Gasdermins are responsible for the insertion and subsequent pore formation in the penultimate execution of pyroptosis. Gasdermin D (GsdmD) is the principle gasdermin family protein which has been studied; however, very little is known about the other Gasdermin proteins and its specific role in pyroptosis. Interestingly, cleaved Gasdermin E (GsdmE) as well as GsdmD have been reported to augment inflammasome-driven pyroptosis by forming pores in the mitochondria, thus releasing cytochrome c into the cytosol and initiating the

apoptosome (140). This paradigm can be tested for a role in *Card19-/-* BMDM cell death resistance by a combination of western blot analysis and microscopy. Firstly, the localization of endogenous GsdmE and GsdmD will be measured in *Card19* +/+ and *Card19* -/- BMDMs that are untreated or treated with pyroptosis stimuli, such as LPS or Nigericin with ATP. GsdmD and GsdmE may be localized to the cytosol in an untreated state, but upon stimulation – perhaps prompted by Card19 after the release of mitochondrial danger signals – will translocate to the OMM. However, since Card19 is absent in knock-out macrophages, this translocation will not occur. Mitochondrial danger signals such as mROS will still activate the inflammasome, permitting some pyroptosis to occur, which is consistent with what we have previously observed. Subcellular fractionation in *Card19* +/+ and *Card19* -/- BMDMs followed by western blot analysis of cleaved GsdmD and GsdmE in the mitochondrial fraction can be performed. If Card19 promotes recruitment of cleaved GsdmD and GsdmE to the mitochondria, whether by direct interaction or indirectly by altering mitochondrial morphology, then we expect that there will be reduced recruitment of cleaved GsdmD and GsdmE at the mitochondrial fraction. Again, this would not prevent cell death from occurring entirely, but rather would reduce the time required to achieve cell death as well as the total amount of cell death occurring at a specific timepoint. Interestingly, this could provide an answer to how *Card19* -/- BMDMs appear to resistant to both apoptotic and pyroptotic cell death stimuli.

Card19 and Immune Responses

Mitochondrial are significant centers of immune cell signaling. Not only does TLR stimulation induce mitochondrial danger signals, but mitochondria contain proteins

such as Mavs, which are key mediators in antiviral defense. Additionally, the generation of ROS by the mitochondria is a key antimicrobial effector. Activation of the inflammasome is also a key component in controlling intracellular infection by driving inflammation. Indeed, *Caspase1 -/-* mice infected with *Shigella flexneri* displayed drastically decreased signs of inflammation such as decreased edema and immune cell infiltration; however, these same mice did not survive infection and exhibited high bacterial loads (145). Furthermore, although the evidence supporting the direct interaction between Card19 and Mavs is sparse, the role of Card19 as a positive regulator of Type I Interferons should be clarified. It is unclear whether Card19 absence provides an inherent advantage or disadvantage against infection of BMDMs.

Mitophagy, mROS, and inflammasome activation are protective against intracellular bacterial infection. Considering that *Card19 -/-* mice display elevated levels of mROS and decreased MMP, which can drive inflammasome activation and mitophagy respectively, absence of Card19 may provide an inherent benefit to BMDMs upon infection. This can be tested by performing Gentamicin protection assays in *Card19 +/+* and *Card19 -/-* BMDMs. BMDMs are infected at an MOI of 10 to 100; the viable cells are then treated with Gentamicin, an antibiotic, which kills *Shigella* while leaving the BMDMs unaffected. After multiple washes, the BMDMs are permeabilized with a Triton-X 100 solution; the resultant supernatant is used to plate serial dilutions on TSB-Congo Red agar plates, which are the standard plates used for *Shigella*. After 16 hours of growth, the bacterial yield is quantified by counting the colonies that have grown on the plates. If the absence of Card19 confers an antibacterial advantage, then the bacterial load from *Card19 +/+* BMDMs will be higher than that of *Card19 -/-* BMDMs. To test

whether this advantage is due to the increased presence of mROS, the Gentamicin protection assay can be repeated with the added condition of MitoTempo treated cells. If the advantage is indeed due to the presence of increased mROS, then the addition of MitoTempo should abrogate that advantage and result in relatively equal bacterial loads from the BMDMs of both genotypes. To test if increased mitophagy confers an advantage in the absence of Card19, Gentamicin protection assays can be performed with in combination with autophagy inhibitors such as 3-MA or Baf-1. It would be best to test this in combination with genetic manipulations of autophagy, to account for off-target effects of autophagy inhibiting drugs; *Parkin -/-* or *Pink1-/-* mice crossed with *Card19 -/-* can be used to derive BMDMs that are deficient in both mitophagy and *Card19*. The same approach can be used to generate BMDMs to test the effect of the inflammasome, by crossing *Caspase1 -/-* mice with *Card19 -/-* mice to generate double-knockouts; the BMDMs derived from these mice can again be used in Gentamicin protection assays.

Beyond the relevance of mROS and its role in bactericidal activity in macrophages, there is some limited evidence that mROS may play a role in regulating phagocytosis indirectly by modulating HIF-2α (37). In this limited context, under normoxic conditions, unstimulated macrophages expressed basal levels of HIF-2α that induced expression of the PRR macrophage receptor with collagenous structure (MARCO) by promoting basal mROS levels (37). To determine if absence of Card19 and the commensurate increase in mROS modulates this pathway, we can measure phagocytosis using Zymosan particles labeled with a fluorescent dye. Phagocytosis is then quantified measuring the fluorescent intensity of the engulfed beads using a plate reader. We would expect that if mROS promotes the inhibition of MARCO-driven

phagocytosis, then *Card19 -/-* BMDMs would display decreased fluorescence intensity corresponding to decreased engulfment of the Zymosan beads. Additionally, we can measure expression of Hif-2α and MARCO via western blot of whole-cell lysates; we would expect that *Card19 -/-* BMDMs would display increased Hif-2α and decreased MARCO expression. Presumably, alteration in phagocytosis and bactericidal activity will also impact the ability of macrophages to present antigen on the cell surface. To measure this indirectly, we can detect the amount of MHC II displayed on the surface of BMDMs via flow cytometry. We can expect that, if *Card19 -/-* BMDMs display enhanced antigen presentation due to enhanced bactericidal activity, then in the absence of Card19, BMDMs will express elevated MHC II. Alternatively, however, it is possible that *Card19 -/-* BMDMS will display decreased MHC II due to decreased antigen presentation, corresponding to Hif-2α-driven suppression of phagocytosis.

To investigate the putative interaction between Card19 and Mavs, as well as measuring the potential function of Card19 as a positive regulator of interferons, we can employ techniques we have previously used with some alterations. Although 3xMyc-Card19 did not precipitate with Mavs in our study, this may be limited by the fact that this was performed under untreated conditions. Instead, the *Card19 -/-* macrophage cell line expressing 3xMyc-Card19 can be untreated or treated with poly I:C as well as VSV. We can then measure immunoprecipitation of Mavs with 3xMyc-Card19 by a combination of mass spectrometry and western blots. We also would expect to detect CARD proteins Rig-I or Mda-5 via mass spectrometry, since both of these CARD-containing PRRs bind directly to Mavs upon sensing viral moieties (197). However, we may have difficulty observing Rig-I or Mda-5 in traditional IPs followed by western

blotting, since Card19 may not directly interact with these proteins and only directly interact with Mavs. The putative interaction can further be confirmed by confocal microscopy and SIM to observe Card19-Mavs colocalization upon poly I:C or VSV stimulation. The putative role of Card19 as a positive regulator of interferons can be assessed by comparing the transcription of IFN-β and IL-6 via RT-PCR between *Card19 +/+, Card19 -/-*, or *Card19 -/- + 3×Myc-Card19* macrophage cell lines upon treatment with poly I:C or infection with VSV. If Card19 is a positive regulator of interferon signaling, then the *Card19 -/-* macrophage cell line will exhibit reduced transcription of IFN-β and IL-6. These phenotypes should be rescued by the expression of 3×Myc-Card19 in the *Card19 -/-* macrophage cell line. If the 3×Myc tag interferes with the functionality of Card19, an untagged construct can be expressed in the cell line instead. Finally, the overall ability of macrophages to control viral infection in the absence of Card19 can be measured by infecting *Card19 +/+* and *Card19 -/-* BMDMs with VSV. The BMDMs can then be lysed, and the viral burden can be measured by both a plaque assay as well as RT-PCR. If Card19 promotes Mavs-mediated interferon production, then in all likelihood, in the absence of Card19, there will be an increased viral burden. In contrast, since mROS production has been shown to augment Mavs oligomerization and subsequent Type I interferon responses, it is possible that Card19 is in fact a negative regulator of Type I interferons, and the mROS produced in the absence of Card19 will promote Mavs signaling post-oligomerization. In that case, we would expect to see both a decreased viral burden and increased production of Type I interferons in the absence of Card19.

Investigation of mass spectrometry candidates in T cells

While we identified MICOS proteins as interacting partners in macrophages, we have not confirmed these results in other cell types. It is likely that the MICOS-Card19 interaction is conserved in other cell types, since both Mic19 and Mtx2 were reported to pull down with Card19 in HTC116 cells in the BioPlex study. Additionally, the BioPlex reported a diverse range interacting partners reported in HEK293T cells, it is likely that Card19 has non-MICOS functions outside of macrophages.

To confirm that Card19 interacts with MICOS in T cells and to identify putative non-MICOS interacting partners, we will repeat our immunoprecipitation and mass spectrometry experiments as performed in the macrophage cell lines. BMDMs are very difficult to transduce, and therefore we relied on immortalized macrophages for our mass spectrometry experiments; in contrast, primary murine T cells are readily transduced. Briefly, we will harvest the spleen and lymph nodes from *Card19 -/-* mice and isolate CD8+ T cells using the DynaBeads™ Untouched™ Mouse CD8 T Cell kit (ThermoFisher, #11417D). Isolated CD8+ T cells will be seeded on plates coated with anti-CD3ε and anti-CD28 for 48 hours. The CD8+ T cell blasts will then be collected and transduced via spinfection with a vector expressing 3xMyc-Card19. As a control, a sample of *Card19 -/-* CD8+ T cells will be transduced with an empty vector. We will then perform immunoprecipitation and mass spectrometry as described in the methods section. Putative candidates will be confirmed by repeating immunoprecipitation with Protein G Sepharose beads and western blotting. We expect to find that Card19 interacts with Mic19, Sam50, Mic60, Mtx2, and Mic25 in T cells as it does in macrophages.

Currently, very little data regarding MICOS in T cells exists. One report in 2019 found that human CD8+ T cells simultaneously stimulated with PD-1 and restimulated

with anti-TCR/CD3 displayed both decreased ECAR and OCR, decreased maximal OCR, and reduced relative H+ leak compared to CD8+ T cells restimulated without the presence of PD-1 (121). Remarkably, this corresponded to decreased MMP as well as reduced expression of various mitochondrial proteins, especially MIC19 and CHCHD10 (121). PD-1 stimulation also decreased the number of cristae present in restimulated CD8+ T cells, increased the number of cells without any cristae present, and furthermore reduced cristae length, as measured by TEM (121). MIC19 silencing by lentivirus-delivered shRNA resulted in decreased MMP as well as decreased intracellular IFNγ measured via flow cytometry (121). Following confirmation of the interaction between Card19 and Mic19 in CD8+ T cells via mass spectrometry, we can assess if Card19 plays a role in this dynamic. To determine if Card19 participates in this paradigm upon PD-1 stimulation, we can measure expression of Card19 in *Card19* +/+ CD8+ T cells after PD-1 and anti-CD3 stimulation via western blot. Furthermore, we can compare cristae structure, MMP and intracellular IFN-γ levels via TEM and flow cytometry in *Card19* +/+ and *Card19* -/- CD8+ T cells after PD-1 and anti-CD3 stimulation. Similar to the results exhibited upon silencing of MIC19, we would expect to see decreased cristae quality, decreased MMP, and decreased intracellular IFN-γ. Reconstitution of Card19 in *Card19* -/- CD8+ T cells by retrovirus transduction would rescue this phenotype.

Card19 and Immunometabolism

There is considerable evidence that MICOS defects cause mitochondrial dysregulation, with varying results including increased mROS, decreased OCR and ATP production, and decreased MMP. Oxidative phosphorylation is generally the preferential pathway for ATP production in both inactivated T cells and BMDMs, which are

quiescent. After activation, T cells undergo metabolic reprogramming and preferentially use aerobic glycolysis. Similarly, after stimulation with LPS or IFNγ, BMDMs are polarized to the pro-inflammatory M1 state and also preferentially use aerobic glycolysis for fuel. Since MICOS defects affect OXPHOS, it seems unlikely that MICOS defects will explicitly affect the activation state of T cells or M1 BMDMs by restricting available ATP. The proliferation of *Card19* +/+ and *Card19* -/- CD8+ T cells can be measured by stimulating the T cells with anti-CD3/anti-TCR and anti-CD28; the cells can then be incubated with CFSE. After CFSE incubation, the cells can be stained with Annexin V. Proliferation can then be measured using CFSE dilution as a surrogate, whereas Annexin V can be used as a measure of viability. If Card19 has an impact on T cell proliferation after activation, then *Card19* -/- CD8+ T cells will have less CFSE dilution; they will likely also have increased Annexin V, as the cells will deplete available GMP stores earlier, and thus face increased metabolic stress and apoptosis as a result.

Although we have reported that *Card19* -/- CD8+ T cells exhibit modestly decreased markers of NF-κB activation after TCR restimulation, there is evidence that ETC complex III-driven mROS is a critical promoter of NFAT and IL-2 production upon T cell activation (151). We did not measure these markers of activation in our studies. To address this, we will isolate naïve CD8+ and CD4+ T cells from *Card19* +/+ and *Card19* -/- mice. We will activate the T cells via anti-CD3 and anti-CD28 for 0, 10, 20, 40, 60, and 120 minutes. We will then collect the cells and perform subcellular fractionation to isolate the nuclear and cytosolic fractions followed by detection of NFAT in both fractions via western blot. NFAT translocates to the nucleus upon T cell activation. If increased mROS in *Card19* -/- CD8+ and CD4+ drives increased NFAT

translocation, we expect to see increased NFAT expression in the nuclear fraction relative to *Card19* +/+ CD8+ and CD4+ T cells. Both genotypes should demonstrate some NFAT translocation upon T cell activation, but presumably this translocation will be enhanced in the absence of Card19. Additionally, we can measure the amount of IL-2 produced in CD8+ and CD4+ T cells employing RT-PCR to detect *IL-2* mRNA produced by T cells cultured for 24 hours in the presence of anti-CD3 and anti-CD28 activation. If the absence of Card19 effects NFAT-mediated IL-2 production via increased mROS, we expect that *Card19* -/- CD8+ and CD4+ T cells will exhibit increased *IL-2* mRNA relative to *Card19* +/+ CD8+ and CD4+ T cells. This may be accompanied by corresponding increase in surface expression of CD25, the IL-2 receptor alpha chain, measured by flow cytometry.

Although mitochondrial dysfunction is unlikely to negatively affect the ability of *Card19* -/- BMDMs to polarize to the M1 phenotype, it is possible that pre-existing mitochondrial dysfunction actually promotes M1 differentiation even in the absence of exogenous stimuli or result in BMDMs mores sensitive to M1 polarization at lower levels of stimulation, by promoting aerobic glycolysis as an alternative to defective OXPHOS. Glucose uptake and lactate production can be measured in the media of *Card19* +/+ and *Card19* -/- BMDMs by commercially available colorimetric kits. If absence of Card19 promotes aerobic glycolysis, then the amount of glucose will be decreased, and the lactate increased in the media collected from *Card19* -/- BMDMs. We can compare the capacity for M0 BMDMs to polarize to M1 or M2 macrophages by stimulating wild-type and knock-out BMDMs with LPS/IFN-γ to promote M1 polarization or IL-4 to promote M2 polarization. We can then measure the success of polarization by measuring

appropriate cytokines, such as IL-6 and IL-1β for M1 BMDMs and IL-10 and IL-4 for M2 BMDMs. While *Card19 -/-* BMDMs should display no difficulty in polarizing to M1 macrophages – indeed, they may more readily polarize due to danger signals from the mitochondria – we would expect that M2 macrophage polarization would be deficient in the absence of Card19. Specifically, IL-4 and IL-10 production will be reduced in *Card19 -/-* BMDMs, since mitochondrial dysfunction will interfere with M2 metabolic reprogramming, which relies on fatty acid oxidation to fuel oxidative phosphorylation. Additionally, key polarization regulatory proteins can be compared by western blotting between wild-type and knock-out BMDMs upon M1 and M2 polarization. Specifically, we can measure Hif-1α along with Pgc-1β and Arginase. We would expect that Hif-1α expression would be similar between wild-type and knock-out BMDMs; if mitochondrial dysfunction potentiates M1 metabolic reprogramming, HIF-1α expression may in fact be higher in knock-out BMDMs. Additionally, we can expect that Pgc-1β and Arginase levels will be altered in knock-out macrophages relative to wild-type counterparts, given that the mitochondrial dysfunction will interfere with effective M2 polarization and subsequent metabolic reprogramming.

Further investigation and characterization of ataxia and hyperactivity in *Card19 -/-* mice

The apparent ataxia and hyperactivity developed in some *Card19 -/-* mice was a striking phenotype (see Appendix 1 for details). MICOS defects have been associated with some neurodegenerative disorders, such as Parkinson's Disease. Since CARD19 is most highly transcribed in microglia, followed by oligodendrocytes, it is possible that these neurological phenotypes have developed due to cellular dysfunction (206). Indeed, microglia are very similar to myeloid-derived macrophages, produce the same cytokines,

and respond to the same stimuli (184). Microglia are important caretakers of homeostasis in the brain and are required for neuronal remodeling and astrocyte function. The microglia dysfunction that may cause the ataxic and hyperactive phenotypes, furthermore, may be related to similar elevated levels of basal mROS, as we observed in *Card19 -/-* BMDMs.

To address this, we can repeat our brain immunohistochemistry studies. In addition to examining microglia and astrocytes, we can measure the morphology and staining intensity of both myelinated and non-myelinated oligodendrocytes using anti-Myelin basic protein (MBP), which is exclusively produced by myelinating oligodendrocytes and anti-Myelin oligodendrocyte glycoprotein (31), which is present on the surface of all oligodendrocytes. Furthermore, we can measure reactive oxygen species in the brain sections using dihydroethidium (DHE), a fluorescent marker that specifically interacts with superoxide. Intensity of the respective stains will be quantified by calculating the pixel intensity of each marker in at least 6 squares in each region of the brain imaged. We expect that the average staining intensity of Iba1 will be higher in brains isolated from *Card19 -/-* indicating gliosis of microglia. Similar increased intensity may be observed in oligodendrocytes. Finally, we expect that brain sections from *Card19 -/-* mice will display higher staining intensity of DHE. Furthermore, we can use previously described techniques to quantify and compare the morphology of microglia between brain sections from *Card19 +/+* and *Card19 -/-* mice (203).

We expect that the phenotypes we have observed are mediated by microglia, given that Card19 is most highly transcribed in this specific cell type. Dysfunctional

mitochondria in microglia have been reported to drive neurodegenerative disorders – indeed, one report indicates that mitochondrial impairment can potentiate microglia driven Parkinson's disease in a murine model by augmenting NLRP3 inflammasome activation (146). To confirm that the neurological phenotypes we observed in *Card19 -/-* are mediated by microglia, we can treat mice with the small molecule PLX5622 (Plexxicon Inc). PLX5622 is a brain-specific inhibitor of colony-stimulating factor 1 (Csf-1) and ultimately depletes microglia from mouse brains. This inhibitor has been previously used in a murine Alzheimer's model (153; 154). If microglia are indeed the primary agents of the neurological phenotypes we have observed in the absence of Card19, then treatment of *Card19 -/-* with PLX5622 will prevent the development of these phenotypes.

Identifying microglia as the causative agent of the observed ataxia and hyperactivity will only be effective, however, if we can identify a reproducibly measurable behavioral phenotype. DigiGait analysis was virtually impossible to complete with severely ataxic mice. Furthermore, the tape removal test did not yield significant, consistent differences between *Card19 +/+* and *Card19 -/-* mice. Additionally, the apparent phenotypes occurred after the mice reached at least 14 weeks of age. Ideally, a phenotype, even a subtle phenotype, that is clearly identifiable and reproducible in younger mice would be employed for PLX5622 studies. To address this, we will perform DigiGait analysis on age-matched, gender-matched, litter-matched mice that are younger than 10 weeks of age and do not have apparent ataxia that would interfere consistent running on the DigiGait treadmill. This will permit complete DigiGait analysis, and we may find altered gait and stride patterns in *Card19 -/-* mice. If

the DigiGait analysis does not yield an identifiable gait phenotype that can be used for the PLX5622 studies, we can investigate the hyperactivity phenotype. To quantify possibly hyperactivity, we will perform open field tests on age-matched, gender-matched, litter-matched mice that are younger than 10 weeks of age. If younger *Card19 -/-* mice do indeed display signs of increased hyperactivity – or perhaps anxiety – these mice will spend less time in the corners of the open field used in the test and will spend increased time in the center of the open field. Furthermore, we quantify the amount of time the mice spend moving – we expect that *Card19 -/-* mice will spend much more time moving than still relative to *Card19 +/+* mice.

CONCLUSIONS

Card19 is a protein of particular significance in macrophages and potentially microglia. Although Card19 does not appear to bind to Bcl10, drive its degradation, and limit NF-κB activation, it still appears to have a strong putative role in mitochondrial dysfunction, inflammation, and neurodegeneration. This body of this work not only corrects the spurious function previously assigned to Card19 but provides new insights into the true function of Card19. Together, our data supports a model in which Card19 interacts with MICOS and MICOS-interacting proteins as a component of the intermembrane bridge. The absence of Card19 promotes the formation of aberrant cristae, decreased MMP, increased mROS, and decreased OCR. Based on these data, we posit that Card19 is a regulator of the Mic19-Mic60-Mic25 MICOS subcomplex and protects against mitochondrial dysfunction. We propose a model of Card19 function, in which Card19 senses signs of mitochondrial danger, such as mROS, and regulates mitochondrial function via MICOS to maintain homeostasis (Fig. 19A). However, when

Card19 is absent, it is unable to sense signs of mitochondrial danger and regulate MICOS. As a result, there is an accumulation of mitochondrial damage, evident by distorted cristae, decreased MMP, increased mROS, and decreased OCR (Fig. 19A). We further suggest, given the connection between mitochondrial dysfunction in macrophages and microglia with inflammation and neurodegenerative diseases, that the phenotypes we have observed in individual BMDMs in the absence of Card19 may provide an underlying mechanism for ataxic and pro-inflammatory phenotypes we have observed in *Card19 -/-* mice (Fig. 19B).

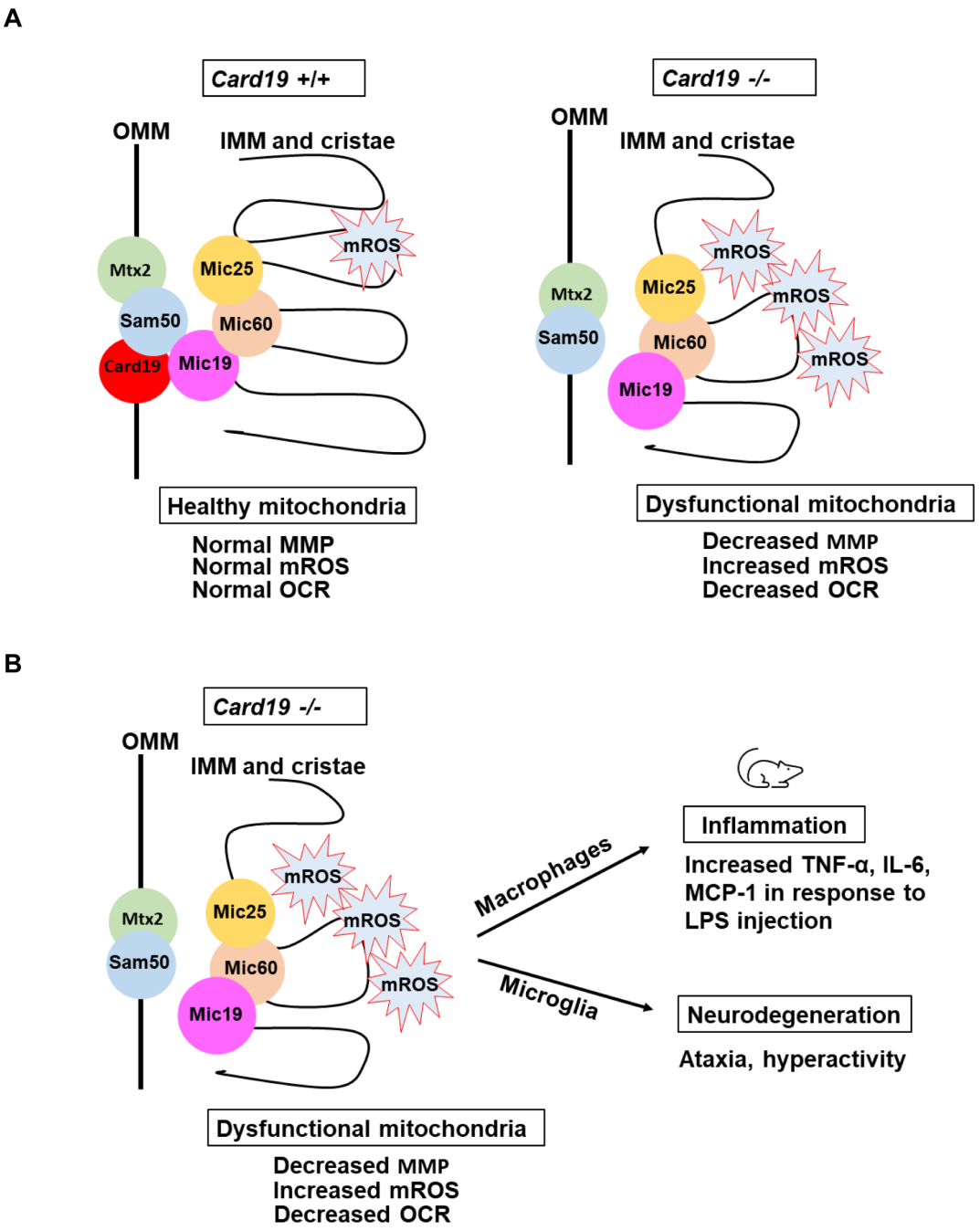

Figure 19. Schematic of Proposed Function of Card19

(A) Card19 binds to the Mic19-Mic60-Mic25 subcomplex and maintains the IMB. When Card19 is present, mitochondria are healthy. When Card19 is absent, mitochondria are dysfunctional. (B) Mitochondrial dysfunction in the absence of Card19 in macrophages and microglia may provide an underlying mechanism for phenotypes we have observed in *Card19 -/-* mice.

Appendix 1: Characterization of ataxia in *Card19 -/-* mice

CARD19 -/- MICE SPONTANEOUSLY DEVELOP ATAXIA UPON INBREEDING

In 2017, after 3 generations of inbreeding of Card19 -/- mice, two striking phenotypes appeared: 1) 30% of the female Card19 -/- mice developed mild ataxia after a minimum of 14 weeks of age, and 2) two litters of pups were born with extremely shortened tails. These mice were apparently otherwise in good health. This phenotype has been reported in a more extreme form in mice modeling CMT2a disease. In this particular model, the mice had genetic manipulation of Mfn2 expression; defects in TRAK2 have also been reported to cause CMT2a . MICOS deficiencies have reportedly been linked to CMT2a as well as other neurodegenerative disorders such as Parkinson's Disease. Mic19 has been linked to Parkinson's Disease via *in silico* and bioinformatic experiments, but has not been explicitly indicated as a cause of PD (139).

Characterization of ataxia exhibited by *Card19 -/-* mice

In order to characterize the apparent ataxia exhibited by *Card19 -/-* mice, we first attempted to quantify the traits of the gait in the wild-type and knock-out mice using the DigiGait. The DigiGait system combines a small, enclosed treadmill and a camera which tracks the gait of the fore and hindlimbs of the mouse. After processing, the DigiGait analysis generates a range of results such as stride length and more for direct comparison. Unfortunately, the ataxia in the *Card19 -/-* mice was severe enough that they were unable to run for the required amount of time needed to collect robust data. Therefore, we focused our energies on the Tape-Removal Test.

Briefly, in the first trial, mice have a small piece of red electrical tape applied to the right forepaw and yellow electrical tape applied to the left forepaw. The mouse is then placed in a clear cylinder and the amount of time required to 1) Notice the tape and 2) Remove the tape is reported. Trial 2 is the same, but with the tape switched onto opposite side paws. Regardless of the trial, yellow tape is lightly placed first and red is pressed onto the paw first. The mice undergo 5 days of successive training before the actual trial is performed in order to prevent variation. Both male and female mice were used in the test (Fig. 19A).

When analyzing the results of the test across genotype without stratifying for sex, there was significant variation (Fig. 20). There did not appear to be a difference between time to removal in trial 1, although two data groupings were apparent in the *Card19* -/- mice in trial 2 (Fig. 20B). *Card19* -/- mice also appeared to be somewhat slower to notice the tape in trial 1, although this difference was eliminated in trial (Fig. 20C). We then divided the data to compare results in male only and female only groups. The female *Card19* -/- mice were somewhat faster than *Card19* +/+ mice to notice and remove the tape in trial 1 (Fig. 20D). However, in trial 2, the female *Card19* -/- mice were generally slower to remove the tape, and there was little difference between female wild-type and knock-out mice to notice the tape (Fig.20E).

When analyzing only the male mice, we found that there was no difference in time to remove between the *Card19* +/+ and *Card19* -/- mice in trial one, but the *Card19* -/- mice were faster to notice the tape (Fig. 20F). In trial 2, the *Card19* -/- mice were faster to remove the tape, but there was no difference between the two groups in time to notice (Fig. 20G).

Interestingly, in performing these studies, we observed two additional phenotypes which may be of interest: some of *Card19 -/-*mice displayed hyperactivity. The hyperactive mice would run and circle constantly in the cage without stopping. Additionally, some of the *Card19 -/-* mice exhibited a bizarre head-flip behavior, where upon preparing to scruff the mice for tape-placement, the mice would tremble and flip the head directly back. None of the *Card19 +/+* mice displayed this strange motion.

Microglia and Astrocytes in brain sections of *Card19 +/+* and *Card19 -/-* mice

Gene expressions databases indicated that among neuronal cell types, *CARD19* is mostly highly transcribed by microglia, followed closely by oligodendrocytes (206). Microglia are highly related to macrophages, and mitochondrial dysfunction in microglia have been linked to a range of neurodegenerative disorders. Microglia are responsible not only for immune responses within the brain, but also for maintenance of neurons and astrocytes. Since *Card19 -/-* mice displayed neurological phenotypes, harvested brains from asymptomatic *Card19 +/+* and *Card19 -/-* mice, and after fixing and sectioning the brains, probed for GFAP and Iba1. GFAP is a marker of astrocytes; increased GFAP intensity is associated with astrogliosis (93). (93)Iba1 is a pan marker of microglia (74). In sagittal sections of the cerebellum, we did observe apparent differences in GFAP distribution. Quantification of GFAP staining intensity confirmed that there did not appear to be presence of astrogliosis in *Card19 -/-* sections (Fig. 21A).

Iba1 staining of sagittal sections of the cerebral cortex also did not indicate that there was increased intensity of Iba1 staining (Fig. 21B). However, upon close inspection, it is apparent that the microglia in *Card19 -/-* sections had altered morphology relative to microglia in *Card19 +/+* sections (Fig. 21B). In particular, the microglia

appeared to have fewer extensions, many of which are broken. Microglia morphology is linked to activation status and dysfunction (92). Whereas homeostatic microglia have a ramified morphology with long thin processes, as seen in *Card19* +/+ brain sections, inflammatory, activated microglia have an ameboid appearance, with no to very few thick processes (92). Dysfunctional microglia, commonly seen during Parkinson's disease, upon experiencing increased oxidative stress and inflammation, exhibit fragmented and twisted processes (92). This morphology is referred to as "dystrophic" and appears most similar to the morphology of microglia from *Card19* -/- mouse brain sections (92). Furthermore, microglia of similar dystrophic morphology were reported in a microglia with myeloid-specific deletion of Atg7, a component of the autophagy pathway, in a model of Autism Spectrum Disorder (83). A similar morphology was observed in the microglia of coronal sections of the cerebral cortex in *Card19* -/- brain sections (Fig. 22).

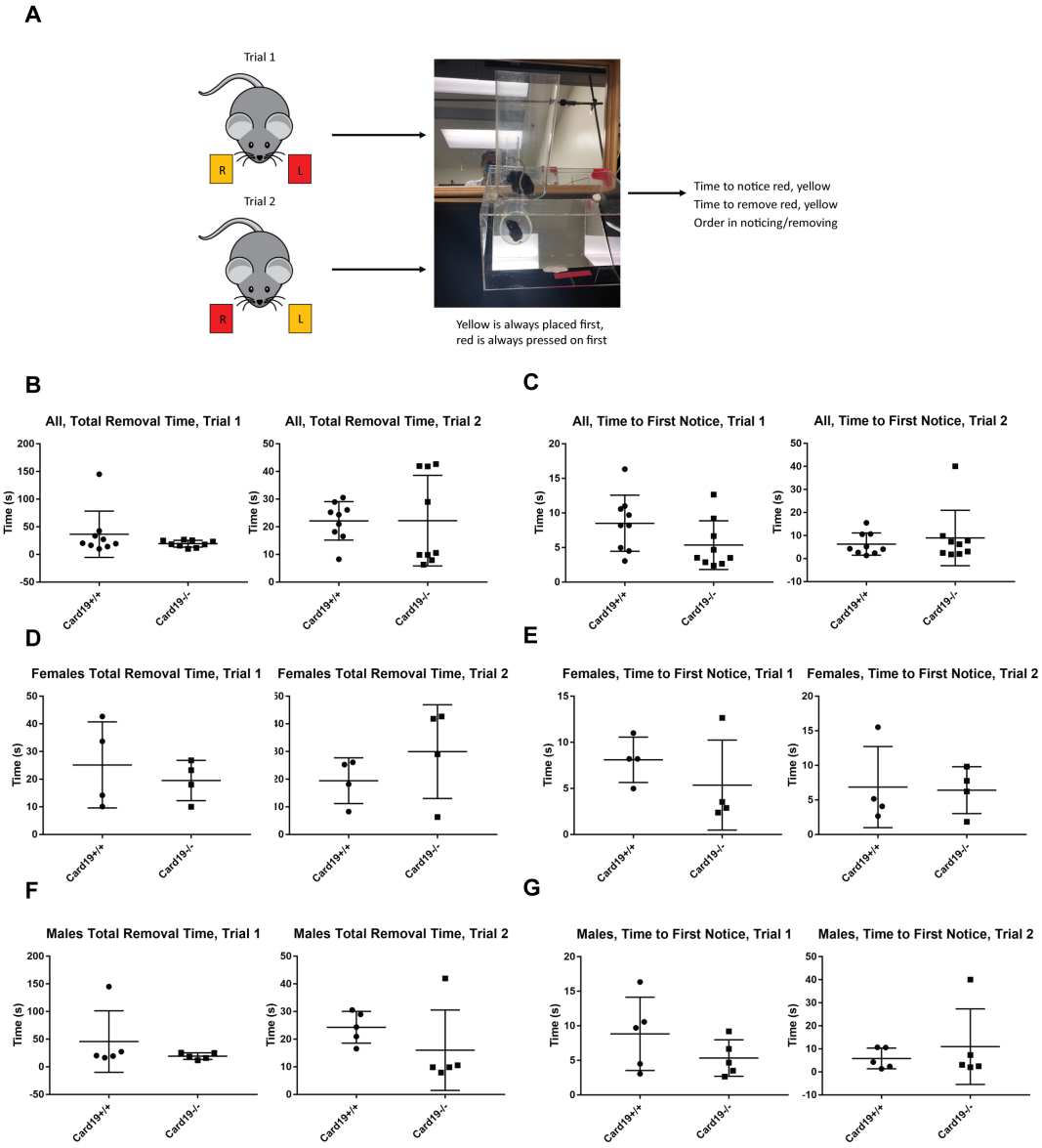

Fig. 20. Tape-test analysis of *Card19* +/+ and *Card19* -/- mice.
(A) In trial 1, yellow tape is placed on the right paw and red tape is placed on the left. In trial 2, the tape placement is reversed. Mice are placed in a clear tube and the time to notice and remove tape is noted. The time to remove both pieces of tape for all mice (B), female mice (D) and male mice (F) was compared between *Card19*+/+ and *Card19* -/- mice. (C), (E), and (G) are the same as (B), (D) and (F), but the time to first notice the tape is compared instead. For all data in Figure 20, unpaired two-way T tests were performed. None of the results were statistically significant.

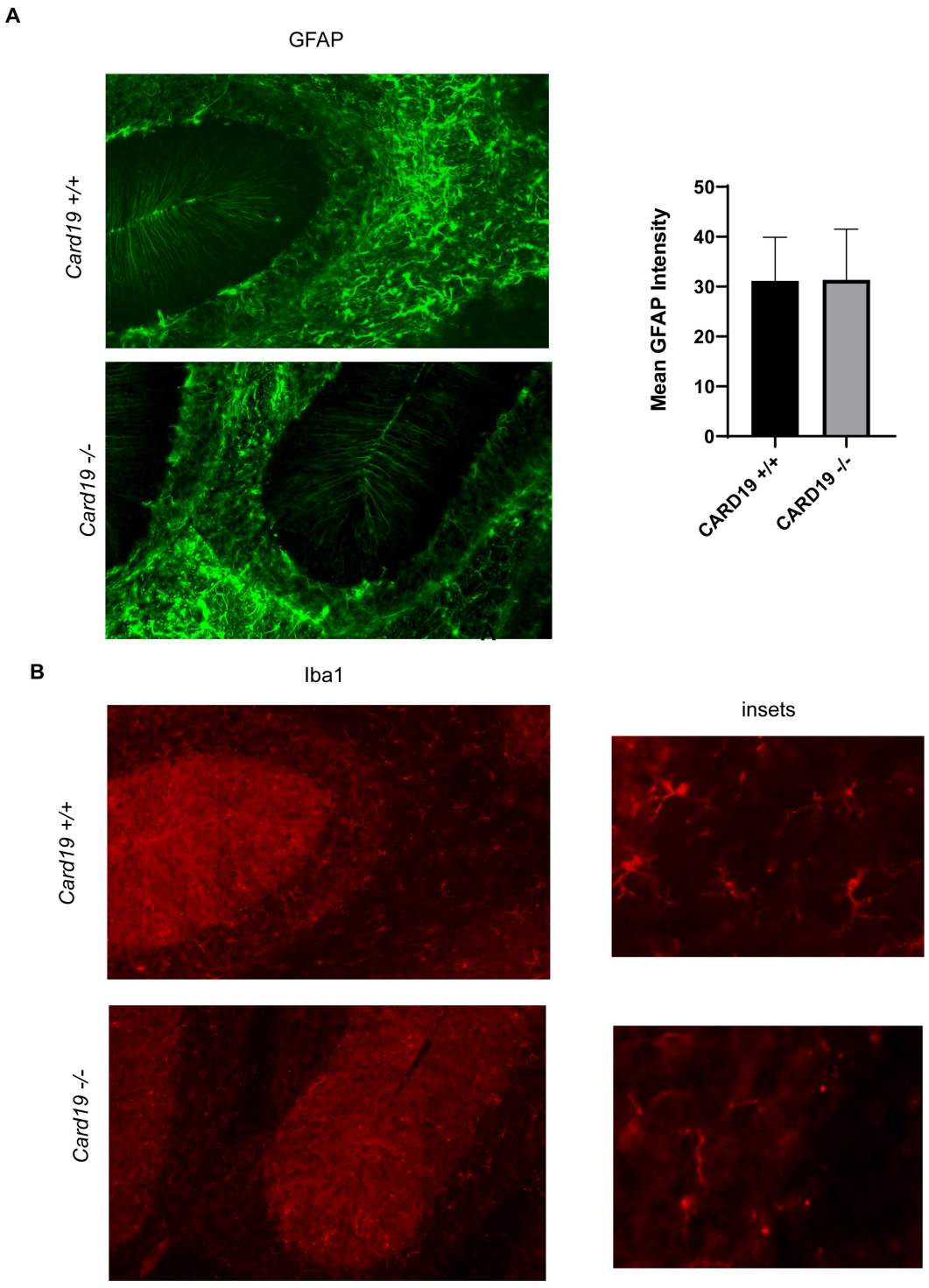

Fig. 21. GFAP (A) and Iba1 (B) staining in sagittal sections of the cerebellum of *Card19* +/+ and *Card19* -/- mice. For (A), GFAP staining intensity was quantified and compared between sections from *Card19* +/+ and *Card19* -/- mice.

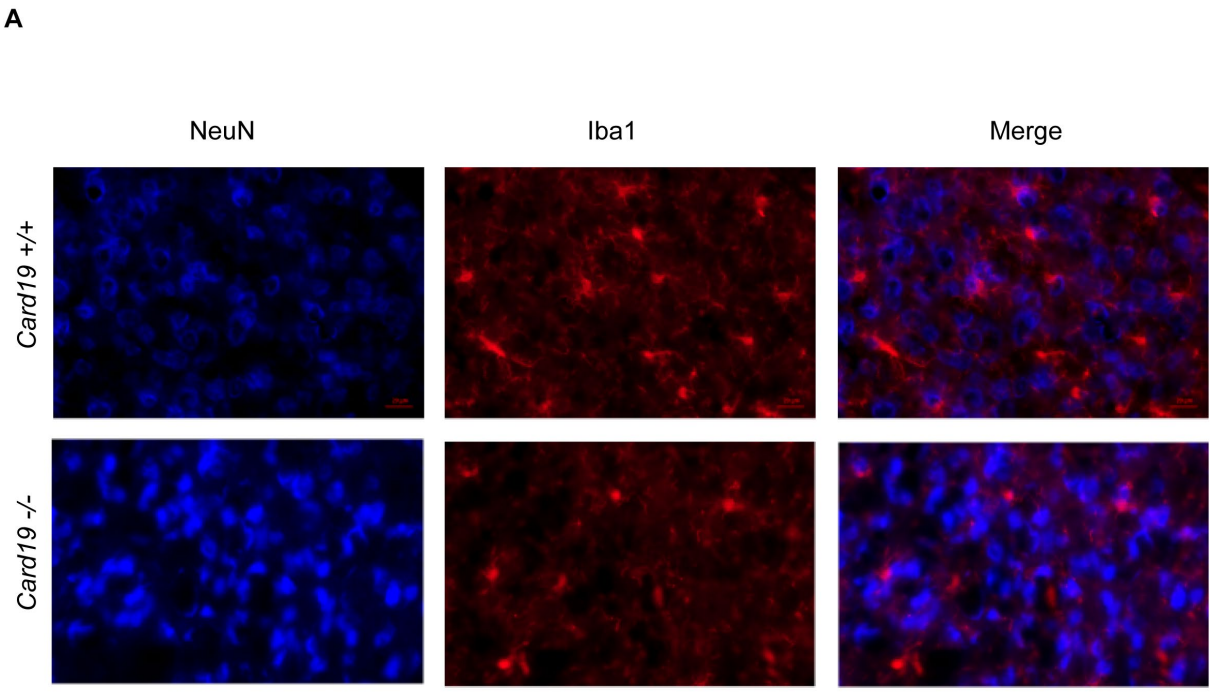

Fig. 22. Iba1 (microglia) and NeuN (neuronal nucleus) staining in coronal sections of the cerebral cortex of *Card19* +/+ and *Card19* -/- mice

REFERENCES

1. Akabane S, Uno M, Tani N, Shimazaki S, Ebara N, et al. 2016. PKA Regulates PINK1 Stability and Parkin Recruitment to Damaged Mitochondria through Phosphorylation of MIC60. *Molecular Cell* 62:371-84
2. Akram M. 2013. Mini-review on Glycolysis and Cancer. *Journal of Cancer Education* 28:454-7
3. Akram M. 2014. Citric Acid Cycle and Role of its Intermediates in Metabolism. *Cell Biochemistry and Biophysics* 68:475-8
4. Allard B, Longhi MS, Robson SC, Stagg J. 2017. The ectonucleotidases CD39 and CD73: Novel checkpoint inhibitor targets. *Immunological reviews* 276:121-44
5. An J, Shi J, He Q, Lui K, Liu Y, et al. 2012. CHCM1/CHCHD6, novel mitochondrial protein linked to regulation of mitofilin and mitochondrial cristae morphology. *J Biol Chem* 287:7411-26
6. Anand R, Kondadi AK, Meisterknecht J, Golombek M, Nortmann O, et al. 2020. MIC26 and MIC27 cooperate to regulate cardiolipin levels and the landscape of OXPHOS complexes. *Life Sci Alliance* 3:e202000711
7. Angajala A, Lim S, Phillips JB, Kim J-H, Yates C, et al. 2018. Diverse Roles of Mitochondria in Immune Responses: Novel Insights Into Immuno-Metabolism. *Frontiers in Immunology* 9:1605
8. Arandjelovic S, Perry JSA, Lucas CD, Penberthy KK, Kim T-H, et al. 2019. A noncanonical role for the engulfment gene ELMO1 in neutrophils that promotes inflammatory arthritis. *Nature Immunology* 20:141-51
9. B. BCaS. 2019.
10. Baechler BL, Bloemberg D, Quadrilatero J. 2019. Mitophagy regulates mitochondrial network signaling, oxidative stress, and apoptosis during myoblast differentiation. *Autophagy* 15:1606-19
11. Bailey SM, Cunningham CC. 2002. Contribution of mitochondria to oxidative stress associated with alcoholic liver disease *Free Radical Biology and Medicine* 32:11-6
12. Barcelos IPd, Troxell RM, Graves JS. 2019. Mitochondrial Dysfunction and Multiple Sclerosis. *Biology (Basel)* 8:37
13. Barnett KC, Ting JPY. 2020. Mitochondrial GSDMD Pores DAMPen Pyroptosis. *Immunity* 52:424-6
14. Baseler WA, Davies LC, Quigley L, Ridnour LA, Weiss JM, et al. 2016. Autocrine IL-10 functions as a rheostat for M1 macrophage glycolytic commitment by tuning nitric oxide production. *Redox Biology* 10:12-23
15. Benincá C, Zanette V, Brischigliaro M, Johnson M, Reyes A, et al. 2021. Mutation in the MICOS subunit gene APOO (MIC26) associated with an X-linked recessive mitochondrial myopathy, lactic acidosis, cognitive impairment and autistic features. *Journal of Medical Genetics* 58:155
16. Bergsbaken T, Fink SL, Cookson BT. 2009. Pyroptosis: host cell death and inflammation. *Nat Rev Microbiol* 7:99-109

17. Bhatia D, Chung K-P, Nakahira K, Patino E, Rice MC, et al. 2019. Mitophagy-dependent macrophage reprogramming protects against kidney fibrosis. *JCI Insight* 4:e132826
18. Bjanes EL. 2019. *The Mitochondrial Protein Card19 Regulates Membrane Integrity And Terminal Lysis Downstream Of Caspase Activation And Gasdermin Cleavage*. University of Pennsylvania Publicly Accessible Penn Dissertations
19. Blum TB, Hahn A, Meier T, Davies KM, Kühlbrandt W. 2019. Dimers of mitochondrial ATP synthase induce membrane curvature and self-assemble into rows. *Proceedings of the National Academy of Sciences* 116:4250
20. Bogenhagen DF, Rousseau D, Burke S. 2008. The Layered Structure of Human Mitochondrial DNA Nucleoids*. *Journal of Biological Chemistry* 283:3665-75
21. Boillée S, Yamanaka K, Lobsiger CS, Copeland NG, Jenkins NA, et al. 2006. Onset and Progression in Inherited ALS Determined by Motor Neurons and Microglia. *Science* 312:1389
22. Bouchier-Hayes L, Martin SJ. 2002. CARD games in apoptosis and immunity. *EMBO reports* 3:616-21
23. Buskiewicz IA, Montgomery T, Yasewicz EC, Huber SA, Murphy MP, et al. 2016. Reactive oxygen species induce virus-independent MAVS oligomerization in systemic lupus erythematosus. *Sci Signal* 9:ra115-ra
24. Cao Y, Rathmell JC, Macintyre AN. 2014. Metabolic Reprogramming towards Aerobic Glycolysis Correlates with Greater Proliferative Ability and Resistance to Metabolic Inhibition in CD8 versus CD4 T Cells. *PLOS ONE* 9:e104104
25. Carneiro FRG, Lepelley A, Seeley JJ, Hayden MS, Ghosh S. 2018. An Essential Role for ECSIT in Mitochondrial Complex I Assembly and Mitophagy in Macrophages. *Cell Rep* 22:2654-66
26. Cham CM, Driessens G, O'Keefe JP, Gajewski TF. 2008. Glucose deprivation inhibits multiple key gene expression events and effector functions in CD8+ T cells. *European Journal of Immunology* 38:2438-50
27. Chance B, Williams GR. 1955. RESPIRATORY ENZYMES IN OXIDATIVE PHOSPHORYLATION: III. THE STEADY STATE. *Journal of Biological Chemistry* 217:409-27
28. Chandra P, He L, Zimmerman M, Yang G, Köster S, et al. 2020. Inhibition of Fatty Acid Oxidation Promotes Macrophage Control of Mycobacterium tuberculosis. *mBio* 11:e01139-20
29. Chang C-H, Curtis Jonathan D, Maggi Leonard B, Faubert B, Villarino Alejandro V, et al. 2013. Posttranscriptional Control of T Cell Effector Function by Aerobic Glycolysis. *Cell* 153:1239-51
30. Chen K-E, Richards AA, Caradoc-Davies TT, Vajjhala PR, Robin G, et al. 2013. The structure of the caspase recruitment domain of BinCARD reveals that all three cysteines can be oxidized. *Acta Crystallographica Section D* 69:774-84
31. Chen Q, Vazquez EJ, Moghaddas S, Hoppel CL, Lesnefsky EJ. 2003. Production of Reactive Oxygen Species by Mitochondria: CENTRAL ROLE OF COMPLEX III. *Journal of Biological Chemistry* 278:36027-31
32. Chinen T, Kannan AK, Levine AG, Fan X, Klein U, et al. 2016. An essential role for the IL-2 receptor in T(reg) cell function. *Nature immunology* 17:1322-33

33. Chou JJ, Matsuo H, Duan H, Wagner G. 1998. Solution Structure of the RAIDD CARD and Model for CARD/CARD Interaction in Caspase-2 and Caspase-9 Recruitment. *Cell* 94:171-80
34. Cogliati S, Enriquez JA, Scorrano L. 2016. Mitochondrial Cristae: Where Beauty Meets Functionality. *Trends in Biochemical Sciences* 41:261-73
35. Crotty S. 2014. T follicular helper cell differentiation, function, and roles in disease. *Immunity* 41:529-42
36. Darshi M, Mendiola VL, Mackey MR, Murphy AN, Koller A, et al. 2011. ChChd3, an inner mitochondrial membrane protein, is essential for maintaining crista integrity and mitochondrial function. *J Biol Chem* 286:2918-32
37. Dehn S, DeBerge M, Yeap X-Y, Yvan-Charvet L, Fang D, et al. 2016. HIF-2α in Resting Macrophages Tempers Mitochondrial Reactive Oxygen Species To Selectively Repress MARCO-Dependent Phagocytosis. *Journal of immunology (Baltimore, Md. : 1950)* 197:3639-49
38. Di Rita A, D'Acunzo P, Simula L, Campello S, Strappazzon F, Cecconi F. 2018. AMBRA1-Mediated Mitophagy Counteracts Oxidative Stress and Apoptosis Induced by Neurotoxicity in Human Neuroblastoma SH-SY5Y Cells. *Frontiers in Cellular Neuroscience* 12:92
39. DiMauro S, Davidzon G. 2005. Mitochondrial DNA and disease. *Annals of Medicine* 37:222-32
40. Doyle AG, Herbein G, Montaner LJ, Minty AJ, Caput D, et al. 1994. Interleukin-13 alters the activation state of murine macrophages in vitro: Comparison with interleukin-4 and interferon-γ. *European Journal of Immunology* 24:1441-5
41. Duong-Ly KC, Kuo Y-M, Johnson MC, Cote JM, Kollman JM, et al. 2018. T cell activation triggers reversible inosine-5′ -monophosphate dehydrogenase assembly. *Journal of Cell Science* 131:jcs223289
42. El Maadidi S, Faletti L, Berg B, Wenzl C, Wieland K, et al. 2014. A Novel Mitochondrial MAVS/Caspase-8 Platform Links RNA Virus–Induced Innate Antiviral Signaling to Bax/Bak-Independent Apoptosis. *The Journal of Immunology* 192:1171
43. Endo Y, Onodera A, Obata-Ninomiya K, Koyama-Nasu R, Asou HK, et al. 2019. ACC1 determines memory potential of individual CD4+ T cells by regulating de novo fatty acid biosynthesis. *Nature Metabolism* 1:261-75
44. Eramo MJ, Lisnyak V, Formosa LE, Ryan MT. 2020. The 'mitochondrial contact site and cristae organising system' (MICOS) in health and human disease. *The Journal of Biochemistry* 167:243-55
45. Eydt K, Davies KM, Behrendt C, Wittig I, Reichert AS. 2017. Cristae architecture is determined by an interplay of the MICOS complex and the F(1)F(O) ATP synthase via Mic27 and Mic10. *Microb Cell* 4:259-72
46. Fagerberg L, Hallström BM, Oksvold P, Kampf C, Djureinovic D, et al. 2014. Analysis of the human tissue-specific expression by genome-wide integration of transcriptomics and antibody-based proteomics. *Mol Cell Proteomics* 13:397-406
47. Federico A, Cardaioli E, Da Pozzo P, Formichi P, Gallus GN, Radi E. 2012. Mitochondria, oxidative stress and neurodegeneration. *Journal of the Neurological Sciences* 322:254-62

48. Feely SME, Laura M, Siskind CE, Sottile S, Davis M, et al. 2011. MFN2 mutations cause severe phenotypes in most patients with CMT2A. *Neurology* 76:1690-6
49. Friedman JR, Mourier A, Yamada J, McCaffery JM, Nunnari J. 2015. MICOS coordinates with respiratory complexes and lipids to establish mitochondrial inner membrane architecture. *eLife* 4:e07739
50. Galván-Peña S, O'Neill LAJ. 2014. Metabolic reprograming in macrophage polarization. *Frontiers in immunology* 5:420-
51. Gao F, Yang J, Wang D, Li C, Fu Y, et al. 2017. Mitophagy in Parkinson's Disease: Pathogenic and Therapeutic Implications. *Front Neurol* 8:527-
52. Giam M, Huang DCS, Bouillet P. 2008. BH3-only proteins and their roles in programmed cell death. *Oncogene* 27:S128-S36
53. Glytsou C, Calvo E, Cogliati S, Mehrotra A, Anastasia I, et al. 2016. Optic Atrophy 1 Is Epistatic to the Core MICOS Component MIC60 in Mitochondrial Cristae Shape Control. *Cell Rep* 17:3024-34
54. Golubovskaya V, Wu L. 2016. Different Subsets of T Cells, Memory, Effector Functions, and CAR-T Immunotherapy. *Cancers (Basel)* 8:36
55. Grasemann C, Devlin MJ, Rzeczkowska PA, Herrmann R, Horsthemke B, et al. 2012. Parental Diabetes: The Akita Mouse as a Model of the Effects of Maternal and Paternal Hyperglycemia in Wildtype Offspring. *PLOS ONE* 7:e50210
56. Grivennikova VG, Vinogradov AD. 2006. Generation of superoxide by the mitochondrial Complex I. *Biochimica et Biophysica Acta (BBA) - Bioenergetics* 1757:553-61
57. Guarani V, McNeill EM, Paulo JA, Huttlin EL, Fröhlich F, et al. 2015. QIL1 is a novel mitochondrial protein required for MICOS complex stability and cristae morphology. *eLife* 4:e06265
58. Han D, Antunes F, Canali R, Rettori D, Cadenas E. 2003. Voltage-dependent Anion Channels Control the Release of the Superoxide Anion from Mitochondria to Cytosol. *Journal of Biological Chemistry* 278:5557-63
59. Han D, Williams E, Cadenas E. 2001. Mitochondrial respiratory chain-dependent generation of superoxide anion and its release into the intermembrane space. *Biochem J* 353:411-6
60. Hansen KG, Herrmann JM. 2019. Transport of Proteins into Mitochondria. *The Protein Journal* 38:330-42
61. Hasson SA, Kane LA, Yamano K, Huang C-H, Sliter DA, et al. 2013. High-content genome-wide RNAi screens identify regulators of parkin upstream of mitophagy. *Nature* 504:291-5
62. Heid ME, Keyel PA, Kamga C, Shiva S, Watkins SC, Salter RD. 2013. Mitochondrial Reactive Oxygen Species Induces NLRP3-Dependent Lysosomal Damage and Inflammasome Activation. *The Journal of Immunology* 191:5230
63. Heindl S, Gesierich B, Benakis C, Llovera G, Duering M, Liesz A. 2018. Automated Morphological Analysis of Microglia After Stroke. *Frontiers in Cellular Neuroscience* 12:106
64. Henchcliffe C, Beal MF. 2008. Mitochondrial biology and oxidative stress in Parkinson disease pathogenesis. *Nature Clinical Practice Neurology* 4:600-9

65. Houten SM, Wanders RJA. 2010. A general introduction to the biochemistry of mitochondrial fatty acid β-oxidation. *J Inherit Metab Dis* 33:469-77
66. Hu S, Du MQ, Park SM, Alcivar A, Qu L, et al. 2006. cIAP2 is a ubiquitin protein ligase for BCL10 and is dysregulated in mucosa-associated lymphoid tissue lymphomas. *J Clin Invest* 116:174-81
67. Hu S, Zhang C, Ni L, Huang C, Chen D, et al. 2020. Stabilization of HIF-1α alleviates osteoarthritis via enhancing mitophagy. *Cell Death & Disease* 11:481
68. Huttlin EL, Bruckner RJ, Navarrete-Perea J, Cannon JR, Baltier K, et al. 2020. Dual Proteome-scale Networks Reveal Cell-specific Remodeling of the Human Interactome. *bioRxiv*:2020.01.19.905109
69. Huttlin EL, Ting L, Bruckner RJ, Gebreab F, Gygi MP, et al. 2015. The BioPlex Network: A Systematic Exploration of the Human Interactome. *Cell* 162:425-40
70. Huynen MA, Mühlmeister M, Gotthardt K, Guerrero-Castillo S, Brandt U. 2016. Evolution and structural organization of the mitochondrial contact site (MICOS) complex and the mitochondrial intermembrane space bridging (MIB) complex. *Biochimica et Biophysica Acta (BBA) - Molecular Cell Research* 1863:91-101
71. Hwang MS, Schwall CT, Pazarentzos E, Datler C, Alder NN, Grimm S. 2014. Mitochondrial Ca(2+) influx targets cardiolipin to disintegrate respiratory chain complex II for cell death induction. *Cell Death Differ* 21:1733-45
72. Ibitokou SA, Dillon BE, Sinha M, Szczesny B, Delgadillo A, et al. 2018. Early Inhibition of Fatty Acid Synthesis Reduces Generation of Memory Precursor Effector T Cells in Chronic Infection. *The Journal of Immunology* 200:643
73. Italiani P, Boraschi D. 2014. From Monocytes to M1/M2 Macrophages: Phenotypical vs. Functional Differentiation. *Frontiers in Immunology* 5:514
74. Ito D, Imai Y, Ohsawa K, Nakajima K, Fukuuchi Y, Kohsaka S. 1998. Microglia-specific localisation of a novel calcium binding protein, Iba1. *Molecular Brain Research* 57:1-9
75. Jain N, Nguyen H, Chambers C, Kang J. 2010. Dual function of CTLA-4 in regulatory T cells and conventional T cells to prevent multiorgan autoimmunity. *Proceedings of the National Academy of Sciences* 107:1524
76. Jans DC, Wurm CA, Riedel D, Wenzel D, Stagge F, et al. 2013. STED super-resolution microscopy reveals an array of MINOS clusters along human mitochondria. *Proceedings of the National Academy of Sciences* 110:8936
77. Jiang C, Zhou Z, Quan Y, Zhang S, Wang T, et al. 2016. CARMA3 Is a Host Factor Regulating the Balance of Inflammatory and Antiviral Responses against Viral Infection. *Cell Rep* 14:2389-401
78. Jiko C, Davies KM, Shinzawa-Itoh K, Tani K, Maeda S, et al. 2015. Bovine F1Fo ATP synthase monomers bend the lipid bilayer in 2D membrane crystals. *eLife* 4:e06119
79. Jin SM, Lazarou M, Wang C, Kane LA, Narendra DP, Youle RJ. 2010. Mitochondrial membrane potential regulates PINK1 import and proteolytic destabilization by PARL. *J Cell Biol* 191:933-42
80. John GB, Shang Y, Li L, Renken C, Mannella CA, et al. 2005. The Mitochondrial Inner Membrane Protein Mitofilin Controls Cristae Morphology. *Molecular Biology of the Cell* 16:1543-54

81. Kabat AM, Pearce EJ. 2017. Inflammation by way of macrophage metabolism. *Science* 356:488
82. Kaech SM, Wherry EJ, Ahmed R. 2002. Effector and memory T-cell differentiation: implications for vaccine development. *Nature Reviews Immunology* 2:251-62
83. Kim HJ, Cho MH, Shim WH, Kim JK, Jeon EY, et al. 2017. Deficient autophagy in microglia impairs synaptic pruning and causes social behavioral defects. *Molecular Psychiatry* 22:1576-84
84. Kingeter LM, Paul S, Maynard SK, Cartwright NG, Schaefer BC. 2010. Cutting edge: TCR ligation triggers digital activation of NF-kappaB. *J Immunol* 185:4520-4
85. Koob S, Barrera M, Anand R, Reichert AS. 2015. The non-glycosylated isoform of MIC26 is a constituent of the mammalian MICOS complex and promotes formation of crista junctions. *Biochimica et Biophysica Acta (BBA) - Molecular Cell Research* 1853:1551-63
86. Krauss S. 2001. Mitochondria: Structure and Role in Respiration. Number of.
87. Kühlbrandt W. 2015. Structure and function of mitochondrial membrane protein complexes. *BMC Biology* 13:89
88. Langel FD, Jain NA, Rossman JS, Kingeter LM, Kashyap AK, Schaefer BC. 2008. Multiple protein domains mediate interaction between Bcl10 and MALT1. *J Biol Chem* 283:32419-31
89. Larsen SE, Bilenkin A, Tarasenko TN, Arjunaraja S, Stinson JR, et al. 2017. Sensitivity to Restimulation-Induced Cell Death Is Linked to Glycolytic Metabolism in Human T Cells. *The Journal of Immunology* 198:147
90. Larson-Casey JL, Deshane JS, Ryan AJ, Thannickal VJ, Carter AB. 2016. Macrophage Akt1 Kinase-Mediated Mitophagy Modulates Apoptosis Resistance and Pulmonary Fibrosis. *Immunity* 44:582-96
91. Lattin JE, Schroder K, Su AI, Walker JR, Zhang J, et al. 2008. Expression analysis of G Protein-Coupled Receptors in mouse macrophages. *Immunome Res* 4:5-
92. Lecours C, Bordeleau M, Cantin L, Parent M, Paolo TD, Tremblay M-È. 2018. Microglial Implication in Parkinson's Disease: Loss of Beneficial Physiological Roles or Gain of Inflammatory Functions? *Frontiers in Cellular Neuroscience* 12:282
93. Lee FHF, Zhang H, Jiang A, Zai CC, Liu F. 2018. Specific Alterations in Astrocyte Properties via the GluA2-GAPDH Complex Associated with Multiple Sclerosis. *Scientific Reports* 8:12856
94. Lee RG, Sedghi M, Salari M, Shearwood A-MJ, Stentenbach M, et al. 2018. Early-onset Parkinson disease caused by a mutation in CHCHD2 and mitochondrial dysfunction. *Neurology Genetics* 4:e276
95. Lee S, Min K-T. 2018. The Interface Between ER and Mitochondria: Molecular Compositions and Functions. *Mol Cells* 41:1000-7
96. Lei Y, Moore CB, Liesman RM, O'Connor BP, Bergstralh DT, et al. 2009. MAVS-mediated apoptosis and its inhibition by viral proteins. *PloS one* 4:e5466-e

97. Lenaz G, Bovina C, D'Aurelio M, Fato R, Formiggini G, et al. 2002. Role of Mitochondria in Oxidative Stress and Aging. *Annals of the New York Academy of Sciences* 959:199-213
98. Li J, Lu J, Mi Y, Shi Z, Chen C, et al. 2014. Voltage-dependent anion channels (VDACs) promote mitophagy to protect neuron from death in an early brain injury following a subarachnoid hemorrhage in rats. *Brain Research* 1573:74-83
99. Li M, Zhong Z, Zhu J, Xiang D, Dai N, et al. 2010. Identification and characterization of mitochondrial targeting sequence of human apurinic/apyrimidinic endonuclease 1. *J Biol Chem* 285:14871-81
100. Li N, Katz S, Dutta B, Benet ZL, Sun J, Fraser IDC. 2017. Genome-wide siRNA screen of genes regulating the LPS-induced NF-κB and TNF-α responses in mouse macrophages. *Sci Data* 4:170008-
101. Li S, Wu Z, Li Y, Tantray I, De Stefani D, et al. 2020. Altered MICOS Morphology and Mitochondrial Ion Homeostasis Contribute to Poly(GR) Toxicity Associated with C9-ALS/FTD. *Cell Rep* 32:107989
102. Li Z, Peng Y, Hufnagel RB, Hu Y-C, Zhao C, et al. 2017. Loss of SLC25A46 causes neurodegeneration by affecting mitochondrial dynamics and energy production in mice. *Hum Mol Genet* 26:3776-91
103. Lin R, Zhang H, Yuan Y, He Q, Zhou J, et al. 2020. Fatty Acid Oxidation Controls CD8+ Tissue-Resident Memory T-cell Survival in Gastric Adenocarcinoma. *Cancer Immunology Research* 8:479
104. Liu L, Lu Y, Martinez J, Bi Y, Lian G, et al. 2016. Proinflammatory signal suppresses proliferation and shifts macrophage metabolism from Myc-dependent to HIF1α-dependent. *Proc Natl Acad Sci U S A* 113:1564-9
105. Livingston MJ, Wang J, Zhou J, Wu G, Ganley IG, et al. 2019. Clearance of damaged mitochondria via mitophagy is important to the protective effect of ischemic preconditioning in kidneys. *Autophagy* 15:2142-62
106. Lobry C, Lopez T, Israel A, Weil R. 2007. Negative feedback loop in T cell activation through IkappaB kinase-induced phosphorylation and degradation of Bcl10. *PNAS* 104:908-13
107. López-Armada MJ, Riveiro-Naveira RR, Vaamonde-García C, Valcárcel-Ares MN. 2013. Mitochondrial dysfunction and the inflammatory response. *Mitochondrion* 13:106-18
108. Madungwe NB, Feng Y, Lie M, Tombo N, Liu L, et al. 2018. Mitochondrial inner membrane protein (mitofilin) knockdown induces cell death by apoptosis via an AIF-PARP-dependent mechanism and cell cycle arrest. *American Journal of Physiology-Cell Physiology* 315:C28-C43
109. Malpartida AB, Williamson M, Narendra DP, Wade-Martins R, Ryan BJ. Mitochondrial Dysfunction and Mitophagy in Parkinson's Disease: From Mechanism to Therapy. *Trends in Biochemical Sciences*
110. Man SM, Karki R, Kanneganti T-D. 2017. Molecular mechanisms and functions of pyroptosis, inflammatory caspases and inflammasomes in infectious diseases. *Immunological reviews* 277:61-75
111. Mancini NL, Goudie L, Xu W, Sabouny R, Rajeev S, et al. 2020. Perturbed Mitochondrial Dynamics Is a Novel Feature of Colitis That Can Be Targeted to

Lessen Disease. *Cellular and Molecular Gastroenterology and Hepatology* 10:287-307
112. Mathupala SP, Pedersen PL. 2010. Voltage dependent anion channel-1 (VDAC-1) as an anti-cancer target. *Cancer Biol Ther* 9:1053-6
113. Mosser DM, Edwards JP. 2008. Exploring the full spectrum of macrophage activation. *Nature Reviews Immunology* 8:958-69
114. Muller F. 2000. The nature and mechanism of superoxide production by the electron transport chain: Its relevance to aging. *J Am Aging Assoc* 23:227-53
115. Muller FL, Liu Y, Van Remmen H. 2004. Complex III Releases Superoxide to Both Sides of the Inner Mitochondrial Membrane. *Journal of Biological Chemistry* 279:49064-73
116. Namgaladze D, Brüne B. 2014. Fatty acid oxidation is dispensable for human macrophage IL-4-induced polarization. *Biochimica et Biophysica Acta (BBA) - Molecular and Cell Biology of Lipids* 1841:1329-35
117. Nathan CF, Murray HW, Wiebe ME, Rubin BY. 1983. Identification of interferon-gamma as the lymphokine that activates human macrophage oxidative metabolism and antimicrobial activity. *Journal of Experimental Medicine* 158:670-89
118. Nobre L, Wise D, Ron D, Volmer R. 2015. Modulation of Innate Immune Signalling by Lipid-Mediated MAVS Transmembrane Domain Oligomerization. *PLOS ONE* 10:e0136883
119. Novak EA, Mollen KP. 2015. Mitochondrial dysfunction in inflammatory bowel disease. *Frontiers in Cell and Developmental Biology* 3:62
120. O'Neill LAJ, Pearce EJ. 2015. Immunometabolism governs dendritic cell and macrophage function. *Journal of Experimental Medicine* 213:15-23
121. Ogando J, Sáez ME, Santos J, Nuevo-Tapioles C, Gut M, et al. 2019. PD-1 signaling affects cristae morphology and leads to mitochondrial dysfunction in human CD8+ T lymphocytes. *Journal for ImmunoTherapy of Cancer* 7:151
122. Pace JL, Russell SW, Schreiber RD, Altman A, Katz DH. 1983. Macrophage activation: priming activity from a T-cell hybridoma is attributable to interferon-gamma. *Proceedings of the National Academy of Sciences* 80:3782
123. Palmieri EM, Gonzalez-Cotto M, Baseler WA, Davies LC, Ghesquière B, et al. 2020. Nitric oxide orchestrates metabolic rewiring in M1 macrophages by targeting aconitase 2 and pyruvate dehydrogenase. *Nature Communications* 11:698
124. Palsson-McDermott EM, O'Neill LAJ. 2013. The Warburg effect then and now: From cancer to inflammatory diseases. *BioEssays* 35:965-73
125. Pang L, Liu K, Liu D, Lv F, Zang Y, et al. 2018. Differential effects of reticulophagy and mitophagy on nonalcoholic fatty liver disease. *Cell Death & Disease* 9:90
126. Park HH, Lo Y-C, Lin S-C, Wang L, Yang JK, Wu H. 2007. The Death Domain Superfamily in Intracellular Signaling of Apoptosis and Inflammation. *Annual Review of Immunology* 25:561-86
127. Patergnani S, Castellazzi M, Bonora M, Marchi S, Casetta I, et al. 2018. Autophagy and mitophagy elements are increased in body fluids of multiple

sclerosis-affected individuals. *Journal of Neurology, Neurosurgery & Psychiatry* 89:439
128. Paul S, Kashyap Anuj K, Jia W, He Y-W, Schaefer Brian C. 2012. Selective Autophagy of the Adaptor Protein Bcl10 Modulates T Cell Receptor Activation of NF-κB. *Immunity* 36:947-58
129. Paul S, Schaefer BC. 2015. Visualizing TCR-Induced POLKADOTS Formation and NF-κB Activation in the D10 T-Cell Clone and Mouse Primary Effector T Cells. In *NF-kappa B: Methods and Protocols*, ed. MJ May:219-38. New York, NY: Springer New York. Number of 219-38 pp.
130. Pearce EL, Walsh MC, Cejas PJ, Harms GM, Shen H, et al. 2009. Enhancing CD8 T-cell memory by modulating fatty acid metabolism. *Nature* 460:103-7
131. Pinegin B, Vorobjeva N, Pashenkov M, Chernyak B. 2018. The role of mitochondrial ROS in antibacterial immunity. *Journal of Cellular Physiology* 233:3745-54
132. Qiao A, Wang K, Yuan Y, Guan Y, Ren X, et al. 2016. Sirt3-mediated mitophagy protects tumor cells against apoptosis under hypoxia. *Oncotarget* 7:43390-400
133. Rampelt H, Wollweber F, Gerke C, de Boer R, van der Klei IJ, et al. 2018. Assembly of the Mitochondrial Cristae Organizer Mic10 Is Regulated by Mic26–Mic27 Antagonism and Cardiolipin. *Journal of Molecular Biology* 430:1883-90
134. Raud B, McGuire PJ, Jones RG, Sparwasser T, Berod L. 2018. Fatty acid metabolism in CD8(+) T cell memory: Challenging current concepts. *Immunological reviews* 283:213-31
135. Raud B, Roy DG, Divakaruni AS, Tarasenko TN, Franke R, et al. 2018. Etomoxir Actions on Regulatory and Memory T Cells Are Independent of Cpt1a-Mediated Fatty Acid Oxidation. *Cell Metabolism* 28:504-15.e7
136. Ray K. 2020. Mitochondrial dysfunction in Crohn's disease. *Nature Reviews Gastroenterology & Hepatology* 17:260-
137. Refolo G, Vescovo T, Piacentini M, Fimia GM, Ciccosanti F. 2020. Mitochondrial Interactome: A Focus on Antiviral Signaling Pathways. *Frontiers in Cell and Developmental Biology* 8:8
138. Rios KE, Kashyap AK, Maynard SK, Washington M, Paul S, Schaefer BC. 2020. CARD19, the protein formerly known as BinCARD, is a mitochondrial protein that does not regulate Bcl10-dependent NF-κB activation after TCR engagement. *Cellular Immunology* 356:104179
139. Rocha S, Freitas A, Guimaraes SC, Vitorino R, Aroso M, Gomez-Lazaro M. 2017. Biological Implications of Differential Expression of Mitochondrial-Shaping Proteins in Parkinson's Disease. *Antioxidants (Basel)* 7:1
140. Rogers C, Erkes DA, Nardone A, Aplin AE, Fernandes-Alnemri T, Alnemri ES. 2019. Gasdermin pores permeabilize mitochondria to augment caspase-3 activation during apoptosis and inflammasome activation. *Nature Communications* 10:1689
141. Romano M, Fanelli G, Albany CJ, Giganti G, Lombardi G. 2019. Past, Present, and Future of Regulatory T Cell Therapy in Transplantation and Autoimmunity. *Frontiers in Immunology* 10:43

142. Rossignol R, Gilkerson R, Aggeler R, Yamagata K, Remington SJ, Capaldi RA. 2004. Energy Substrate Modulates Mitochondrial Structure and Oxidative Capacity in Cancer Cells. *Cancer Research* 64:985
143. Sadeghian M, Mastrolia V, Rezaei Haddad A, Mosley A, Mullali G, et al. 2016. Mitochondrial dysfunction is an important cause of neurological deficits in an inflammatory model of multiple sclerosis. *Scientific Reports* 6:33249
144. Sakowska P, Jans DC, Mohanraj K, Riedel D, Jakobs S, Chacinska A. 2015. The Oxidation Status of Mic19 Regulates MICOS Assembly. *Mol Cell Biol* 35:4222-37
145. Sansonetti PJ, Phalipon A, Arondel J, Thirumalai K, Banerjee S, et al. 2000. Caspase-1 Activation of IL-1b and IL-18 Are Essential for Shigella flexneri Induced Inflammation. *Immunity* 12:581-90
146. Sarkar S, Malovic E, Harishchandra DS, Ghaisas S, Panicker N, et al. 2017. Mitochondrial impairment in microglia amplifies NLRP3 inflammasome proinflammatory signaling in cell culture and animal models of Parkinson's disease. *NPJ Parkinsons Dis* 3:30-
147. Scharschmidt E, Wegener E, Heissmeyer V, Rao A, Krappmann D. 2004. Degradation of Bcl10 induced by Tcell activation negatively regulates NF-kappaB signaling. *Mol Cell Biol* 24:3860-73
148. Schmidt O, Pfanner N, Meisinger C. 2010. Mitochondrial protein import: from proteomics to functional mechanisms. *Nature Reviews Molecular Cell Biology* 11:655-67
149. Schweppe DK, Huttlin EL, Harper JW, Gygi SP. 2018. BioPlex Display: An Interactive Suite for Large-Scale AP–MS Protein–Protein Interaction Data. *Journal of Proteome Research* 17:722-6
150. Sellge G, Magalhaes JG, Konradt C, Fritz JH, Salgado-Pabon W, et al. 2010. Th17 Cells Are the Dominant T Cell Subtype Primed by Shigella flexneri Mediating Protective Immunity. *The Journal of Immunology* 184:2076
151. Sena LA, Li S, Jairaman A, Prakriya M, Ezponda T, et al. 2013. Mitochondria are required for antigen-specific T cell activation through reactive oxygen species signaling. *Immunity* 38:225-36
152. Shen Y, McMackin MZ, Shan Y, Raetz A, David S, Cortopassi G. 2016. Frataxin Deficiency Promotes Excess Microglial DNA Damage and Inflammation that Is Rescued by PJ34. *PLOS ONE* 11:e0151026
153. Spangenberg E, Severson PL, Hohsfield LA, Crapser J, Zhang J, et al. 2019. Sustained microglial depletion with CSF1R inhibitor impairs parenchymal plaque development in an Alzheimer's disease model. *Nature Communications* 10:3758
154. Spangenberg EE, Lee RJ, Najafi AR, Rice RA, Elmore MRP, et al. 2016. Eliminating microglia in Alzheimer's mice prevents neuronal loss without modulating amyloid-β pathology. *Brain* 139:1265-81
155. St-Pierre J, Buckingham JA, Roebuck SJ, Brand MD. 2002. Topology of Superoxide Production from Different Sites in the Mitochondrial Electron Transport Chain*. *Journal of Biological Chemistry* 277:44784-90
156. St. Paul M, Ohashi PS. 2020. The Roles of CD8+ T Cell Subsets in Antitumor Immunity. *Trends in Cell Biology* 30:695-704

157. Stein M, Keshav S, Harris N, Gordon S. 1992. Interleukin 4 potently enhances murine macrophage mannose receptor activity: a marker of alternative immunologic macrophage activation. *Journal of Experimental Medicine* 176:287-92
158. Stephan T, Brüser C, Deckers M, Steyer AM, Balzarotti F, et al. 2020. MICOS assembly controls mitochondrial inner membrane remodeling and crista junction redistribution to mediate cristae formation. *The EMBO Journal* 39:e104105
159. Stranks AJ, Hansen AL, Panse I, Mortensen M, Ferguson DJP, et al. 2015. Autophagy Controls Acquisition of Aging Features in Macrophages. *Journal of Innate Immunity* 7:375-91
160. Strasser A, O'Connor L, Dixit VM. 2000. Apoptosis Signaling. *Annual Review of Biochemistry* 69:217-45
161. Su AI, Wiltshire T, Batalov S, Lapp H, Ching KA, et al. 2004. A gene atlas of the mouse and human protein-encoding transcriptomes. *Proc Natl Acad Sci U S A* 101:6062-7
162. Su S-H, Wu Y-F, Wang D-P, Hai J. 2018. Inhibition of excessive autophagy and mitophagy mediates neuroprotective effects of URB597 against chronic cerebral hypoperfusion. *Cell Death & Disease* 9:733
163. Sun J, Katz S, Dutta B, Wang Z, Fraser IDC. 2017. Genome-wide siRNA screen of genes regulating the LPS-induced TNF-α response in human macrophages. *Sci Data* 4:170007-
164. Sun L, Deng L, Ea CK, Xia ZP, Chen ZJ. 2004. The TRAF6 ubiquitin ligase and TAK1 kinase mediate IKK activation by BCL10 and MALT1 in T lymphocytes. *Mol Cell* 14:289-301
165. Sun L, Hao Y, An R, Li H, Xi C, Shen G. 2014. Overexpression of Rcan1-1L inhibits hypoxia-induced cell apoptosis through induction of mitophagy. *Mol Cells* 37:785-94
166. Suzuki H, Kameyama T, Takaoka A. 2019. BinCARD2 as a positive regulator of interferon response in innate immunity. *Biochemical and Biophysical Research Communications* 511:287-93
167. Tanaka A, To J, O'Brien B, Donnelly S, Lund M. 2017. Selection of reliable reference genes for the normalisation of gene expression levels following time course LPS stimulation of murine bone marrow derived macrophages. *BMC Immunol* 18:43-
168. Tang J, Zhang K, Dong J, Yan C, Hu C, et al. 2020. Sam50–Mic19–Mic60 axis determines mitochondrial cristae architecture by mediating mitochondrial outer and inner membrane contact. *Cell Death & Differentiation* 27:146-60
169. Tannahill GM, Curtis AM, Adamik J, Palsson-McDermott EM, McGettrick AF, et al. 2013. Succinate is an inflammatory signal that induces IL-1β through HIF-1α. *Nature* 496:238-42
170. Telford BJ, Chen A, Beetham H, Frick J, Brew TP, et al. 2015. Synthetic Lethal Screens Identify Vulnerabilities in GPCR Signaling and Cytoskeletal Organization in E-Cadherin–Deficient Cells. *Molecular Cancer Therapeutics* 14:1213

171. Terzenidou ME, Segklia A, Kano T, Papastefanaki F, Karakostas A, et al. 2017. Novel insights into SLC25A46-related pathologies in a genetic mouse model. *PLoS Genet* 13:e1006656-e
172. Thome M, Charton JE, Pelzer C, Hailfinger S. 2010. Antigen receptor signaling to NF-kappaB via CARMA1, BCL10, and MALT1. *Cold Spring Harb Perspect Biol* 2:a003004
173. Togashi Y, Shirakawa J, Okuyama T, Yamazaki S, Kyohara M, et al. 2016. Evaluation of the appropriateness of using glucometers for measuring the blood glucose levels in mice. *Scientific Reports* 6:25465
174. Truscott KN, Brandner K, Pfanner N. 2003. Mechanisms of Protein Import into Mitochondria. *Current Biology* 13:R326-R37
175. Tsai P-I, Lin C-H, Hsieh C-H, Papakyrikos AM, Kim MJ, et al. 2018. PINK1 Phosphorylates MIC60/Mitofilin to Control Structural Plasticity of Mitochondrial Crista Junctions. *Molecular Cell* 69:744-56.e6
176. Uhlén M, Fagerberg L, Hallström BM, Lindskog C, Oksvold P, et al. 2015. Tissue-based map of the human proteome. *Science* 347:1260419
177. Utsumi T, Matsuzaki K, Kiwado A, Tanikawa A, Kikkawa Y, et al. 2018. Identification and characterization of protein N-myristoylation occurring on four human mitochondrial proteins, SAMM50, TOMM40, MIC19, and MIC25. *PLOS ONE* 13:e0206355
178. Valvona CJ, Fillmore HL, Nunn PB, Pilkington GJ. 2016. The Regulation and Function of Lactate Dehydrogenase A: Therapeutic Potential in Brain Tumor. *Brain Pathology* 26:3-17
179. Van den Bossche J, Baardman J, Otto Natasja A, van der Velden S, Neele Annette E, et al. 2016. Mitochondrial Dysfunction Prevents Repolarization of Inflammatory Macrophages. *Cell Rep* 17:684-96
180. Vander Heiden MG, Cantley LC, Thompson CB. 2009. Understanding the Warburg Effect: The Metabolic Requirements of Cell Proliferation. *Science* 324:1029
181. Vats D, Mukundan L, Odegaard JI, Zhang L, Smith KL, et al. 2006. Oxidative metabolism and PGC-1beta attenuate macrophage-mediated inflammation. *Cell metabolism* 4:13-24
182. von der Malsburg K, Müller Judith M, Bohnert M, Oeljeklaus S, Kwiatkowska P, et al. 2011. Dual Role of Mitofilin in Mitochondrial Membrane Organization and Protein Biogenesis. *Developmental Cell* 21:694-707
183. Wang C, Youle RJ. 2009. The role of mitochondria in apoptosis. *Annu Rev Genet* 43:95-118
184. Wang J, Wang J, Wang J, Yang B, Weng Q, He Q. 2019. Targeting Microglia and Macrophages: A Potential Treatment Strategy for Multiple Sclerosis. *Frontiers in Pharmacology* 10:286
185. Wang S, Wang L, Qin X, Turdi S, Sun D, et al. 2020. ALDH2 contributes to melatonin-induced protection against APP/PS1 mutation-prompted cardiac anomalies through cGAS-STING-TBK1-mediated regulation of mitophagy. *Signal Transduction and Targeted Therapy* 5:119

186. Wang X, Wang W, Li L, Perry G, Lee H-g, Zhu X. 2014. Oxidative stress and mitochondrial dysfunction in Alzheimer's disease. *Biochimica et Biophysica Acta (BBA) - Molecular Basis of Disease* 1842:1240-7
187. Wang Y, Mao X, Chen H, Feng J, Yan M, et al. 2019. Dexmedetomidine alleviates LPS-induced apoptosis and inflammation in macrophages by eliminating damaged mitochondria via PINK1 mediated mitophagy. *International Immunopharmacology* 73:471-81
188. Wang Y, Tang C, Cai J, Chen G, Zhang D, et al. 2018. PINK1/Parkin-mediated mitophagy is activated in cisplatin nephrotoxicity to protect against kidney injury. *Cell Death & Disease* 9:1113
189. Warburg O. 1956. On the Origin of Cancer Cells. *Science* 123:309-14
190. Weber TA, Koob S, Heide H, Wittig I, Head B, et al. 2013. APOOL Is a Cardiolipin-Binding Constituent of the Mitofilin/MINOS Protein Complex Determining Cristae Morphology in Mammalian Mitochondria. *PLOS ONE* 8:e63683
191. Wegener E, Oeckinghaus A, Papadopoulou N, Lavitas L, Schmidt-Supprian M, et al. 2006. Essential role for IkappaB kinase beta in remodeling Carma1-Bcl10-Malt1 complexes upon T cell activation. *Mol Cell* 23:13-23
192. West AP, Brodsky IE, Rahner C, Woo DK, Erdjument-Bromage H, et al. 2011. TLR signalling augments macrophage bactericidal activity through mitochondrial ROS. *Nature* 472:476-80
193. Williams JA, Ni H-M, Ding Y, Ding W-X. 2015. Parkin regulates mitophagy and mitochondrial function to protect against alcohol-induced liver injury and steatosis in mice. *American Journal of Physiology-Gastrointestinal and Liver Physiology* 309:G324-G40
194. Williamson JR, Cooper RH. 1980. Regulation of the citric acid cycle in mammalian systems. *FEBS Letters* 117:K73-K85
195. Wolstenholme DR. 1992. Animal Mitochondrial DNA: Structure and Evolution. In *International Review of Cytology*, ed. DR Wolstenholme, KW Jeon, 141:173-216: Academic Press. Number of 173-216 pp.
196. Woo H-N, Hong G-S, Jun J-I, Cho D-H, Hyun-WooChoi, et al. 2004. Inhibition of Bcl10-mediated activation of NF-κB by BinCARD, a Bcl10-interacting CARD protein. *FEBS Letters* 578:239-44
197. Wu B, Hur S. 2015. How RIG-I like receptors activate MAVS. *Curr Opin Virol* 12:91-8
198. Wu C, Jin X, Tsueng G, Afrasiabi C, Su AI. 2016. BioGPS: building your own mash-up of gene annotations and expression profiles. *Nucleic Acids Research* 44:D313-D6
199. Wu W, Xu H, Wang Z, Mao Y, Yuan L, et al. 2015. PINK1-Parkin-Mediated Mitophagy Protects Mitochondrial Integrity and Prevents Metabolic Stress-Induced Endothelial Injury. *PLOS ONE* 10:e0132499
200. Xie J, Marusich MF, Souda P, Whitelegge J, Capaldi RA. 2007. The mitochondrial inner membrane protein Mitofilin exists as a complex with SAM50, metaxins 1 and 2, coiled-coil-helix coiled-coil-helix domain-containing protein 3 and 6 and DnaJC11. *FEBS Letters* 581:3545-9

201. Xie L, Huang W, Fang Z, Ding F, Zou F, et al. 2019. CircERCC2 ameliorated intervertebral disc degeneration by regulating mitophagy and apoptosis through miR-182-5p/SIRT1 axis. *Cell Death & Disease* 10:751
202. Xue L, Morris SW, Orihuela C, Tuomanen E, Cui X, et al. 2003. Defective development and function of Bcl10-deficient follicular, marginal zone and B1 B cells. *Nat Immunol* 4:857-65
203. Young K, Morrison H. 2018. Quantifying Microglia Morphology from Photomicrographs of Immunohistochemistry Prepared Tissue Using ImageJ. *J Vis Exp*:57648
204. Zeharia A, Friedman JR, Tobar A, Saada A, Konen O, et al. 2016. Mitochondrial hepato-encephalopathy due to deficiency of QIL1/MIC13 (C19orf70), a MICOS complex subunit. *Eur J Hum Genet* 24:1778-82
205. Zerbes RM, Bohnert M, Stroud DA, von der Malsburg K, Kram A, et al. 2012. Role of MINOS in Mitochondrial Membrane Architecture: Cristae Morphology and Outer Membrane Interactions Differentially Depend on Mitofilin Domains. *Journal of Molecular Biology* 422:183-91
206. Zhang Y, Chen K, Sloan SA, Bennett ML, Scholze AR, et al. 2014. An RNA-Sequencing Transcriptome and Splicing Database of Glia, Neurons, and Vascular Cells of the Cerebral Cortex. *The Journal of Neuroscience* 34:11929
207. Zhao C, He R, Shen M, Zhu F, Wang M, et al. 2019. PINK1/Parkin-Mediated Mitophagy Regulation by Reactive Oxygen Species Alleviates Rocaglamide A-Induced Apoptosis in Pancreatic Cancer Cells. *Frontiers in Pharmacology* 10:968
208. Zheng J, Chen L, Lu T, Zhang Y, Sui X, et al. 2020. MSCs ameliorate hepatocellular apoptosis mediated by PINK1-dependent mitophagy in liver ischemia/reperfusion injury through AMPKα activation. *Cell Death & Disease* 11:256
209. Zhong Z, Liang S, Sanchez-Lopez E, He F, Shalapour S, et al. 2018. New mitochondrial DNA synthesis enables NLRP3 inflammasome activation. *Nature* 560:198-203
210. Zhong Z, Umemura A, Sanchez-Lopez E, Liang S, Shalapour S, et al. 2016. NF-κB Restricts Inflammasome Activation via Elimination of Damaged Mitochondria. *Cell* 164:896-910
211. Zhou H, Zhu P, Wang J, Zhu H, Ren J, Chen Y. 2018. Pathogenesis of cardiac ischemia reperfusion injury is associated with CK2α-disturbed mitochondrial homeostasis via suppression of FUNDC1-related mitophagy. *Cell Death & Differentiation* 25:1080-93
212. Zhou R, Yazdi AS, Menu P, Tschopp J. 2011. A role for mitochondria in NLRP3 inflammasome activation. *Nature* 469:221-5
213. Zhou W, Ma D, Sun AX, Tran H-D, Ma D-L, et al. 2019. PD-linked CHCHD2 mutations impair CHCHD10 and MICOS complex leading to mitochondria dysfunction. *Hum Mol Genet* 28:1100-16
214. Zhu Y, Ji J-J, Yang R, Han X-Q, Sun X-J, et al. 2019. Lactate accelerates calcification in VSMCs through suppression of BNIP3-mediated mitophagy. *Cellular Signalling* 58:53-64